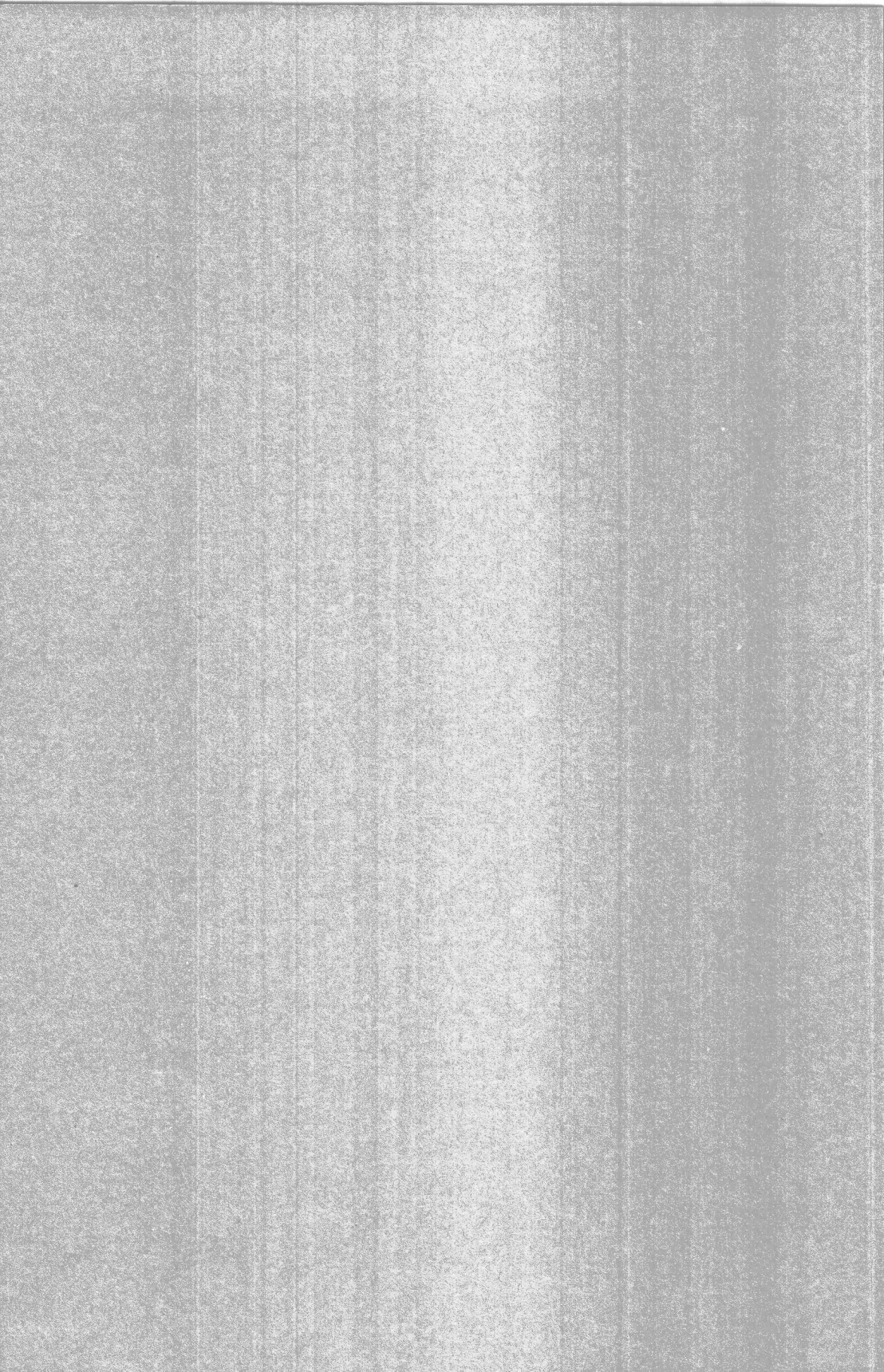


THERMAL HELIUM DESORPTION SPECTROMETRY  
APPLIED TO  
METALLIC IMPLANTS IN TUNGSTEN

2092 5072

G.J. VAN DER KOLK





51943  
C10086



THERMAL HELIUM DESORPTION SPECTROMETRY APPLIED TO METALLIC IMPLANTS IN TUNGSTEN

BIBLIOTHEEK TU Delft  
P 2092 5072



C

865194





# THERMAL HELIUM DESORPTION SPECTROMETRY APPLIED TO METALLIC IMPLANTS IN TUNGSTEN



PROEFSCHRIFT

TER VERKRIJGING VAN DE GRAAD VAN DOCTOR  
IN DE TECHNISCHE WETENSCHAPPEN AAN DE  
TECHNISCHE HOGESCHOOL DELFT, OP GEZAG VAN DE  
RECTOR MAGNIFICUS, PROF. IR. B. P. TH. VELTMAN,  
IN HET OPENBAAR TE VERDEDIGEN TEN OVERSTAAN  
VAN HET COLLEGE VAN DEKANEN OP DONDERDAG  
14 JUNI 1984 TE 14.00 UUR

DOOR

GERRIT JAN VAN DER KOLK

GEBOREN TE EDE  
NATUURKUNDIG INGENIEUR

Dit proefschrift is goedgekeurd door de promotoren:

PROF. DR. IR. H. VAN DAM en

PROF. DR. J.Th.M. DE HOSSON

30

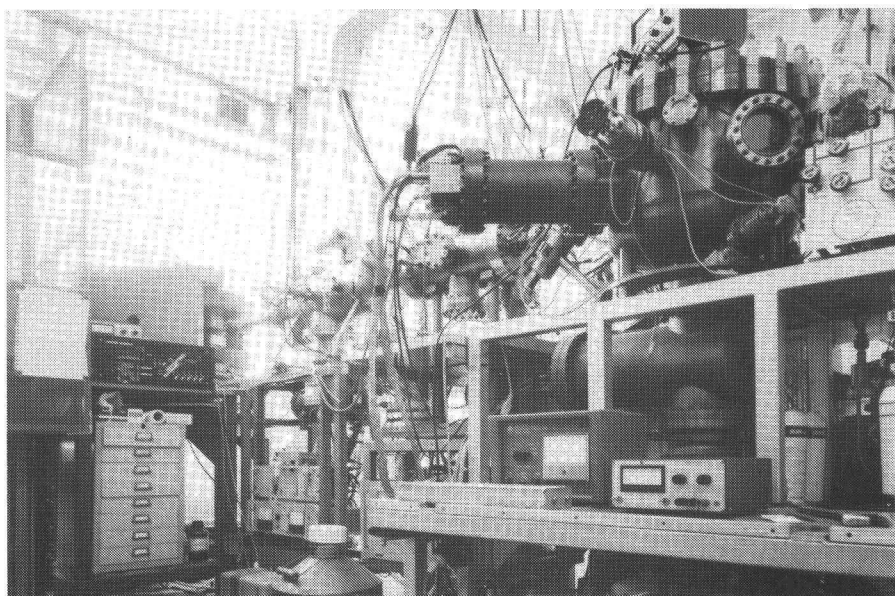
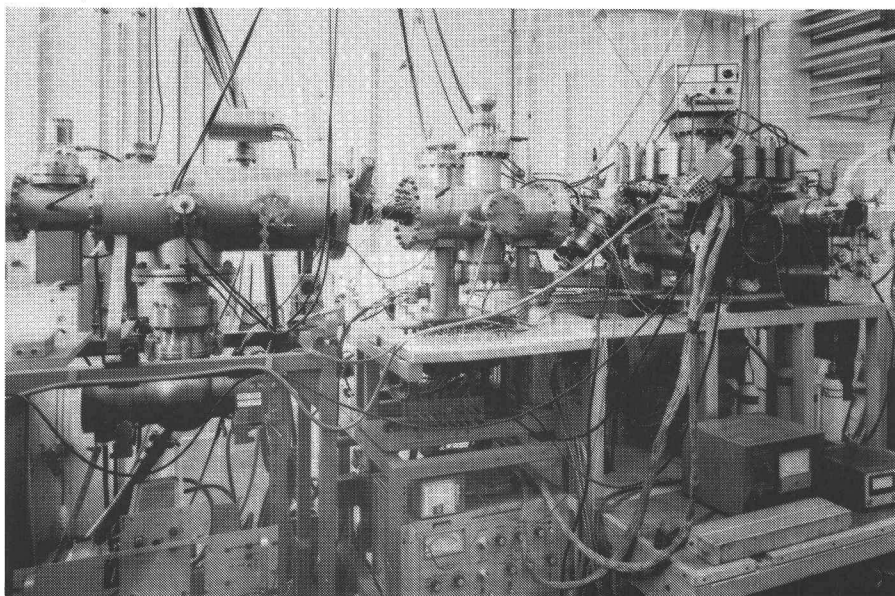
Dr. A. van Veen en Dr. Ir. L.M. Caspers hebben in hoge mate bijgedragen aan de begeleiding bij het tot stand komen van het proefschrift en zijn als zodanig aangewezen door het College van Dekanen.



aan Trees  
aan mijn ouders

The work described in this thesis was part of the research programme of the Stichting voor Fundamenteel Onderzoek der Materie (Foundation for Fundamental Research on Matter) and was supported financially by the Nederlandse Organisatie voor Zuiver Wetenschappelijk Onderzoek (Netherlands Organization for the Advancement of Pure Research). It was carried out in the group Reactorphysics at the Interuniversity Reactor Institute Delft and the Department of Applied Physics of the Delft University of Technology.





The ion accelerator and helium desorption equipment used in this study.

## VOORWOORD

Bij het verschijnen van dit proefschrift wil ik allen danken, die direct of indirect hebben bijgedragen aan het tot stand komen ervan.

Tom van Veen wil ik danken voor de prettige samenwerking en voor de mogelijkheid die hij mij bood om, met grotendeels door hem ontwikkelde apparatuur, moderne experimentele fysica te kunnen bedrijven.

Leo Caspers ben ik erkentelijk voor de introductie die hij mij gaf in de simulaties met behulp van computermodellen, daarnaast herinner ik me met veel plezier de talloze discussies over wetenschappelijke en niet-wetenschappelijke onderwerpen.

Mijn promotoren Jef de Hosson en Hugo van Dam wil ik danken voor de kritiek geleverd op het concept proefschrift.

Mijn collega's binnen de vakgroep Reactorfysica Jan de Roode, Kees Westerduin, Maurits Ypma, Bob Heyenga, Karel Roos, Dik de Haas en voormalig collega Cees Rieff wil ik danken voor hun hulp bij het oplossen van voorkomende problemen.

Met Frits Pleiter en Kees Post uit Groningen heb ik zeer prettige contacten onderhouden.

Met de student André Hydra en de buitenlandse gasten Bent Nielsen, Tim Armstrong en Brian Nielsen heb ik prettig samen kunnen werken.

De medewerkers van de tekenkamer en de instrumentmakerij van de afdeling Technische Natuurkunde hebben in hoge mate bijgedragen aan de vervaardiging van de meetopstelling.

Nita Brands en dhr. A.R. Suiters hebben medegewerkt aan de vormgeving van dit proefschrift.

Tenslotte wil ik jou, Trees, bedanken voor de mogelijkheid die je me bood om me een tijdlang volledig aan het hier beschreven onderzoek te kunnen wijden.

## CONTENTS

<b>VOORWOORD</b>	<b>8</b>
<b>CONTENTS</b>	<b>9</b>
 <b>1. INTRODUCTION.</b>	 <b>13</b>
 <b>2. PERFORMANCE OF THE EXPERIMENTAL APPARATUS FOR HELIUM DESORPTION STUDIES.</b>	 <b>17</b>
2.1. GENERALLY.	17
2.2. DANFYSIK ION SOURCE AND BEAM LINE.	20
2.3. GAS ION SOURCE.	22
2.4. DESORPTION AND DATA HANDLING.	24
2.5. TARGET PREPARATION.	27
2.6. CONCLUSIONS AND FINAL REMARKS.	29
 <b>3. INTERACTION OF VACANCIES WITH IMPLANTED IMPURITIES.</b>	 <b>31</b>
3.1. CASCADE ANNEALING OF TUNGSTEN IMPLANTED WITH 5 keV NOBLE GAS ATOMS; A COMPUTER SIMULATION.	33
3.1.1. Introduction.	33
3.1.2. Static lattice calculations.	34
3.1.3. Monte Carlo calculations.	36
3.1.4. Marlowe calculations.	38
3.1.5. Discussion.	39
3.2. EFFECTS OF VACANCIES NEAR SUBSTITUTIONAL IMPLANTS ON TRAPPING AND DESORPTION OF HELIUM; A SIMULATION.	43
3.2.1. Introduction.	43
3.2.2. He drainage from implants to nearby V.	44
3.2.2.1. Static lattice calculations.	44
3.2.2.2. Trapping of He at V and KrV/AgV.	45
3.2.2.3. Drainage of He from KrV/AgV to and retrapping in nearby V/HeV.	48
3.2.3. Random walk simulations.	50
3.2.3.1. Periodically arranged traps.	50
3.2.3.2. Shielding at infinitely low defect concentration.	54
3.2.3.3. Shielding of defects by more than one V.	57
3.2.4. Discussion.	57

<b>3.3. INTERACTION OF VACANCIES WITH IMPLANTED METAL ATOMS IN TUNGSTEN OBSERVED BY MEANS OF THERMAL HELIUM DESORPTION SPECTROMETRY AND THE PERTURBED ANGULAR CORRELATION TECHNIQUE.</b>	<b>61</b>
3.3.1. Introduction	61
3.3.2. THDS experiments.	62
3.3.2.1. Method.	62
3.3.2.2. Experimental results.	64
3.3.2.3. Defect characterization.	67
3.3.3. PAC experiments.	71
3.3.3.1. Method.	71
3.3.3.2. Experimental results.	73
3.3.3.3. Defect characterization.	79
3.3.4. Model calculations.	82
3.3.4.1. Implantation simulations with Marlowe.	82
3.3.4.2. Annealing results.	83
3.3.5. Interpretation of the results.	86
3.3.5.1. Discrepancy between THDS and PAC results from as-implanted samples.	86
3.3.5.2. Vacancy migration energy.	86
3.3.5.3. Vacancy binding energies.	87
3.3.5.4. Larger defect clusters.	89
3.3.6. Conclusions.	89
 <b>4. INTERACTION OF INTERSTITIALS WITH SUBSTITUTIONAL IMPURITIES.</b>	 <b>93</b>
 4.1. BINDING OF HELIUM TO METALLIC IMPURITIES IN TUNGSTEN; EXPERIMENTS AND COMPUTER SIMULATIONS.	 95
4.1.1. Introduction.	95
4.1.2. Experimentally.	96
4.1.3. Experimental results.	97
4.1.3.1. Annealing temperature variation after metal implantation.	97
4.1.3.2. Peak assignment.	98
4.1.3.3. Peak fitting.	103
4.1.3.4. He precipitation at high dose He injection.	106
4.1.4. Static lattice calculations.	107
4.1.4.1. Pair potentials.	107
4.1.4.2. Calculated results.	110



	11
4.1.5. Discussion.	112
4.1.6. Application.	113
4.2. INTERACTION OF SELF INTERSTITIALS WITH METALLIC IMPURITIES IN TUNGSTEN OBSERVED WITH THDS.	117
4.2.1. Introduction.	117
4.2.2. Experimental results.	118
4.2.3. Discussion.	121
5. INTERACTION BETWEEN IMPLANTED IMPURITIES.	125
CLUSTERING PHENOMENA OF IMPLANTS IN TUNGSTEN OBSERVED WITH THDS.	127
5.1. Introduction.	127
5.2. Experimental results.	129
5.2.1. Experimentally.	129
5.2.2. Results.	129
5.3. Static lattice calculations.	136
5.4. Discussion.	138
5.4.1. Ag results.	138
5.4.2. Other metallic implants.	140
5.4.3. Mobility and clustering mechanism.	140
5.5. Conclusion.	142
SUMMARY	145
SAMENVATTING	146
CURRICULUM VITAE	147

Section 3.1. Accepted by Nuclear Instruments and Methods  
in slightly different form.

Section 3.2. To be published in Nuclear Instruments and Methods.

Section 3.3. To be published in Radiation Effects.

Section 4.1. To be published in Journal of Nuclear Materials.

Section 4.2. To be published in Radiation Effect Letters.

Section 5. To be published in Nuclear Instruments and Methods.



## 1. INTRODUCTION.

Since the start in the fifties the implantation of metals with ions has continuously gained interest. Originally all the research effort was devoted to the processes occurring in construction materials for fission reactors during implantation in an attempt to simulate neutron irradiation and the formation of transmutation products in the materials. Nowadays the interest is fed by the prospect that the first wall and other construction parts of the future fusion reactor will be subjected to a stream of particles, which results in a number of displacements per atom that will be a manifold of that in a "classic" fission reactor [1]. Furthermore a recent development is to use ion implantation as a means for advanced "metal tailoring" [2]. The work described in this study reflects this double interest. A central role is thereby allotted to helium. Originally interest in He aroused when it was realized that He produced by  $(n,\alpha)$  reactions stabilized the voids appearing in neutron irradiated metals [3]. Later E.V. Kornelsen [4] showed that the high mobility in combination with the insolubility of He in refractory metals provided a unique possibility to detect point defects at very low concentrations.

Thermal Helium Desorption Spectrometry (THDS) is applied in this study to observe different defect reactions in tungsten of the metallic impurities Ag, Cu, Mn, Al, Cr and In. W was chosen for a variety of reasons. Firstly W is thoroughly studied with THDS [5,6], so the novel data presented here of metallic implants can be compared with those already known for noble gases in W. Secondly W and its companion Mo, although no short term candidates for the first wall of the fusion reactor [7], seem to be candidate materials for the limiter, which

protects the first wall against heating by plasma disruptions and neutral beams [8,9]. Thirdly the high melting point of W results in a "stretched temperature scale" for the different migration and dissociation processes taking place with the point defects. The results presented in chapter 4 justify this choice; in any other metal the sample would have to be cooled below room temperature in order to use THDS successfully on metallic impurities.

The interest in metallic impurities is twofold. Firstly in irradiated materials transmutation products may play an important role as nucleation centra for clustering of He, vacancies and/or self-interstitials. Binding of vacancies or interstitials to the impurities will reduce the void growth rate [10]. Binding of He to the impurities will lead to heterogeneous nucleation of He bubbles which has shown to increase the bubble density [11]. Secondly insight into the behaviour of the metallic impurities in the implantation produced "dilute alloy" may facilitate an understanding of the fundamental processes occurring in irradiated alloys or metals containing precipitates.

To interpret the data obtained with THDS static lattice calculations and random walk calculations are performed. The static lattice calculations are based on a description of a metal lattice in terms of central two-body potentials, see also ref. [12], and facilitate a correct assignment of the peaks visible in the desorption spectra. Random walk simulations, see also ref. [13], are applied to investigate the effect of near vacancies.

In chapter 2 a concise description is given of the experimental set-up. The performance of the equipment with respect to the THDS technique is discussed briefly.

In chapter 3 the interaction of vacancies with implanted impurities is described. The first two sections are dedicated to computer simulations which support a correct interpretation of the THDS data. It is demonstrated that after 5 keV heavy noble gas implantation one or more vacancies are present in the vicinity of the implant. Shielding effects of the vacancies on the probability of He-trapping by the implant as well as retrapping in near vacancies of He dissociating from implants are calculated. In section 3.3 experimental results are presented obtained with THDS and PAC\* (Perturbed Angular Correlation). Vacancy binding to the substitutional implants and vacancy clustering

are observed. The stabilising role of He in a small vacancy cluster ( $V_3$ - $V_4$ ) is clearly demonstrated.

In chapter 4 the interaction of interstitials with substitutional impurities is described. Section 4.1 deals with binding of He-interstitials to substitutional impurities. Besides the experimental data the results of static lattice calculations are presented. The agreement between observed and computed binding energies is reasonable. Section 4.2 is devoted to the interaction of self-interstitials with substitutional impurities. Self interstitial atoms push impurity atoms out of their substitutional position. This mechanism may be the explanation for the often observed "radiation enhanced diffusion" of impurities [14].

In chapter 5 finally the interactions between the impurity atoms are observed. To this purpose the doses of the implanted impurities are somewhat higher than for the experiments described in chapters 3 and 4. Surprisingly it is observed that only in the case of Ag-implantation extra peaks, indicating clustering, can be grown. Calculations are presented which indicate that clustering of the other implants certainly should appear in the THDS spectra. The results are of importance for "radiation induced segregation", see ref. [15].

\*The PAC experiments described in this thesis appear by courtesy of Dr. F. Pleiter and Dr. K. Post of the University of Groningen.

#### REFERENCES.

- [1] L.R. Greenwood, J. of Nucl. Mat. 103/104,1433(1981).
- [2] G. Dearnaley and P.D. Goode, Nucl. Instr. and Meth. 189, 117(1981).
- [3] H. Wiedersich and J. Katz in: Defects and Defect Clusters in BCC Metals and Their Alloys, ed. J.R. Arsenault, Maryland 1973, pp.530-544.
- [4] E.V. Kornelsen, Rad. Eff. 13,227(1972).
- [5] A. van Veen, A. Warnaar and L.M. Caspers, Vacuum 30,109(1980).
- [6] A.A. van Gorkum, Dr. Thesis, Delft 1981,  
E.V. Kornelsen, A.A. van Gorkum, Rad. Eff. 42,113(1979).
- [7] R.W. Conn, J. of Nucl. Mat. 85/86,9(1979).
- [8] A. Tobin, J. of Nucl. Mat. 85/86,197(1979).
- [9] K. Furuya, N. Nagata, R. Watanabe and H. Yoshida, J. of Nucl.

Mat. 103/104,937(1981).

- [10] A.E. Little, AERE Report R-9427, Harwell 1979.
- [11] R. Bullough, M.R. Hayns, M.H. Wood, J. of Nucl. Mat. 85/86,559(1979).
- [12] W.F.W.M. van Heugten, Dr. Thesis, Groningen 1979,  
W.F.W.M. van Heugten, F. van de Berg, L.M. Caspers and  
A. van Veen, Delft Progr. Rep. 3,97(1978).
- [13] R.H.J. Fastenau, Dr. Thesis, Delft 1982,  
R.H.J. Fastenau, A. van Veen, P. Penning, L.M. Caspers,  
Phys. Stat. Sol. (a) 47,577(1978).
- [14] Z.L. Wang, J.F.M. Westendorp and F.W. Saris, Nucl. Instr. and  
Meth. 209/210,115(1983).
- [15] A.D. Marwick, R.C. Piller, P.M. Sivell, J. of Nucl. Mat. 83,35(1979).

## 2. PERFORMANCE OF THE EXPERIMENTAL APPARATUS FOR HELIUM DESORPTION STUDIES.

### 2.1. GENERALLY.

Thermal Helium Desorption Spectrometry (THDS) encompasses the decoration of defects with low energy He and the subsequent desorption of He by heating. The He ion energy is chosen such that no new lattice damage is introduced. Since He is interstitially mobile in most metals at room temperature (RT) and is trapped at positions with a lower electron density than the surrounding lattice, e.g. vacancies, vacancy clusters and dislocations, this provides a method to detect defects in near surface layers. The He release rate is monitored during linear heating with time. From the different desorption peaks information on the defects present is obtained. The defects may be introduced by implantation, deformation etc. In this study defects were introduced by implantation. A typical THDS experiment is schematically shown in fig. 1: after the partial annealing step low energy He is injected. Subsequently the crystal is heated to desorb He and finally the He detector is calibrated.

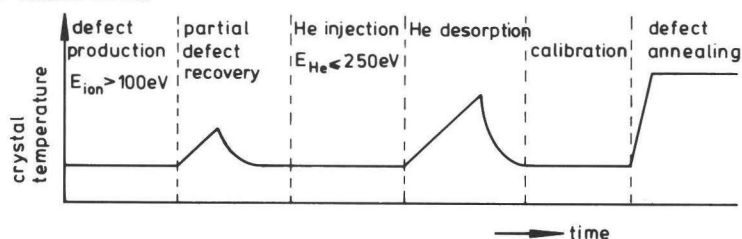


fig. 1: Scheme of a THDS experiment.

Requirements for THDS equipment are described by Caspers and van Veen [1] and Kornelsen and van Gorkum [2,3]. The most important requirements are: i) a low total pressure ( $<3 \times 10^{-8}$  Pa); ii) a low partial He-pressure to have a low He-background during desorption; iii) purity of the He-beam and, if defects are introduced by implantation, also purity of the damaging-beam; iv) homogeneous distribution of the ions over the target surface; v) adequate sensitivity for He during desorption (detection limit better than  $10^8$  He atoms); and vi) high purity of the sample. Within these limitations several design options are possible as dynamic or static desorption, i.e. a high or low He pumping speed during desorption, temperature measurement by thermocouple or pyrometer etc.

The experimental set-up used in this study, further called HDS3, was developed to combine THDS with other ion beam analysis techniques in a large vacuum chamber [4]. To obtain a high He sensitivity a small desorption volume can be created during desorption in the large multi-purpose vacuum chamber. A scheme is shown in fig. 2.

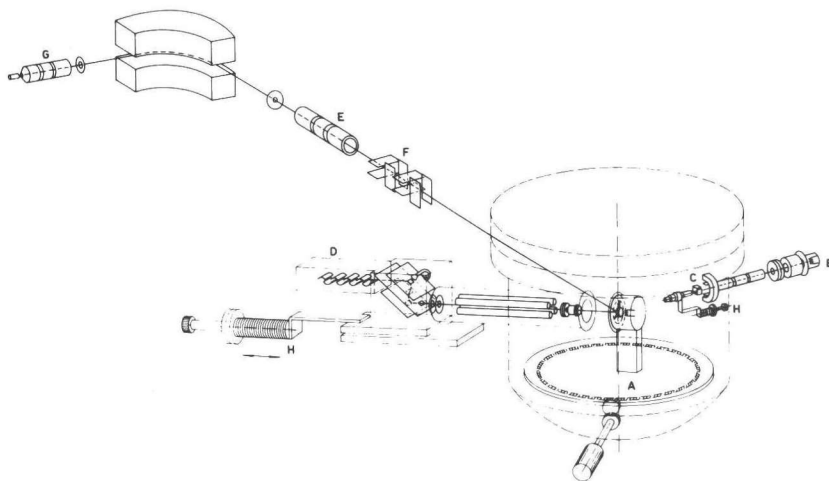


fig. 2: Scheme of the equipment with: the target housing A, the gas ion source B with Wien filter C, the quadrupole mass analyzer with channeltron and dynode multiplier D, the beam transport line with deflection plates F and Einzel lens E of the Danfysik ion source G. Both beam transport system of the gas ion source and quadrupole mass analyzer can be driven towards the crystal by linear motion drives H.



The target, in this study a W(100) single crystal, is mounted in a half open cylinder A in the centre of a large UHV chamber. The cylinder can rotate around the centre of the UHV chamber with the aid of a ring shown in fig. 2 such that the target can be made to face the mass spectrometer D. The latter can be rolled forward so that mass spectrometer and target housing together form a reduced volume of 1.4 dm<sup>3</sup>. Other auxiliary devices the target can face are: the gas ion source B and the beam transport line E-F of a Danfysik ion source G. The Danfysik ion source, linked to a magnetic mass selector, allows the controlled introduction of ions of virtually all elements. Extra options not used in this study include a lithium ion gun and an energy selector meant for measuring the kinetic energy of desorbed He.

To match the different criteria concerning partial and total pressure HDS3 was supplied with an elaborate pumping system, see fig. 3.

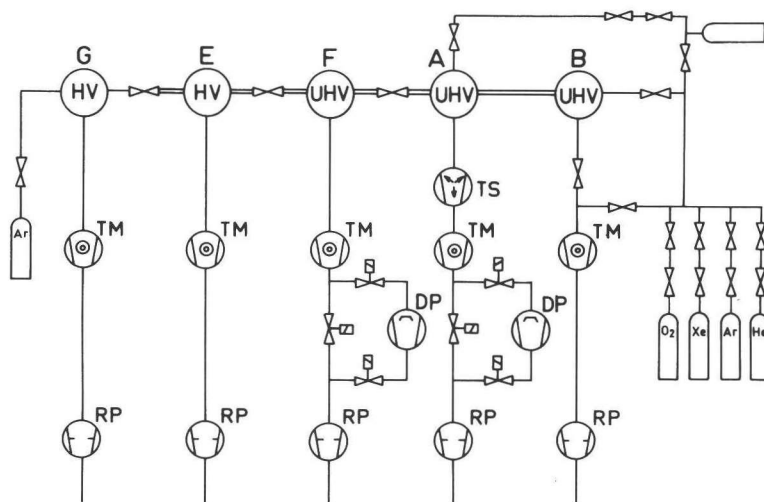


fig. 3: Scheme of the differential pumping stations with titanium sublimator TS, turbomolecular pumps TM, diffusion pumps DP and roughing pumps RP. Indicated are the vacuum chambers of: G) Danfysik ion source, E) intermediate chamber with Einzel lens, F) intermediate chamber with sweeping plates, A) target chamber and B) gas ion source.

All sections have their own pumping system and are separated by small apertures. This facilitates variousial pumping in the different sections so that the pressure in the target chamber normally is at  $2 \times 10^{-8}$  Pa and during impurity ion implantation at  $5 \times 10^{-7}$  Pa. The pressure in the intermediate chambers E and F and the Danfysik source G are  $3 \times 10^{-6}$  Pa,  $5 \times 10^{-7}$  Pa and  $10^{-5}$  Pa respectively. During impurity ion implantation the working-pressure in the source G is  $7 \times 10^{-3}$  Pa and in the chambers E and F  $1 \times 10^{-5}$  and  $2 \times 10^{-6}$  Pa respectively. During noble gas ion implantation the pressure in the target chamber may rise to  $2 \times 10^{-5}$  Pa. The performance of HDS3 with respect to the THDS requirements will be discussed in the next sections.

## 2.2. DANFYSIK ION SOURCE AND BEAM LINE.

The Danfysik ion source, type 911A, originally designed by Sidenius [5] is capable of ionizing virtually all elements. In fig. 4 a cross section of the source is shown. Vapour is produced by heating of the implant material in a small oven O which heats up to a temperature of 1900 K. Through a small hole in the back of the oven a noble gas flow is maintained to facilitate easy start up and operation of the source. A fraction of the mixture of vapour and gas is ionized in the hollow cathode C and extracted from the source by a potential difference variable up to 30 keV.

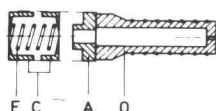


fig. 4: The Danfysik ion source with:  
O) oven, A) anode, F) filament  
and C) cathode.

Mass selection is provided by magnetic deviation over 90 degrees. The mass resolution  $M/\delta M$  is better than 200 which is adequate for our experiments. The magnet is double focussing, i.e. point to point focussing. An ion-optical scheme is shown in fig. 5.

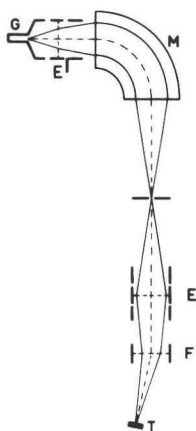
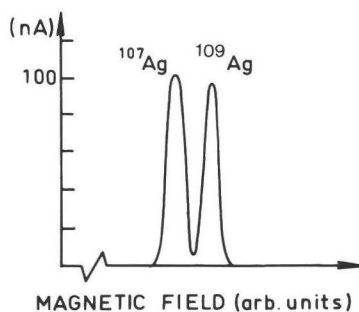


fig. 5: Ion optical scheme of HDS3.  
G) Danfysik ion source,  
E, E<sup>1</sup>) Einzel lens, F) sweeping  
plates, M) magnet, T) target.

The Einzel lens E<sup>1</sup> next to the ion source is meant to focus the magnet on the extraction conus. In E the ion beam is focussed again. The current of 5 keV Ag measured on a Faraday cup positioned at F as a function of the magnetic field is shown in fig. 6.

fig. 6: Current of 5 keV Ag measured with a  
Faraday cup in the intermediate chamber  
F as a function of the magnetic field.



In some cases a practical limit to the mass resolution is set by fluctuations of the cathode voltage; melting of the material in the oven sometimes causes temporarily blocking of the gas flow through the oven, leading to fluctuations in the source pressure, cathode current and thus cathode voltage. Close to the lens at E a beam profile monitor is mounted. Beams with energies above 15 keV can be monitored. At F four pairs of deflection plates are mounted, two for vertical, and two for horizontal deviation. One pair of the deflection plates is used to give the beam a deviation of 5 degrees, sufficient to separate the ions from the neutrals in the beam.

Furthermore two pairs of deflection plates are used to sweep the beam with frequencies of 2500 Hz in horizontal and 700 Hz in vertical direction respectively, to obtain a uniform distribution on the target T [6]. Since the sweeping voltages are sinusoidal, uniformity is only guaranteed if the sweeping amplitude is such that an area with several times the target diameter is swept. In practice both voltages were adjusted so that any of them with the other set zero gave a current reduction of a factor two. Moreover the beam was defocussed as well. In table 1 typical target currents are shown.

table 1: Current  $I_t$  for different ions with energies of 10 keV and 25 keV on the target (surface  $0.38 \text{ cm}^2$ ).

Mass	Ion	$I_t$ (10 keV)	$I_t$ (25 keV)
40	Ar	100 (nA)	2000 (nA)
55	Mn	25	50
63	Cu	25	50
65	Cu	12	26
107	Ag	30	55
109	Ag	28	50
180			
186	W	5	7

The dose on the target is determined by integration of the current and correction for the secondary electron emission yield using data known from literature [7]. The systematic error in the obtained doses may be ~20%.

### 2.3. GAS ION SOURCE.

Noble gas ions are produced in an electron impact source designed and constructed in Delft [8]. The energy range is between 50 eV and 6 keV (see also ref. [4]). All construction parts are shielded by a series of tubes which for low ion energies are set on a negative potential in order to transport the beam at a higher energy. All lens voltages are superposed on this transport potential, see fig. 7. The beam is mass analysed by an electromagnetic Wien-filter positioned in the middle of the beam transport line. The mass resolution  $M/\delta M$  with a magnetic field of 0.1 T for a He beam with energy below 750 eV is ~3.

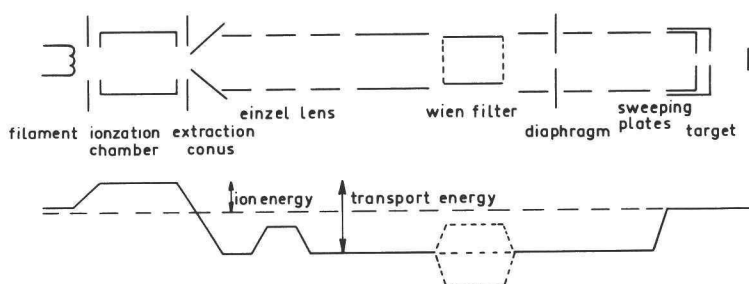


fig. 7: Scheme of the potentials in the beam transport line of the gas ion source operated at low ion energy.

In view of the purity of the used helium gas (better than 99.9 %), this is adequate to reduce the normal UHV residual ions in the He beam to fractions less than  $10^{-4}$ . The magnetic field can be increased to 0.3 T, giving a mass resolution  $M/\delta M$  of 10 for the case mentioned above. The whole beam transport system can be moved forwards towards the crystal by a drive mechanism, so that the last diaphragm of the beam transport is about 15 mm removed from the target surface. The diaphragm diameter (3.5 mm) is chosen so that one third of the target surface was injected with gas ions whereas with the impurity beam the whole target was bombarded. Proper overlap of the bombarded area's is thus ensured. The gas ion beam is also swept in two directions with similar frequencies as mentioned in 2.2. The same criterion was applied to adjust sweeping amplitudes. Typical target currents of He with Wien filter and sweeping plates in operation are shown in fig. 8 as a function of energy. Correction for secondary electrons is again taken from literature [7].

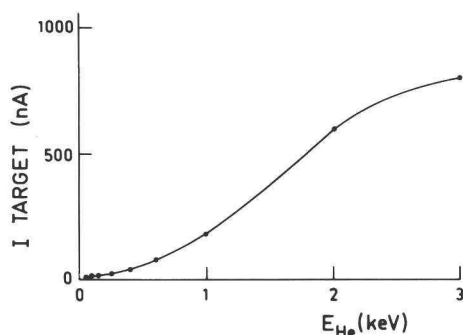


fig. 8: Current of He as a function of energy on the target (bombarded area 0.1 cm<sup>2</sup>).

The gas ion source is pumped by a separate turbomolecular pump in order to keep the partial He pressure below  $3 \times 10^{-5}$  Pa during He injection. To keep the partial He pressure low during desorption also a slit is mounted in the beam line which can be closed. Due to the low conductance the partial He pressure is below  $10^{-11}$  Pa even with opened slit.

#### 2.4. DESORPTION AND DATA HANDLING.

The crystal is heated by 1.5 keV electron bombardment on the rear of the sample. The temperature is measured using a WRe3%-WRe25% thermocouple which is mounted in a small hole in the target. During heating the crystal is set on +1.5 keV, thus making it necessary to use an insulation amplifier for the thermocouple signal. The advantage of this system over the alternative, i.e. an electron emitting filament on -1.5 keV, is that all electrons are attracted by the crystal, thus avoiding excessive heating of the crystal surroundings. During desorption the temperature is controlled linearly with time with the aid of a differential amplifier, which compares the real thermocouple signal with a computer generated signal. A scheme is given in fig. 9.

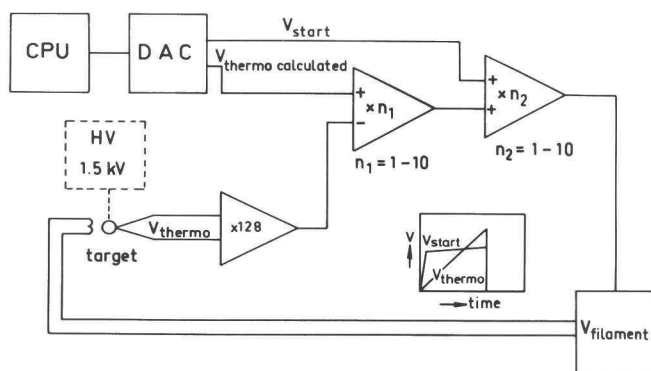


fig. 9: Scheme of the sample heating with central processing unit (CPU) and digital to analogue converter (DAC), the inset shows the two computer generated signals.

Since the filament starts with electron emission only if it is at a certain rather high temperature, the control-signal, obtained from the feed back loop, is superposed on a steering signal chosen so that the filament is immediately heated to that temperature once the desorption step starts. The two computer generated signals are shown in the inset of fig. 9. The heating rate normally used is  $\sim 40$  K/s, see also fig. 10.

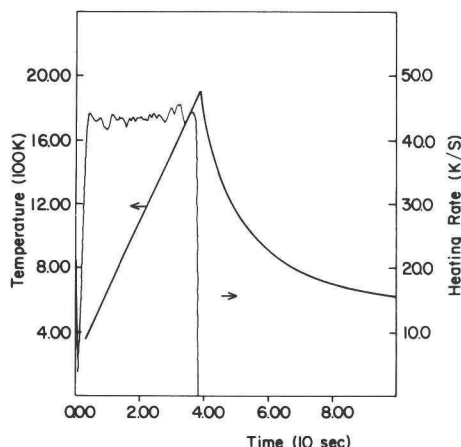


fig. 10: Temperature profile and heating rate of the sample during a desorption step.

The He atoms released during the crystal heating are detected by a quadrupole mass analyser (Balzers QMG 311) in combination with a dynode multiplier. Before desorption the mass spectrometer is moved towards the target housing (the half open cylinder A mentioned in section 2.1) to create a small desorption volume of  $1.4 \text{ dm}^3$ , see also ref. [4]. During desorption the thermocouple signal and mass spectrometer signal are sampled with a standard frequency of 10 Hz. This is sufficient to match the criterion derived in [2], that the sampling density should be such that at least 10 points are sampled over a width of  $0.15 T_m$  for a peak with temperature  $T_m$  at the peak maximum.

The accuracy of the calculated temperature is determined by: i) the uncertainty in the temperature of the cold joint of the thermocouple; ii) the accuracy of the thermocouple; and iii) the accuracy of the data collection system including amplifiers, voltage to frequency converters and timers. Ad i), the cold joint is mounted on the back of the half open cylinder A. Heating of the sample leads to an aftereffect in the form of a slightly increased temperature of the cup A. By monitoring peak shifts after various crystal heating treatments the

magnitude of this effect was determined as well as the required cooling time of the equipment. In this way the uncertainty is kept below 6 K. Ad ii), The accuracy of the thermocouple is according to the manufacturers better than 1%. Ad iii), The accuracy of the whole data acquisition system is kept better than 1% by regular calibration.

The accuracy of the obtained temperatures ranges from 3% to 2.5% for low (400 K) respectively high temperatures (1500 K). Pyrometric temperature determination of the sample under most favourable conditions would have given an uncertainty of the same magnitude in the region above 900 K. Below this temperature extrapolations based on crystal thermal capacity, radiation loss, supplied power and conduction loss can be used to deduce the temperature profile as a function of time. Since the conduction loss, which is the most important at low temperature, will depend on the temperature of the local surroundings, this will introduce a fairly large uncertainty at low temperatures. In this study desorption peaks at rather low temperatures are observed, so a thermocouple is a necessary expedient.

The mass spectrometer is calibrated by injection of a known amount of He in the target housing A through a small pipe in the back of the housing. The He shot normally contains  $\sim 10^{12}$  He atoms. This number is deduced by measuring the He pressure in a 25 cc vessel with an absolute membrane manometer prior to expansion in a 1000 cc vessel. For each shot a 1cc volume is filled with He from the 1000 cc vessel. In practice it is seen that the sensitivity for He desorbing from a W(100) target is much better than calculated from the calibration pulse. We assume that this is caused by preferential desorption in forward direction from the target, an effect that was predicted by van Veen et al. [9]. The ratio between real and calculated sensitivity for the target used was obtained by determining trapped fractions of 4 keV He implanted  $\sim 20$  degrees of the  $\langle 100 \rangle$  channel. From literature [10] it is known that 10% of the He atoms injected into a W(100) crystal with an energy of 4 keV, with an implantation angle of  $\sim 20$  degrees off the  $\langle 100 \rangle$  channel and with a dose of  $3 \times 10^{12}$  He<sup>+</sup>/cm<sup>2</sup>, is trapped. The sensitivity of the mass spectrometer was found to vary critically with total pressure and surface coverage of the secondary electron multiplier. In the case of low temperature He desorption peaks ( $\sim 400$  K) pressure variation cannot be avoided by heating of the target surroundings since the crystal temperature will rise than as well, leading to premature He desorption. Therefore in that case various cali-



bration shots were performed prior to and after desorption. Only those spectra with a sensitivity variation less than 10% are used in this study. Sensitivities obtained in this set-up are  $8 \times 10^{-7}$  A/Pa or  $8 \times 10^5$  He atoms per measured pulse at the exit side of the multiplier.

Since desorption is performed in the dynamic mode; i.e. He is deliberately pumped, a correction for the average residence time or vacuum time constant  $\tau$  should be made. The relation between He desorption rate  $L(t)$  and the measured partial He pressure  $P(t)$  during heating of the target is given by:

$$L(t) = V \left( \frac{dP(t)}{dt} + \frac{P(t)}{\tau} \right) \quad (1)$$

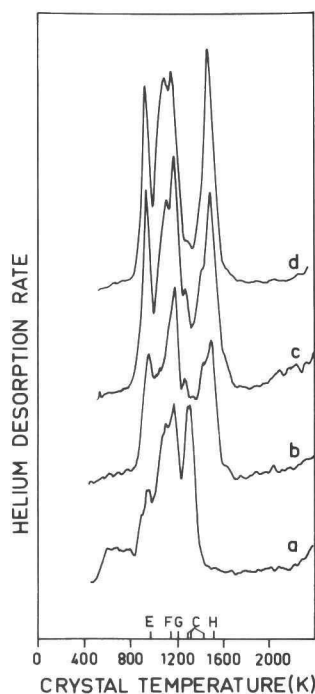
$\tau$  is the vacuum time constant  $V/S$ , with  $V$  the desorption volume and  $S$  the He pumping speed, see [4]. Normally  $\tau$  is determined by measuring the exponential decrease of a He pulse. In our case the only He inlet in the desorption volume is the inlet for the calibration pulse, the conductance of this pipe is rather low. Therefore the value of  $\tau$  was derived from the exponential decrease of  $P$  after the He release of the crystal was stopped abruptly by stopping the electron bombardment. The value thus found is 0.1 s for properly connected target housing and mass spectrometer. Peaks were numerically corrected for this  $\tau$ . It should be noted that the choice of the sampling rate of 10 Hz together with  $\tau=0.1$  s is the optimum one for minimizing the noise in the He release rate [2].

## 2.5. TARGET PREPARATION.

The target used in this study was a W(100) single crystal made from a rod delivered by the Materials Research Corporation. According to the manufacturer the purity is better than 99.999%. A disk of diameter 0.7 and thickness 0.3 cm was spark eroded from the rod. Subsequently the crystal was mechanically polished with diamond powder with grain size of 0.25  $\mu\text{m}$ . When the surface could not be improved any more with this treatment electrolytical polishing was applied. A 2% NaOH solution in combination with proper voltage and solution flow settings gave good results. Micrographs taken with the scanning electron microscope showed a smooth surface. After mounting of the freshly prepared crystal the desorption spectra indicated the presence of an impurity. Heating under a hydrogen atmosphere of  $10^{-4}$  Pa showed no improvement.

Heating at 2350 K during 48 hours under an oxygen atmosphere of  $2 \times 10^{-4}$  Pa showed a drastic reduction of the impurity effect. Therefore we assume that C was involved.

fig. 11: He desorption spectra for W(100) implanted with  $1.2 \times 10^{13}$   $1.5 \text{ keV He}^+ \text{ cm}^{-2}$ , after: a) one; b) two; c) three; and d) five standard oxygen treatments, see text.



In fig. 11 spectra are shown of the crystal implanted with  $1.2 \times 10^{13}$   $1.5 \text{ keV He}^+ \text{ cm}^{-2}$  after successive oxygen treatments. The well known E, F, G and H peaks, indicating He binding to monovacancies, become visible [11], whereas the extra peaks labelled C shrink after the various oxygen treatments. The oxygen treatment was repeated  $\sim 7$  times, followed by flashing to 2500 K several times at  $2 \times 10^{-8}$  Pa. The cleaning treatment is described in ref. [12]. A few tens of surface layers were sputtered with Ar, again followed by several flashes to 2500 K to remove possible subsurface Ar-clusters. The fraction of low energy implanted He trapped in the crystal after these treatments was less than 0.01%, the peaks representing He binding to vacancies showed no extra binding states, so it was concluded that virtually no traps were present.

## 2.6. CONCLUSIONS AND FINAL REMARKS.

Versatility is one of the most characteristic features of HDS3. Its low pressure, low He-background and connection to the Danfysik ion source make it suitable for THDS experiments on metallic implants. The desorption method, linear heating and simultaneous He pumping, offers the opportunity to follow He filling behaviour up to very high He doses. A lower limit of the number of defects detectable with this equipment is  $\sim 10^{10} \text{ cm}^{-2}$ . The position of the target, at the crossing of the two beams and the axis of the mass spectrometer, allows other research topics as dual beam damage production, secondary ion mass spectrometry and low energy ion scattering. Not yet available for this study, but now nearing completion, is a target manipulator. With this tool equipped, HDS3 will be able to exploit THDS to its full potential, including the measurement of depth profiles, trapping radii for He etc.

## REFERENCES.

- [1] L.M. Caspers and A. van Veen, Phys. Stat. Sol. (a)68,339(1981).
- [2] A.A. van Gorkum and E.V. Kornelsen, Vacuum 31,89(1981).
- [3] E.V. Kornelsen and A.A. van Gorkum, Vacuum 31,99(1981).
- [4] A. van Veen, A. Waraer and L.M. Caspers, Vacuum 30,109(1980).
- [5] G. Sidenius, Proc. Int. Conf. on Electromagnetic Isotope Separators, Marburg, Germany 1970, p.423.
- [6] E.J. Rogers, Nucl. Instr. and Meth. 189,305(1981).
- [7] G. Carter and J.S. Colligon, Ion Bombardment of Solids, Heinemann, London 1968.
- [8] Design by A. van Veen.
- [9] A. van Veen and L.M. Caspers, Delft Progr. Rep. A1,160(1976).
- [10] E.V. Kornelsen and A.A. van Gorkum, Nucl. Instr. and Meth. 170,161(1980).
- [11] E.V. Kornelsen, Rad. Eff. 13,227(1972).
- [12] K. Besocke and S. Berger, Proc. 7<sup>th</sup> Int. Vacuum Congr, Vienna 1977, Vol.2, pp.893-896.



### 3. INTERACTION OF VACANCIES WITH IMPLANTED IMPURITIES.

#### INTRODUCTORY REMARKS.

In this chapter three sections are presented. In the first section it is concluded from computer calculations that after bombardment of tungsten with 5 keV heavy noble gases implantation produced vacancies are located near the implanted atoms. In the second section the interaction of helium with these nearby vacancies during low energy injection or during desorption is simulated. It follows that these nearby vacancies hinder detection of substitutional implants with THDS. In the third section results obtained from THDS and Perturbed Angular Correlation measurements (PAC) are compared with each other and with the calculated results.



### 3.1. CASCADE ANNEALING OF TUNGSTEN IMPLANTED WITH 5 KEV NOBLE GAS ATOMS; A COMPUTER SIMULATION.

G.J. van der Kolk<sup>1</sup>, A. van Veen<sup>1</sup>, L.M. Caspers<sup>1</sup> and J.Th.M. de Hosson<sup>2</sup>.

<sup>1</sup> Delft University of Technology/Interuniversity Reactor Institute, Mekelweg 15, 2629 JB Delft, the Netherlands.

<sup>2</sup> University of Groningen, Materials Science Centre, Nijenborgh 18, 9747 AG Groningen, the Netherlands.

#### ABSTRACT

The trapping of vacancies by implanted atoms is calculated. After low energy implantation (5 keV) of tungsten with heavy noble gas atoms most of the implanted atoms are in a substitutional position with one or two vacancies within two lattice units. Under the influence of the lattice distortion around the implanted atoms the vacancies follow a preferential migration path towards the implant during annealing. With lattice relaxation simulations migration energies close to the implanted atoms are calculated. Monte Carlo theory is applied to obtain trapping probabilities as a function of implant-vacancy separation and temperature. An estimate of the initial implant-vacancy separation follows from collision cascade calculations. The results show that nearby vacancies are trapped by the implanted atoms.

#### 3.1.1. INTRODUCTION.

After implantation of tungsten with heavy noble gas atoms it is found that there is a recovery step, which can be attributed to vacancy mobility and subsequent recovery at the surface (stage III). With thermal helium desorption spectrometry (THDS) it is also seen that in stage III a defect-complex is formed, probably consisting of a substitutional noble gas atom and one or more extra vacancies. Upon further annealing these defect complexes dissociate. For some implants it was shown that the defects formed then are substitutional noble gas atoms [1].

Recently performed perturbed angular correlation experiments (PAC) on tungsten implanted with 25 keV Ag and In, revealed a near

substitutionality of the implant immediately after implantation, whereas with THDS substitutionality of the implant was seen only after annealing to a temperature above stage III [2].

The aim of this study is to show the presence of near-vacancies at the implant after implantation. Those near vacancies will make it impossible for THDS to detect the implanted atoms. Furthermore it will be shown that during annealing a large fraction of these near-vacancies will migrate to the implant. Energies required for vacancy jumping to various positions near the implanted atoms are estimated using the short-range pair-potential calculations. The thus obtained migration energies are used in a Monte Carlo program to calculate the vacancy capture radius for a uniform vacancy distribution and to calculate trapping probabilities for vacancies on sites within 8 lattice units (LU) from the implant. An estimate of the initial implant-vacancy separation follows from collision cascade simulations with Marlowe [3].

### 3.1.2. STATIC LATTICE CALCULATIONS.

In the static lattice calculations a small bcc crystallite of  $17 \times 17 \times 17$  LU<sup>3</sup>, containing a defect in the centre, relaxes to a minimum energy configuration. The vacancy migration energies were found by calculation of the total energies of the relaxed crystallite with a lattice atom fixed at various positions between two vacancies. The results obtained with this method depend on the set of pair-potentials applied. In this study the widely-used Johnson-Wilson short range W-W potential was taken. It should be realized that the migration energy calculated with this potential is about 0.4 eV too low compared with the experimental value [4,5]. Since our interest is the relative preference of vacancy migration for certain directions in a strained crystal, this does not affect our calculations. The W-noble gas potentials were calculated by Baskes [6] applying the Hartree-Fock method. It was found that there are two equivalent barriers for a jump in the  $\langle 111 \rangle$  direction, formed by the two triangles of atoms in a (111) plane through which the moving atom has to migrate. Calculated vacancy migration energies around substitutional noble gas atoms are shown beside the arrows of the so-called transition matrices in fig. 1.



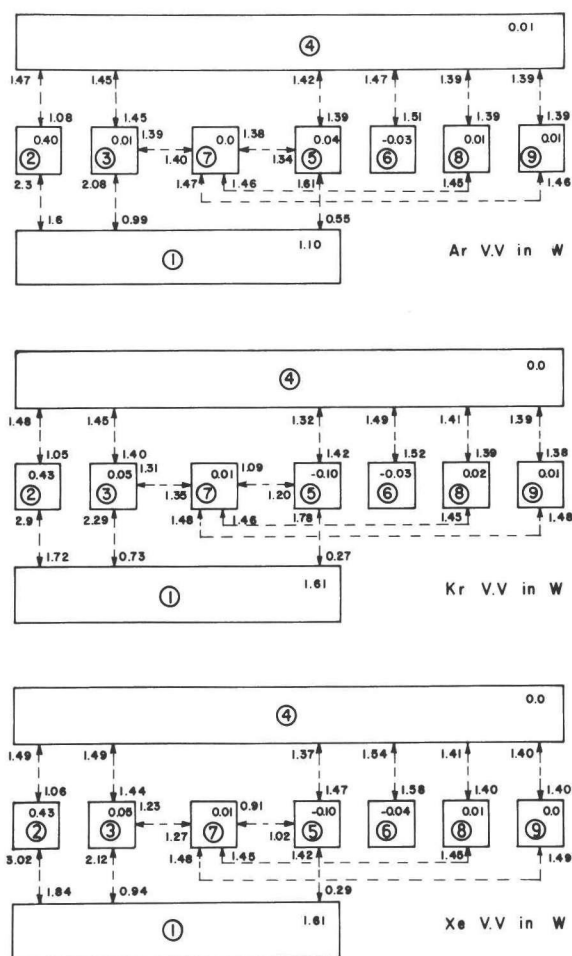


fig. 1: Transition matrix for vacancy jumps in the vicinity of a noble gas atom in tungsten. The encircled number is the separation in nearest neighbour number. The number in the box is the binding energy of the vacancy to the noble gas atom. The numbers labeling the arrows are activation energies for corresponding transitions.

The encircled number in the box indicates which neighbouring position is concerned; 1 is nearest neighbour. The transition matrices are similar to the transition matrices of a V close to a V or HeV [7], except for the jumps from and towards first and second neighbour positions. Qualitatively the trend of lower vacancy migration energies in a strained crystal agrees well with the calculations of Matthai and Bacon [8]. The binding energy of the vacancy on  $n^{\text{th}}$  neighbour position

to the substitutional noble gas atom is shown in the boxes in the right top corner. From the figure a few details can be learned. Firstly the difference in the transition matrices are only very small. Secondly the migration of a third or fifth neighbour vacancy to a first neighbour position is very much enhanced by the implant. This is easily understood bearing in mind the repulsive force which is exerted by the noble gas atom on the neighbouring W atoms.

### 3.1.3. MONTE CARLO CALCULATIONS.

The Monte Carlo approach has been widely used by Fastenau [7] to calculate capture radii for various sink-mobile particle combinations. With this approach the lifetime of a random walker in a box containing only one sink in the centre is calculated. Using correct boundary conditions this is equivalent to a random walker in a periodic array of sinks. The average lifetime  $t_{av}$  is related to the capture constant  $Z$  by comparison with diffusion theory:

$$\frac{d c_m}{d t} = -K c_m c_s = -Z \nu c_m c_s \quad (1)$$

$c_s$  is the sink concentration,  $c_m$  is the concentration of mobile particles,  $K$  is a capture constant which is equal to a trap related capture constant  $Z$  times the jumping frequency of the mobile particle. Transformation to the number of mobile particles and calculation of the average lifetime gives:

$$t_{av} = \frac{1}{Z \nu c_s} \quad (2)$$

where  $1/c_s$  equals the number of atoms in the crystallite used.  $t_{av}$  follows from the Monte Carlo calculations. It should be realized that  $Z$  as calculated depends on the sink concentration  $c_s$ . At lower concentrations  $Z$  approaches the value for infinitely low  $c_s$ . The crystallite size applied then requires a very long calculation time. Therefore the diffusion theory developed by Ham [9] for spherical traps of constant size arranged on a simple cubic superlattice was applied to derive the trapping constant for infinitely low defect concentration  $Z_0$  from  $Z_{c_s}$ . In ref. [7] this derivation is given and shown to be applicable to this problem.

The vacancy was supposed to be trapped once arrived at first or

second neighbour position. In fig. 2 the thus derived capture constants  $Z_0$  for the different implants are shown.

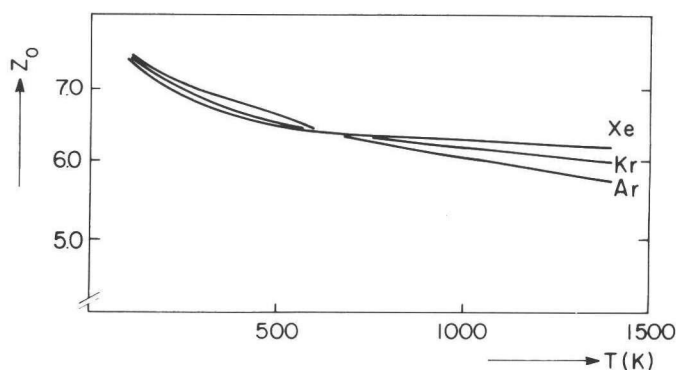


fig. 2: Low sink concentration limit of the capture constant  $Z_0$  for vacancy capture by substitutional noble gas atoms in tungsten as a function of temperature.

The capture constant for an implant not influencing the near-vacancy migration energies is 2.9. It can be seen that at lower temperatures the relative difference in migration energies for different jump directions tends to increase the capture constant  $Z_0$ . At higher temperatures  $Z_0$  is smaller but still much larger than the value for non-preferential jump directions.

Trapping probabilities  $P^V(r)$  of monovacancies starting from positions within 8 LU from the implant were calculated for stage III temperature (here taken as 550 K). The condition for trapping was the same as mentioned above. A vacancy was supposed to be lost for short-range trapping once outside the sphere of 8 LU. It should be realized that trapping probabilities calculated this way only describe trapping of near vacancies. In those cascades where the vacancy concentration within 8 LU of the implant is quite high, vacancy clustering may occur, thus reducing the trapping probability  $P^V(r)$ . For implantations with doses  $> 5 \times 10^{12} \text{ cm}^{-2}$  cascade overlap will occur. All vacancies escaping short range trapping will lead to an increase of the vacancy concentration. These vacancies will cluster, escape at the surface, or be trapped by an implant, but not necessarily the one initiating its formation. Trapping probabilities for different implant-vacancy separations and implants are shown in table 1 for a temperature of 550 K.

table 1: Vacancy trapping probability  $P_v(r)$  for different implant vacancy separations  $r$  and implants.

implant	$r=0-2$	$r=2-4$	$r=4-6$	$r=6-8$
Ar	0.95	0.51	0.18	0.04
Kr	0.95	0.51	0.19	0.04
Xe	0.96	0.51	0.18	0.04
W	0.58	0.18	0.05	0.01

Also shown in the table are the data for an implant not exerting strain in the lattice and thus not influencing the vacancy migration energies. This implant is labelled W.

### 3.1.4. MARLOWE CALCULATIONS.

With the program Marlowe [3] simulations of 5 keV noble gas implantation on W(100) were performed. It was shown recently that the cut-off radius for vacancy/self interstitial recombination should be quite large to predict correctly experimentally observed vacancy concentrations after implantation. Hou et al. [10] compared Marlowe calculations with THDS measurements on Mo implanted with 1-3 keV light noble gas atoms. They found that a displacement energy  $E^d$  of 33 eV and a cut-off radius of 3.7 LU yielded good agreement between observed and calculated vacancy concentrations. For W we took  $E^d$  40 eV, the cut-off radius was also taken as 3.7 LU.

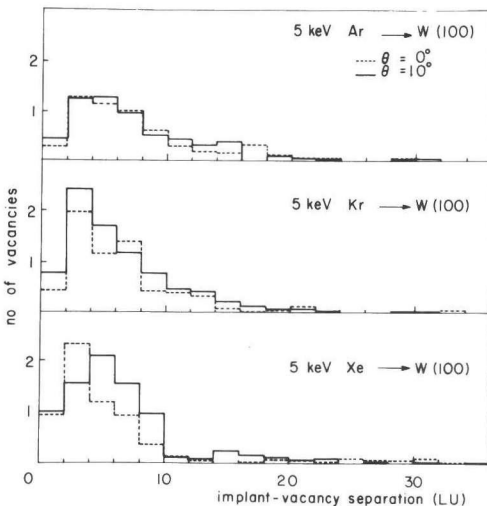


fig. 3: Radial vacancy distribution for 5 keV noble gas atoms implanted into W(100).

In fig. 3 results are shown for 5 keV noble gas atoms impinging perpendicularly on the [100] surface, or 10 degrees off the surface normal. From this figure the trend is clear that the heavier noble gas atoms have a larger fraction of nearby-vacancies than the lighter ones. This can be understood by realizing that energy-transfer to lattice atoms is more favourable due to the smaller mass difference between the projectile and target atoms, not only on impinging the surface but also on the final collisions of the implant. By analyzing the individual cascades with respect to the radial vacancy distributions and the calculated trapping probabilities (table 1) the fraction of  $XV_n$  formed after annealing to stage III was calculated ( $XV$  represents substitutional Ar, Kr or Xe).

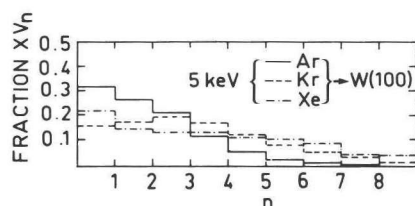


fig. 4: The fraction  $XV_n$  after annealing up to stage III, based on the vacancy distribution averaged over normal incidence and  $10^\circ$  off the [001] channel.

In fig. 4 fractions  $XV_n$  for the different projectiles are shown. For Ar a substitutional fraction of 30% is obtained after annealing to stage III. For Kr and Xe substitutional fractions of about 20% were obtained after annealing. It should be realized that since vacancy clustering has been omitted (see section 3) trapping probabilities  $P^V(r)$  for higher local vacancy concentrations will be overestimated. Thus especially the fractions  $XV_n$  with larger  $n$  will be overestimated.

### 3.1.5. DISCUSSION.

Several implicit hypotheses were made in the calculations which might influence the results. The trapping probabilities followed from calculated migration energies. Since the migration energies were calculated in a static way with a relaxed lattice the real enhancement of certain jumps may be different, leading to other results. A lower limit for the trapping probabilities is given in table 1.

In the analysis of the Marlowe results we used the cut-off radius for vacancy/self interstitial recombination, obtained from the experi-

mental vacancy per ion ratio for light ion bombardment. Since the energy transfer to the lattice atoms is higher for heavier ions, more vacancies are produced. Effectively the concept of cut-off radius represents a survival probability for vacancies in the vicinity of self-interstitials. Therefore we assume that the value derived by ref. [10] is also valid for the somewhat higher defect concentration in this study.

In the as-implanted samples with THDS virtually no substitutional implants are seen, whereas with Mössbauer and PAC substitutional fractions between 50% and 90% are detected [2,11,12]. We believe that this discrepancy is caused by the presence of nearby vacancies. According to Marlowe calculations there are 1 or 2 vacancies within 2 LU. Vacancies located between 1 and 2 LU from the implant will prevent detection of the implant with THDS, whereas these vacancies will not affect the Mössbauer and PAC results. After annealing to stage III Mössbauer and PAC show substitutional fractions of 10 to 30%, which agrees well with the results shown in fig. 4. With THDS all near vacancies should be removed before substitutional implants can be detected.

Finally we would like to comment on the interpretation of the Mössbauer results of refs. [11] and [12]. After implantation of W with 85 keV Xe the annealing behaviour is followed. In the annealing curves different sites are distinguished which are not consistent with the results presented above. After implantation fractions of 40% XeV, 4% XeV<sub>2</sub> and 18% XeV<sub>3</sub> are found in ref. [11], and fractions of 65% XeV, 0% XeV<sub>2</sub> and 20% XeV<sub>3</sub> are found in ref. [12]. The remaining Xe atoms are located in larger vacancy clusters. Furthermore the defect labelled XeV<sub>2</sub> in [11] and XeV<sub>4</sub> in [12] disappears after annealing to 100 K above stage III temperature, whereas the fraction XeV<sub>3</sub> grows drastically. This is not in agreement with the results presented in fig. 4.

Therefore we propose that the so called XeV<sub>2</sub> [11] or XeV<sub>4</sub> [12] is a XeV<sub>2</sub>(2), a substitutional Xe atom with a vacancy at second neighbour position, whereas the so called XeV<sub>3</sub> will be a XeV<sub>2</sub>(1), a substitutional Xe atom with a first neighbour vacancy. The early disappearance of the XeV<sub>2</sub>(2) can be understood by reading the XeV-V transition matrix. A second neighbour vacancy is bound with 0.4 eV, so after annealing to a temperature slightly beyond stage III a XeV<sub>2</sub>(2) will be transformed into a XeV<sub>2</sub>(1) either directly or by migration of the vacancy to the fourth neighbour position, and from there across third or fifth to first neighbour position.

We are grateful to Dr. M. Hou (Université Libre, Bruxelles, Belgium) for helpful discussions.

This work is part of the research programme of the Stichting voor Fundamenteel Onderzoek der Materie (Foundation for Fundamental Research on Matter) and is supported financially by the Nederlandse Organisatie voor Zuiver Wetenschappelijk Onderzoek (Netherlands Organization for the Advancement of Pure Research).

#### REFERENCES.

- [ 1 ] A. van Veen, W.Th.M. Buters, G.J. van der Kolk, L.M. Caspers and T.R. Armstrong, Nucl. Instr. and Meth. 194,485(1982).
- [ 2 ] K. Post, F. Pleiter, G.J. van der Kolk, A. van Veen, L.M. Caspers and J.Th.M. de Hosson, Hyperf. Int. 15/16,421(1983).
- [ 3 ] M.T. Robinson and H. Torrens, Phys. Rev. B9,5008(1974).
- [ 4 ] R.A. Johnson and W.D. Wilson in Interatomic Potentials and Simulation of Lattice Defects, eds. P.C. Gehlen, J.R. Beeler Jr. and R.I. Jaffee (Plenum Press, New York 1972) p. 301.
- [ 5 ] K.D. Rasch, R.W. Siegel and H. Schultz, Phil. Mag. A41,91(1980).
- [ 6 ] M. Baskes, private communication.
- [ 7 ] R.H.J. Fastenau, A. van Veen, P. Penning and L.M. Caspers, Phys. Stat. Sol. 47(a),557(1978).
- [ 8 ] C.C. Matthai and D.J. Bacon, J. of Nucl. Mat. 114,22(1983).
- [ 9 ] F.S. Ham, J. Phys. Chem. Sol. 6,335(1958), J. of Appl. Phys. 30,915(1959).
- [ 10 ] M. Hou, A. van Veen, L.M. Caspers and M.R. Ypma, Nucl. Instr. and Meth. 209/210,19(1983).
- [ 11 ] S.R. Reintsema, E. Verbiest, J. Odeurs and H. Pattyn, J. Phys. F, 9,1511(1979).
- [ 12 ] E. Verbiest, Dr. Thesis, Leuven, Belgium (1983).





### 3.2. EFFECTS OF VACANCIES NEAR SUBSTITUTIONAL IMPLANTS ON TRAPPING AND DESORPTION OF HELIUM; A SIMULATION.

G.J. van der Kolk<sup>1</sup>, A. van Veen<sup>1</sup>, J.Th.M. de Hosson<sup>2</sup> and R.H.J. Fastenau<sup>3</sup>.

<sup>1</sup> Delft University of Technology/Interuniversity Reactor Institute, Mekelweg 15, 2629 JB Delft, the Netherlands.

<sup>2</sup> University of Groningen, Materials Science Centre, Nijenborgh 18, 9747 AG Groningen, the Netherlands.

<sup>3</sup> Philips Research Laboratories, 5600 MD Eindhoven, the Netherlands.

#### ABSTRACT

Trapping of He by vacancies and drainage of He from substitutional implants (Ag and Kr in W) to nearby vacancies are investigated using static lattice calculations. The calculations indicate that drainage of He will occur to vacancies within a radius of 2.5 lattice units from the implant. Furthermore the trapping probability of substitutional and interstitial random walkers on a bcc lattice by substitutional traps or vacancies is calculated. When implantation-produced vacancies are present in the vicinity of the observed trap a shielding effect occurs. Trapping constants are calculated with two random walk models for both the unshielded and the shielded defect. For the latter several configurations were taken. The results show that shielding of a defect by one vacancy at a distance of three lattice units leads already to a reduction of He trapping by that defect of 30% to 40 %.

#### 3.2.1. INTRODUCTION.

In radiation-damage experiments particles are often used as probes for defects e.g. He atoms in Thermal Helium Desorption Spectrometry (THDS). In THDS He is injected with low energy. After initial penetration of the surface to a depth of several tens of Angstroms, the He atoms thermalize and start a random walk, see ref. [1,2]. A small fraction of the He atoms is trapped by defects present, the majority escapes at the surface.

For specific defects in the presence of other defects shielding effects will occur, leading to a reduced trapping probability of the

random walker by those defects. Especially in the case of damage introduction by ion implantation defects are not distributed homogeneously despite the low doses often applied: defects made in a single collision cascade are often close to each other. Recent experiments in which Perturbed Angular Correlation (PAC) was compared with THDS to investigate defects in W after 25 keV Ag implantation at low doses ( $<10^{13} \text{ Ag}^+ \text{ cm}^{-2}$ ) demonstrate this [3]. PAC reveals a near 100 % substitutional fraction of Ag after implantation, whereas with THDS substitutional implants can only be detected after annealing to 1400 K. Since with PAC the decay of an active Ag atom is observed, this method will only probe the Ag atom and its immediate surroundings. The discrepancy can be explained assuming the presence of nearby vacancies at Ag which either shield Ag for the migrating He atom or which may cause drainage of He trapped at Ag to nearby vacancies or which retrap dissociated He. In a preceding study it was shown with binary collision cascade simulations that indeed an average of one to three nearby vacancies may be expected within a distance of four lattice units from the implanted atom [4]. During annealing a large fraction (40-60 %) of these vacancies will migrate to the implant, as observed with PAC.

In section 2 attention is given to the possibility of He drainage from implanted atoms to nearby vacancies and retrapping of He in nearby vacancies during the desorption step in THDS.

The situation prior to annealing is taken to calculate the shielding effects of nearby vacancies on He trapping by implanted atoms (section 3). Different vacancy-implant separations and configurations were taken and studied with random walk simulations.

### 3.2.2. HE DRAINAGE FROM IMPLANTS TO NEARBY V.

#### 3.2.2.1. Static lattice calculations.

Static lattice calculations were used to calculate trapping positions, dissociation paths and dissociation energies of He at a vacancy, at a substitutional Kr atom and at a substitutional Ag atom in W. The defects were placed in the centre of a small crystallite ( $17 \times 17 \times 17 a_0^3$  with  $a_0$  the lattice constant). The W-W potential describing the pair interaction of the tungsten atoms was fitted to elastic constants by Johnson and Wilson [5]. The He-Kr, He-W and Kr-W potentials were calculated by Baskes [6] using the modified Wedepohl method [7,8]. The

Ag-W potential was obtained by scaling of the W-W potential [9]. The He-Ag potential was constructed using the modified Wedepohl method [8,9]. Dissociation and migration energies were obtained by calculating the total energy of the crystallite with the dissociating or migrating particle held fixed at various positions along the dissociation respectively migration path. The crystallite was allowed to relax fully.

### 3.2.2.2. Trapping of He at V and KrV/AgV.

According to calculations of ref. [5] He in W migrates from octahedral across tetrahedral to octahedral position energies with a migration of 0.25 eV (the octahedral position is the midpoint of the edge of the bcc cell, the tetrahedral position is the midpoint between two neighbouring octahedral positions). energy of 0.25 eV. This allows the He atom to jump in four directions with jumping distance  $a_0/2$ . The nearest octahedral and lattice positions at a trap are shown and labelled in figs. 1a and 1b and table 1.

table 1: Coordinates in  $a_0/2$  of the  $n^{\text{th}}$  nearest neighbour position with respect to site (0,0,0) for lattice positions (V's) and octahedral positions (He) in a bcc lattice.

n	V	He
1	(1,1,1)	(1,0,0)
2	(2,0,0)	(1,1,0)
3	(2,2,0)	(2,1,0)
4	(3,1,1)	(2,1,1)
5	(2,2,2)	a (2,2,1) b (3,0,0)
6	(4,0,0)	(3,1,0)
7	(3,3,1)	(3,2,0)
8	(4,2,0)	(3,2,1)
9	(4,2,2)	a (3,2,2) b (4,1,0)
10	a (3,3,3) b (5,1,1)	a (3,3,0) b (4,1,1)

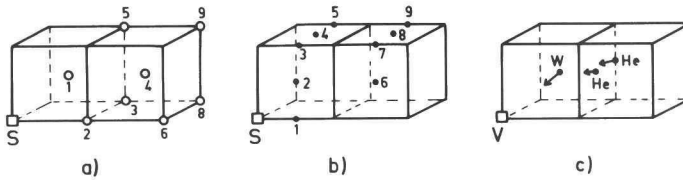


fig. 1: The nearest lattice positions (a) and octahedral positions (b) at a sink S and a schematic representation of He assisted vacancy jumping (c).

Units of  $a_0/2$  are used further in the text. For a vacancy as trap and He as migrating particle the octahedral site 2 is a trapping position. For site 3 being a trapping position either migration of He to site 2 or migration of the lattice atom at  $(2,0,0)$  to the vacancy at  $(0,0,0)$  with He simultaneously jumping into the newly-created vacancy is required. The first process is calculated to have the same tetrahedral saddlepoint energy as for bulk migration of He. The latter reaction, He assisted vacancy jumping, has been investigated by Wilson and Bisson [10]. They found that it requires the same energy as bulk vacancy migration. Thus site 3 can be excluded as He trapping position. For He positioned at site 4 and site 5a calculations were also performed on the energy required to move the atom at  $(1,1,1)$  into the vacancy. The energies relative to the energy of the crystallite with He trapped in a vacancy (V) are shown in fig. 2.

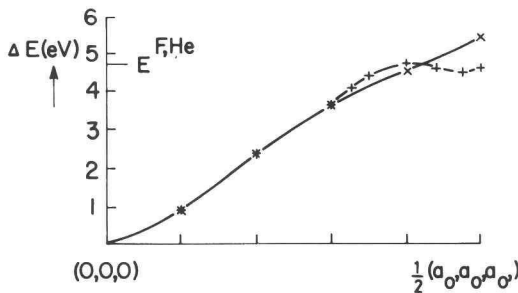


fig. 2: Migration energy of a W atom along the  $\langle 111 \rangle$  direction near a vacancy at  $(0,0,0)$  in the presence of a He atom, initially at site 4 (x), or at site 5a (+). Both He and the surrounding W atoms were allowed to relax fully.

It should be noted that ref. [10] had already calculated this for the first position, but for He fixed at that position. In our calculations the tungsten atom was fixed at positions along the line connecting (0,0,0) and (1,1,1), He and the surrounding lattice atoms were allowed to relax fully.

The results indicate that He at positions 4 and 5a will push the tungsten atom into the vacancy, thereby itself being trapped by the newly formed vacancy. The reaction is visualised in fig. 1c.

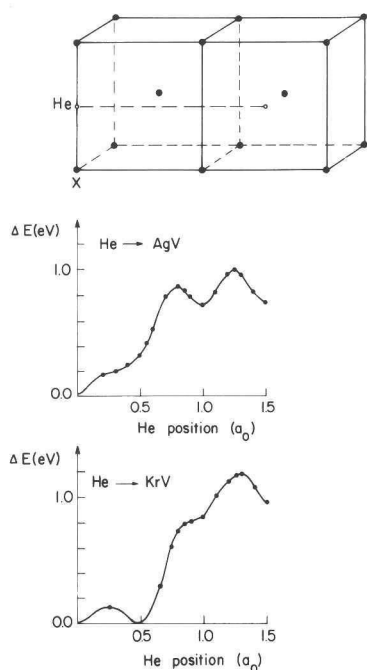


fig. 3: Energy variation of a W crystallite with He fixed at various positions along the [100] axis close to substitutional Ag and Kr.

In fig. 3 energy variations are shown of the crystallite if a He atom is moved along the path connecting the position of He trapped at substitutional Ag or Kr and the octahedral site 6 of fig. 1a. From the figure it clearly follows that site 3 (in the figure He at  $a_0$ ) is a trapping position for He.

### 3.2.2.3. Drainage of He from KrV/AgV to and retrapping in nearby V/HeV.

Drainage either at room temperature or during desorption takes place when the energy required for He to reach a nearby V or nearby HeV is below the normal dissociation energy.

Instead of calculating all possible drainage paths in the vicinity of a V we followed a simplified approach. We assumed that the energy variation as calculated in section 2.2 (fig. 3) for He dissociating from KrV or AgV will not be altered by a nearby V. Then the problem of finding the drainage paths is reduced to determining all trapping positions for He at an  $n^{\text{th}}$  neighbour V which can be reached by He originally trapped at KrV/AgV with an energy lower than the bulk dissociation energy. For instance a V at a 4<sup>th</sup> neighbour position (table 1) relative to a KrV will migrate spontaneously to a 2<sup>nd</sup> neighbour position if a He atom is trapped at a KrV and therefore may be at (1,1,0). For a few drainage reactions (5<sup>th</sup> and 7<sup>th</sup> neighbour V) the energy variation along the He migration path was followed. For Ag the rule held well, for Kr the rule slightly overestimated the required energies ( $\sim 0.05$  eV).

table 2: Energies required for He drainage reactions. Figures between brackets indicate  $n^{\text{th}}$  neighbour lattice positions.

reaction	energy (eV)
HeKrV $\rightarrow$ KrV + He *	1.16
HeKrV.V(n) $\rightarrow$ KrV.HeV(n) n=1,2	0
HeKrV.V(n) $\rightarrow$ KrV.HeV(1) n=3,5	0
HeKrV.V(4) $\rightarrow$ KrV.HeV(2)	0
HeKrV.V(7) $\rightarrow$ KrV.HeV(3)	0.13
HeKrV.V(n) $\rightarrow$ KrV.HeV(4) n=8,9	0.85
HeAgV $\rightarrow$ AgV + He *	1.00
HeAgV.V(n) $\rightarrow$ AgV.HeV(n) n=1,2	0
HeAgV.V(n) $\rightarrow$ AgV.HeV(1) n=3,5	0
HeAgV.V(4) $\rightarrow$ AgV.HeV(2)	0
HeAgV.V(7) $\rightarrow$ AgV.HeV(3)	0.35
HeAgV.V(n) $\rightarrow$ AgV.HeV(4) n=8,9	0.90
HeKrV.HeV(n) $\rightarrow$ KrV.He <sub>2</sub> V(n) n=1,2,3	0
HeKrV.HeV(4) $\rightarrow$ KrV.He <sub>2</sub> V(4)	0.83
HeAgV.HeV(n) $\rightarrow$ AgV.He <sub>2</sub> V(n) n=1,2	0
HeAgV.HeV(3) $\rightarrow$ AgV.He <sub>2</sub> V(3)	0.14
HeAgV.HeV(4) $\rightarrow$ AgV.He <sub>2</sub> V(4)	0.76
HeAgV.HeV(5) $\rightarrow$ AgV.He <sub>2</sub> V(5)	0.95

\* dissociation reaction

In table 2 all drainage reactions which will occur are shown. Energies required for the reactions are also shown. It is clearly demonstrated that drainage is quite effective, especially for He from KrV to a nearby V. For AgV drainage of He under influence of an 8<sup>th</sup> or 9<sup>th</sup> neighbour V is only slightly favoured above normal dissociation. It should be realized that if more strain is present, as may be expected when a larger impurity atom is involved or when more than one He atoms are trapped, drainage of He under influence of an 8<sup>th</sup> or 9<sup>th</sup> neighbour V will be more favoured.

Drainage of He to a nearby HeV is less effective because the phenomenon that He pushes a W atom in the nearby vacancy will not occur as pictured here. We assume that the trapping positions relative to the HeV are thus limited to octahedral sites 2. Calculations of He migration paths were performed. The results indicate that beside the first, second and third neighbour HeV drainage also takes place to a fourth neighbour HeV. For the fifth neighbour HeV only very slight enhanced drainage was found in the case of AgV, see table 2.

For a nearby V to which drainage does not take place still a rather high probability exists of spontaneous retrapping of He after dissociation from an XV (X=Ag, Kr). In [11] it is shown that the probability of trapping in a near sink with sink radius  $r_s$  at distance R versus escape at infinity is given by  $r_s/R$ . In desorption experiments the surface is nearby, thus the fraction being retrapped after dissociation will be lower. To obtain an estimate of this effect a simple random walk model was applied. A random walker started a 1000 times at octahedral positions around the origin in a box of  $16 \times 16 \times 16$   $a_0^3$  containing a vacancy at a certain distance from the origin.

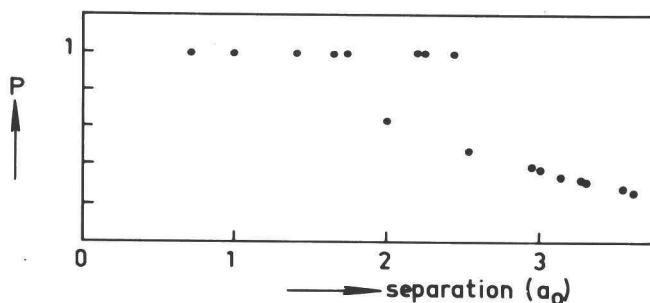


fig. 4: Probability P for He, initially trapped at XV (X=Ag,Kr), to be trapped in a V, either spontaneously or during annealing, as a function of XV-V separation.

Capture criteria for He close to a V followed from section 2.2, the random walker is assumed to escape if at the edge of the box. The trapping probabilities calculated this way, combined with the drainage probabilities, for different XV-V separations, are used to obtain the fraction of He atoms trapped in a V after initially being trapped in a XV. The result is shown in fig. 4.

### 3.2.3. RANDOM WALK SIMULATIONS.

#### 3.2.3.1. Periodically arranged traps.

In the preceding study [4] concerning vacancy trapping by substitutional noble gas atoms a random walk model was used which could be related with diffusion theory to obtain effective trapping constants for defects. Hitherto the average lifetime  $t_{av,rw}$  of a random walker in a periodic array of spherical sinks with concentration  $c_s$  was calculated.  $t_{av,rw}$  thus calculated was compared with the average lifetime  $t_{av,d}$  of a particle diffusing in a sphere with boundary conditions  $dc/dt=0$  for  $x=R$ , with  $R$  the radius of the sphere, and  $c=0$  for  $x \leq r$ , so that  $r$  is the trapping radius of the defect. The solution of this problem is given by Ham [12]. Fastenau et al. [13,14] compared the diffusion theory with random walk results for different random walker-defect combinations. Interaction of vacancies, self interstitials and He atoms with vacancies were simulated by them. In this study we are mainly interested in He interaction with defects. To simulate the shielding of implanted atoms by vacancies we introduced an extended sink, composed of different traps, in the centre of a crystallite. He atoms leaving the box are entering it at the opposite side of the box, so that the box is equivalent with periodically arranged traps, see also [13,15]. For sinks three different trapping radii were taken, in accordance with the calculations in section 2.2. For empty vacancies a rather large trapping volume was taken, see table 3.

table 3: Trapping sites in  $a_0/2$  coordinates and calculated trapping constants for interaction of He with various defects.

defect	trapping sites	$Z_0$
V	(1,1,0) (2,1,1) (2,2,1)	1.41
HeV	(1,1,0)	0.73
XV, X=Ag,Kr	(2,1,0)	1.15
$V_2(1), V_2(2)$	as for V	1.67
$V_3(112)$	as for V	1.72
$V_4(111122)$	as for V	1.87



For a vacancy filled with a small impurity, here HeV, only the site (1,1,0) was taken, whereas for larger impurities also the site at (2,1,0) was taken as trapping position. The average number of jumps  $n_{av}$  for a He atom to be trapped, starting at a random position within the crystallite, was calculated. From diffusion theory the relation between  $n_{av}$  and the trapping constant  $Z_{eff}$  is obtained as follows:

$$\frac{dc_m}{dt} = -Z_{eff} \cdot \nu \cdot c_s \cdot c_m \quad (1a)$$

where  $\nu$  is the jumping frequency,  $c_m$  the concentration of random walkers,  $c_s$  the sink concentration and  $Z_{eff}$  the trapping constant. Calculation of the average lifetime  $t_{av}$  and taking  $n_{av} = t_{av} \cdot \nu$  it follows:

$$Z_{eff} = \frac{1}{t_{av} \nu c_s} = \frac{1}{n_{av} c_s} \quad (1b)$$

The trapping constant  $Z_0$  for infinitely low sink concentration  $c_s$  and octahedral random walkers on a bcc lattice was calculated by refs. [12,13,14] to depend on  $Z_{eff}$  according to the following relation:

$$Z_0 = \frac{\pi(R\alpha - \arctg R\alpha)}{3\alpha} \quad (2a)$$

with  $R$  the radius in  $a_0$  of the sphere corresponding with  $1/c_s$  atoms,  $\alpha$  is given by:

$$\alpha = \left\{ \frac{9Z_{eff}}{\pi R^3} \right\}^{0.5} \quad (2b)$$

An access factor  $A_{i,j}$  for a sink  $U_i$  near another sink  $U_j$  with a total sink concentration approaching zero can be defined:

$$A_{i,j} = \frac{f_i Z_{oi,j}}{Z_{oi}} \quad (3a)$$

with  $Z_{oi,j}$  the trapping constant for the extended sink composed of defects  $U_i$  and  $U_j$  and  $f_i$  the fraction of random walkers trapped in defect  $U_i$ . An alternative definition is:

$$A_{i,j} = \frac{f_i Z_{eff,i,j}}{Z_{eff,i}} \quad (3b)$$

$Z_{\text{eff},i}$  represents the trapping constant for defect  $U_i$  at a sink concentration which corresponds with the sink concentration in the case of defect  $U_j$  near  $U_i$ , with  $U_i$  and  $U_j$  counted as separate sinks. The definition has only physical meaning for equal sinks  $U_i$  and  $U_j$ .

The average number of jumps required for trapping  $n_{\text{av}}$  was calculated for a sink in the centre of a box of  $12 \times 12 \times 12 a_0^3$ . The octahedral random walker was released 3000 times at random positions within the box, trapping positions excluded, for every defect configuration. Thus obtained  $n_{\text{av}}$  s were substituted in equations (1) (2) and (3) to calculate access factors for V near V, HeV near V, XV near V and XV near HeV, see fig. 5.

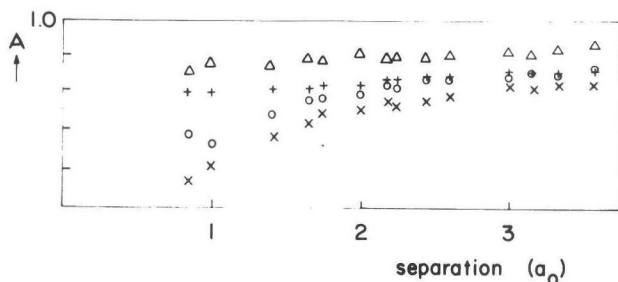


fig. 5: Access factors of V near V (+), HeV near V (x), XV near V (o) and XV near HeV ( $\Delta$ ) for octahedral random walkers on a bcc lattice as a function of separation.

For those trapping sites around a HeV or XV at which He can be trapped by the V as well preference is given to trapping by the V. The trapping constants at infinitely low concentration and the trapping sites are given in table 3. The access factor is typically between 0.4 and 0.6 depending on the combination and separation. For two HeV s also a calculation was performed for a larger separation. The value of A approaches 1 as may be expected. In fig. 6 the access factors of V s and XV s near a di- and tri-vacancy are shown.

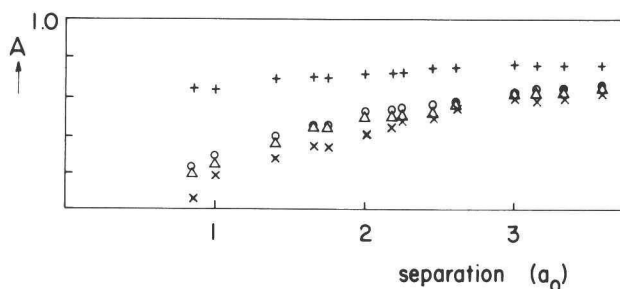


fig. 6: Access factors of V near  $V_2$  (+), XV near  $V_2(1)$  or  $V_2(2)$  (o), XV near  $V_3(112)$  ( $\Delta$ ) and HeV near  $V_2$  (x), further as in fig. 5.

Again for octahedral sites within trapping distance of both defects the di- or trivacancy was supposed to be the stronger trap. The distance between the nearest vacancy of the di- or trivacancy and the sink is taken as separation. The divacancy was taken either as  $V_2(1)$  or  $V_2(2)$ ; a nearest neighbour  $V_2$  or a second nearest neighbour  $V_2$ . For the trivacancy the most stable one was taken;  $V_3(112)$  according to refs. [16,17]. In fig. 7 the fraction He trapped by XV in the presence of V,  $V_2$  and  $V_3$  is shown.

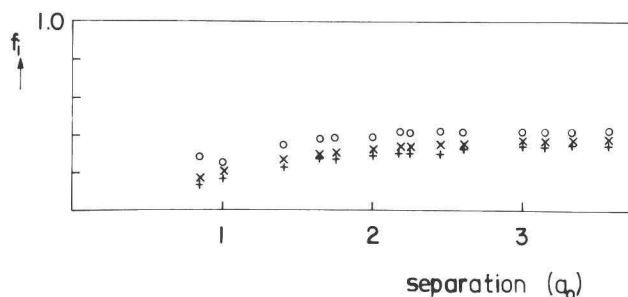


fig. 7: Fraction of octahedral random walkers trapped by XV in the presence of V (o),  $V_2(x)$  and  $V_3(+)$  as a function of separation.

To investigate the dependence of the access factors on the total sink concentration for a first to tenth neighbour divacancy calculations of the (imaginary) mutual shielding were performed for different sink concentrations using equation (3b). In fig. 8 a few illustrative results are shown.

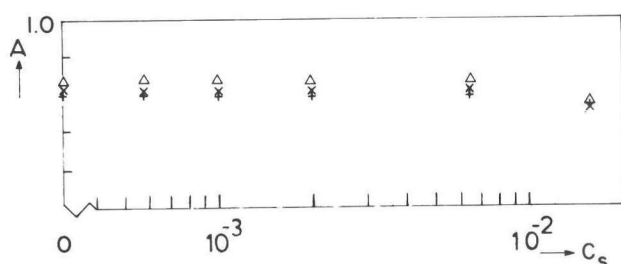


fig. 8: Access factor for V near V as a function of the sink concentration, (+) first neighbour separation, (x) third neighbour and ( $\Delta$ ) ninth neighbour separation.

Access factors at infinitely low concentration are also shown. It should be noted that the coincidence of the access factors at concentration zero with the factors at  $5.8 \times 10^{-4}$  reflects the fact that  $Z_0$  was calculated from  $n_{av}$  at this concentration. The figure demonstrates that (3b), if applicable, is equivalent with (3a). Deviations occur if the size of the extended sink is not small compared with the size of the crystallite.

The periodicity of the sinks in general leads to a higher  $Z_{eff}$  than for randomly distributed sinks with a similar concentration. In ref. [18]  $Z_{eff}$  for He trapping by vacancies for both cases was calculated. For sink concentrations below  $10^{-3}$  the two values approach each other. So we expect that the shielding factors found above for the periodic arrangement differ little from shielding factors for random sink arrangements at vacancy concentrations below  $10^{-3}$ .

### 3.2.3.2. Shielding at infinitely low defect concentration.

To calculate the effective shielding directly at infinitely low defect concentration another approach can be used. Consider the trapping positions around defect and neighbouring vacancies again as an extended sink. It was shown by Soos and Powell [19] that the random walk of a point defect in a crystal containing  $m$  extended defects is equivalent with the random walk of an extended sink (including all trapping positions) in a crystal containing  $m$  immobile point defects. Fastenau et al [14,20] used this concept, but now only the number of "fresh" sites  $S_n(U_j)$  the extended sink  $U_j$  had encountered after  $n$  steps was investigated. Montroll and Weiss [21] already showed that

for low point defect concentrations  $S_n(U_j)$  can be approximated with:

$$S_n(U_j) = b(U_j).n + c(U_j).vn + d(U_j) \quad (4)$$

$b(U_j)$ ,  $c(U_j)$  and  $d(U_j)$  are coefficients of the series expansion of  $S_n$  [14]. The physical meaning of relation (4) is that  $b(U_j)$  equals  $Z_0$ , see refs. [14,20]. It may be assumed that (4) is also valid for extended defects in three dimensions.

To calculate effective shielding factors for different defect configurations the number of fresh sites encountered by the composite defect as obtained with random walk was fitted with equation (4). By distinguishing the number of fresh sites encountered by the shielded and the shielding defects and applying (3a) on the  $Z_{0,j}$  found the access factor  $A$  is obtained.

Since He migrates interstitially random walkers on an imaginary lattice should be concerned, Koiwa and Ishioka [22,23,24] have treated this problem in a series of articles for point defects. Their theoretically obtained results agree with the random walk calculations of Fastenau (Koiwa:  $b=0.5713$ , Fastenau:  $b=0.567$ ). For extended defects however the concept of an octahedral walking sink instead of octahedral walking point defect cannot be applied in a straightforward manner. All octahedral trapping positions around the extended sink should perform an octahedral random walk. Thereby they necessarily cross lattice positions which never could have been visited by He atoms. Although this problem can be solved, it requires considerably greater calculation time, especially if the more realistic larger trapping radius is taken, and thus we limited ourselves here to random walkers on lattice positions. The random walker was supposed to be trapped once it arrived at first neighbour position of the trap. Jumps were made to first neighbour positions. Physically this coincides with vacancy migration. For some defects the data thus obtained are shown in fig. 9.

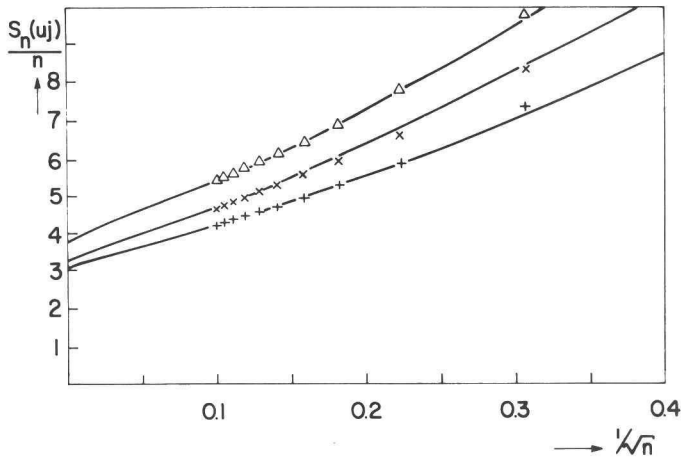


fig. 9:  $S_n(U_j)/n$  versus  $\sqrt{n}$  for  $n^{\text{th}}$  neighbour divacancies, (+)  $n=1$ , (x)  $n=3$  and ( $\Delta$ )  $n=9$ , marked points are obtained with Monte Carlo simulations, drawn curves are best fits using equation (4).

Best fits using relation (4) are drawn.  $b(U_j)$  is typically about 2 to 3 times higher than for an octahedral random walker reflecting that the latter can only sample two new lattice positions, whereas the random walker taken here can sample 7 new lattice positions per step. The data thus obtained for  $b(U_j)$ ,  $c(U_j)$ ,  $d(U_j)$  and the access factor  $A$  are shown in table 4. It can be seen that the access factors are quite similar to the ones calculated in section 3.1.

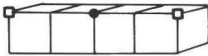
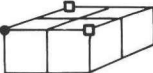

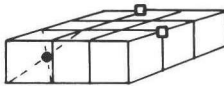
table 4: Parameters describing the random walk of an extended sink on a bcc lattice as obtained with (4) from Monte Carlo simulations and access factors  $A$ . Defects were allowed to jump in the  $\langle 111 \rangle$  direction. All first neighbour positions were taken as trapping positions.

defect	$b(U_j)$	$c(U_j)$	$d(U_j)$	$A$
V	2.42	7.97	2.02	--
$V_2(1)$	3.06	10.44	9.35	0.63
$V_2(2)$	3.17	10.38	7.91	0.65
$V_2(3)$	3.23	13.75	10.16	0.67
$V_2(4)$	3.45	14.17	7.30	0.71
$V_2(5)$	3.50	13.51	10.16	0.72
$V_2(6)$	3.73	13.46	13.19	0.77
$V_2(7)$	3.78	13.64	13.75	0.78
$V_2(8)$	3.66	16.53	5.77	0.76
$V_2(9)$	3.83	14.77	13.24	0.79

### 3.2.3.3. Shielding of defects by more than one V.

Using the model presented in section 3.1 the effect of different near vacancy configurations was calculated. Crystallite size is taken the same, as well as trapping sites for the octahedral random walker. In table 5 the access factors are shown together with the corresponding defect configurations. For two V s diametrically positioned relative to XV the shielding effect is nearly twice as large as for a single V. For two nondiametrical V s the shielding effect is less than twice as large.

table 5: Access factors of XV near several vacancies for octahedral random walkers on a bcc lattice, X=Ag, Kr. The positions of the V s relative to XV are schematically indicated.

relative positions of V ( $\square$ ) and XV ( $\bullet$ )	A
	0.24
	0.34
	0.42
	0.48

### 3.2.4. DISCUSSION.

In general the pair-potential results presented in section 2 will give only a qualitative insight in the processes occurring. The calculated vacancy migration energy of 1.46 eV and the calculated dissociation energy for He from KrV of 1.16 eV are lower than the experimental values (1.8 and 1.7 eV respectively, as derived from the spectra in [25]). We do believe however that the phenomenon of He-assisted vacancy jumping takes place, experimental evidence for this phenomenon is that the reverse reaction (He dissociation) probably takes place in a

similar way. Dissociation of He from a singly-filled V in W and Mo can only be described by substitution of a pre-exponential factor in the Arrhenius formula for first order desorption which is a factor 100 larger than for vacancies filled with 3 or more He atoms [26,27]. Armstrong et al. [26] proposed that this reflects the higher entropy factor for a process in which a surrounding lattice atom jumps into the vacancy and pushes He out, rather than jumping of He alone. Trapping positions for He around KrV and AgV were also calculated.

The random walk results presented in section 3 are quantitatively reliable. The only uncertainties come from the presumptions concerning the trapping positions. This affects the magnitude of the shielding effect, as can be seen for the various defects with different trapping radii.

Since heating is essential in the experimental scheme of THDS all (thermally activated) drainage reactions requiring a lower energy than bulk dissociation will lead to He desorbing from a V in the experiment. Thus according to the pair-potential calculations only those substitutional implants will be detected with THDS which have either no vacancies within  $2.5 a_0$  or only at the sixth neighbour position. Furthermore it should be realized that there are only 6 of those out of the  $128 n^{\text{th}}$  neighbour positions with  $n \leq 9$ . Together with the shielding of the sixth neighbour and the retrapping probability of about 0.6 this means that only about 1 percent of the substitutional implants with a vacancy within  $2.5 a_0$  will be detected. Various detection probabilities are schematically shown in fig. 10.

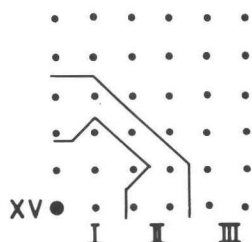


fig. 10: Detectability of XV in the presence of V with THDS; presence of a V in zone 1 prevents detection; in zone 2, less than 50% will be detected; in zone 3, more than 50% will be detected.

The results presented in [4] indeed indicate that on the average one vacancy will be present within this distance already at implantation energies of 5 keV for the heavier noble gases in tungsten. So we may assume that the discrepancies between THDS on the one hand, where after implantation only some 5% to 10% of the implants is seen in a



substitutional position, and PAC [3] and Mössbauer [28,29] results on the other hand where substitutional fractions between 50% and 90% are seen after implantation, are largely due to combined He drainage and He-assisted vacancy jumping. Retrapping and shielding effects play an additional role.

The results presented here also indicate that if THDS is used to deduce total amounts of vacancies produced during heavy ion bombardment, it will tend to underestimate the total number of vacancies produced. The order of magnitude of underestimation will depend on the local vacancy density in the cascade. Especially if vacancy-clustering occurs, the underestimate will be quite drastic. It should be noted that the shielding depends on the He filling degree, a vacancy already filled with a He atom is much less effective in shielding.

This work was part of the research programme of the Stichting voor Fundamenteel Onderzoek der Materie (Foundation for Fundamental Research on Matter) and was supported financially by the Nederlandse Organisatie voor Zuiver Wetenschappelijk Onderzoek (Netherlands Organization for the Advancement of Pure Research).

#### REFERENCES.

- [1] A.A. van Gorkum and E.V. Kornelsen, Rad. Eff. 42,93(1979).
- [2] L.M. Caspers and A. van Veen, Phys. Stat. Sol. (a), 68,339(1981).
- [3] K. Post, F. Pleiter, G.J. van der Kolk, A. van Veen, L.M. Caspers and J.Th.M. de Hosson, proceedings of the sixth International Conference on Hyperfine Interactions, Groningen, the Netherlands 1983, Hyperf. Int. 15/16,421(1983).
- [4] G.J. van der Kolk, A. van Veen, L.M. Caspers and J.Th.M. de Hosson, proceedings of the tenth International Conference on Atomic Collisions in Solids, Bad Iburg, FRG 1983, chapter 3.1.
- [5] R.A. Johnson and W.D. Wilson in Interatomic Potentials and Simulation of Lattice Defects, eds. P.C. Gehlen, J.R. Beeler Jr. and R.I. Jaffee (Plenum Press, New York 1972) p.301.
- [6] M. Baskes, private communication.
- [7] P.T. Wedepohl, Proc. Phys. Soc. 92,79(1967).
- [8] W.D. Wilson and C.L. Bisson, Phys. Rev. B 3,3984(1971).
- [9] G.J. van der Kolk, A. van Veen, L.M. Caspers and J.Th.M. de Hosson, to be published in J. of Nucl. Mat, chapter 4.1.

- [10] W.D. Wilson and C.L. Bisson, Rad. Eff. 19,53(1973).
- [11] A.C. Damask and G.J. Dienes, Point Defects in Metals, New York 1973, pp. 86-88.
- [12] F.S. Ham, J. Phys. Chem. Sol. 6,335(1958).
- [13] R.H.J. Fastenau, A. van Veen, P. Penning and L.M. Caspers, Phys. Stat. Sol. 47(a),557(1978).
- [14] R.H.J. Fastenau, Ph.D. Thesis, Delft 1982.
- [15] T. Leffers and B.N. Singh, Rad. Eff. 59,82(1981).
- [16] R.H.J. Fastenau, L.M. Caspers and A. van Veen, Phys. Stat. Sol 47(a),557(1978).
- [17] K. Masuda, J. Physique 43,921(1982).
- [18] R.H.J. Fastenau, C.M. van Baal, P. Penning and A. van Veen, Phys. Stat. Sol. 52(a),577(1979).
- [19] Z.G. Soos and R.C. Powell, Phys. Rev. B. 6(10),4035(1972).
- [20] R.H.J. Fastenau, Phys. Stat. Sol. 53(a),K39(1979).
- [21] E.W. Montroll and G.H. Weiss, J. of Math. Phys. 6(2),167(1965).
- [22] M. Koiwa, Phil. Mag. 36(4),893(1977).
- [23] S. Ishioka and M. Koiwa, Phil. Mag. 37(4),517(1978).
- [24] M. Koiwa and S. Ishioka, Phil. Mag. 40(5),625(1979).
- [25] E.V. Kornelsen, Rad. Eff. 13,227(1972).
- [26] T.R. Armstrong, A. van Veen and L.M. Caspers, to be published.
- [27] A.A. van Gorkum, J. Appl. Phys. 51(5),2594(1980).
- [28] S.R. Reintsema, E. Verbiest, J. Odeurs and H. Pattyn, J. Phys. F 9,1511(1979).
- [29] E. Verbiest, Dr. Thesis, Leuven, Belgium (1983).

### 3.3. INTERACTION OF VACANCIES WITH IMPLANTED METAL ATOMS IN TUNGSTEN OBSERVED BY MEANS OF THERMAL HELIUM DESORPTION SPECTROMETRY AND PERTURBED ANGULAR CORRELATION MEASUREMENTS.

G.J. van der Kolk<sup>1</sup>, K. Post<sup>2</sup>, A. van Veen<sup>1</sup>, F. Pleiter<sup>2</sup> and J.Th.M. de Hosson<sup>3</sup>.

<sup>1</sup> Delft University of Technology/Interuniversity Reactor Institute, Delft, The Netherlands

<sup>2</sup> Laboratory for General Physics, Materials Science Centre, University of Groningen, The Netherlands

<sup>3</sup> Department of Applied Physics, Materials Science Centre, University of Groningen, The Netherlands.

#### ABSTRACT

With two techniques the defect complexes are studied formed after implantation of 5 to 100 keV metal ions into tungsten. Correlation (PAC) studies clearly indicate the presence of substitutional impurities in samples implanted with Ag or In. With Thermal Helium Desorption Spectrometry (THDS), however, virtually no substitutional implants (Ag,Cu,Mn,Cr,In) could be seen after implantation due to the near vacancies. Migration of vacancies towards the implants during annealing at stage III temperature was observed by means of PAC measurements. At upper stage III vacancy-implant complexes disintegrate, while the substitutional fraction increases. According to THDS, no vacancy-implant complexes are left, in the case of 5 keV implantation after annealing to temperatures slightly beyond stage III temperature. In the case of 20 keV implantation a vacancy-type defect is formed which is stable up to 1350 K. The results of both techniques are compared with each other and with model calculations.

#### 3.3.1. INTRODUCTION.

The interaction of vacancies with impurity atoms in metals is of interest with respect to several engineering problems. We mention the creation of metastable alloys by means of ion implantation to improve surface hardness or corrosion resistance. Another aspect is

the need for alloys that can resist neutron irradiation in a nuclear fusion or fast breeder reactor. Impurities or transmutation products may act as sinks for vacancies and/or interstitials thereby influencing the void growth rate.

In a previous article [1] the interaction of vacancies with Ag implanted into a W(100) single crystal was investigated with Thermal Helium Desorption Spectrometry (THDS). In the present work we extend this study to the implants Cu, Mn, Cr and In. THDS involves the controlled decoration of defect complexes with low energy implanted helium, followed by thermal desorption of bound He. The He release rate is monitored as a function of temperature. A review of THDS and its applications has recently been given by Caspers and van Veen [2].

Perturbed Angular Correlation (PAC) measurements are performed on  $^{111}\text{Ag}$  and  $^{111}\text{In}$  in tungsten. For the other implants no suitable PAC probe atoms exist. The method relies on the measurement of the Electric Field Gradient (EFG) produced by defects at the site of a radioactive nucleus. For details of the method, see ref. [3]. In general, methods using radioactive nuclei are rather powerful for probing defect configurations. A technique like THDS is sensitive to the size of the defect and probes in principle all vacancies created in the collision cascade, but is not able to distinguish between different vacancy-type defect configurations. By using the same combination of implant and host, the results of PAC and THDS experiments can be compared.

In section 2 and 3 we describe the THDS and PAC measurements. In both cases we first briefly discuss the method and thereafter the experimental results. In section 4 model calculations are presented. The first part deals with Marlowe calculations. In the second part we apply simple random walk models to study the migration of vacancies during annealing. In section 5 the results of THDS, PAC and model calculations are compared with each other. Preliminary results have been reported before [4].

### 3.3.2. THDS EXPERIMENTS.

#### 3.3.2.1. Method.

The THDS method has recently been described in various review arti-

cles [2,5,6]. In the following we just give a brief outline of the technique.

After defect introduction, low energy He is injected into the sample with such an energy that no extra damage is introduced. In the case of W, the He implantation energy should therefore be less than 400 eV. The He atoms diffuse rapidly through the crystal and are trapped by defects or escape at the surface. Desorption of the He atoms during linear heating with time yields information on the dissociation energy and the concentration of traps. The experimental equipment has already been described in [1] and [7]. The same W(100) single crystal used in earlier experiments [1] is mounted in a large vacuum vessel on a rotatable platform such, that the sample can face the auxiliary devices: a metal ion source (5-30 keV), a gas ion source (0.1-6 keV) and a quadrupole mass spectrometer. During metal implantation mass separation is provided by means of a magnetic analyser with a mass resolution  $M/\Delta M=200$ . The angle of incidence with respect to the surface normal is about 10 degrees. The helium ion beam is mass-filtered with the aid of an electromagnetic Wien filter. Since high purity He gas is used, the fraction of foreign ions in the He beam is less than  $10^{-4}$ . In both beam lines deflection plates sweep the beam so that uniform implantation is obtained over an area of  $0.1 \text{ cm}^2$ . The crystal is heated by 1.5 keV electron bombardment on the unimplanted side. The temperature is continuously monitored during desorption using a WRe3%-WRe25% thermocouple. The standard heating rate is 40 K/s. The He release rate is measured with the quadrupole mass analyser. The desorption spectra are corrected for the average residence time of He in the desorption volume of 0.1 s.

Dissociation energies of He-defect complexes are obtained by matching computer calculated desorption peaks to the experimental desorption peaks, using the measured temperature profiles. The calculated peaks are based on a first order desorption process:

$$\frac{dc_i(t)}{dt} = c_i(t)v_{0,i}\exp(-E_i^d/kT(t)) \quad (1a)$$

where  $c_i(t)$  is the concentration of defect  $i$  at time  $t$ ,  $E_i^d$  is the dissociation energy of defect  $i$ , and  $T(t)$  the temperature at  $t$ . The pre-exponential factor  $v_{0,i}$  includes the contribution due to the difference between the entropies before and after desorption. The He

release rate  $R_i(t)$  is given by:

$$R_i(t) = f_i \frac{dc_i(t)}{dt} \quad (1b)$$

where  $f_i$  is the number of He atoms dissociating from the specific defect  $i$ . From the peak contents as a function of He dose the number of defects is derived.

### 3.3.2.2. Experimental results.

W(100) was implanted with  $2 \times 10^{12}$  5 keV  $\text{Ag}^+ \text{cm}^{-2}$  at an angle of about 10 degrees with respect to the surface normal. Subsequently, the crystal was heated to a temperature  $T_a$  and injected with  $3 \times 10^{12}$  250 eV  $\text{He}^+ \text{cm}^{-2}$  perpendicularly to the surface. Some spectra with corresponding annealing temperatures  $T_a$  are shown in fig. 1.

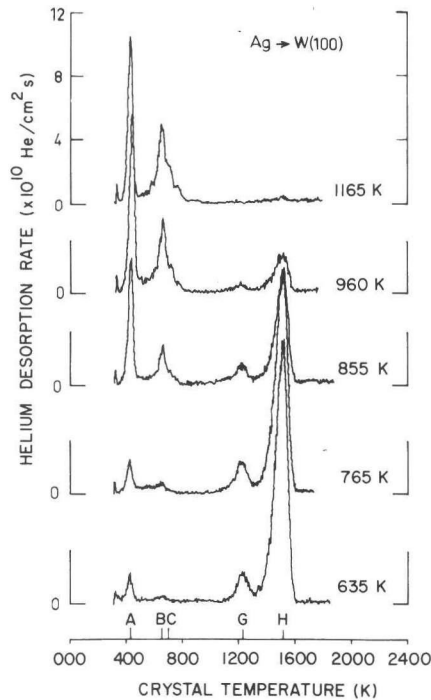


fig. 1: Helium desorption spectra for W(100) implanted with  $2 \times 10^{12}$  5 keV  $\text{Ag}^+ \text{cm}^{-2}$ , annealed to the indicated temperature, and subsequently injected with  $3 \times 10^{12}$  250 eV  $\text{He}^+ \text{cm}^{-2}$ .

Due to the low desorption temperature of 430 K for a heating rate of 40 K/s, the A peak of Ag implanted W was not seen in the earlier

experiments [1]. Heating of the crystal to 340 K by the nearby filament of the ionization source of the mass spectrometer, when the latter was stabilized during 30 minutes prior to the desorption experiment, caused total desorption of the A peak. In the present study care was taken to prevent this by allowing the crystal to cool down a sufficiently long time after each temperature treatment, and keeping the time between He implantation and desorption as short as possible ( $\sim 5$  min).

For the implants Cu, Cr and Mn similar spectra were obtained yielding slightly different binding energies of He to the implant. In the case of In no He binding was observed at temperatures beyond RT. Such a weak binding can be understood taking into account the strong repulsive He-In interaction. In ref. [8] we have discussed the binding energies of He to metallic implants.

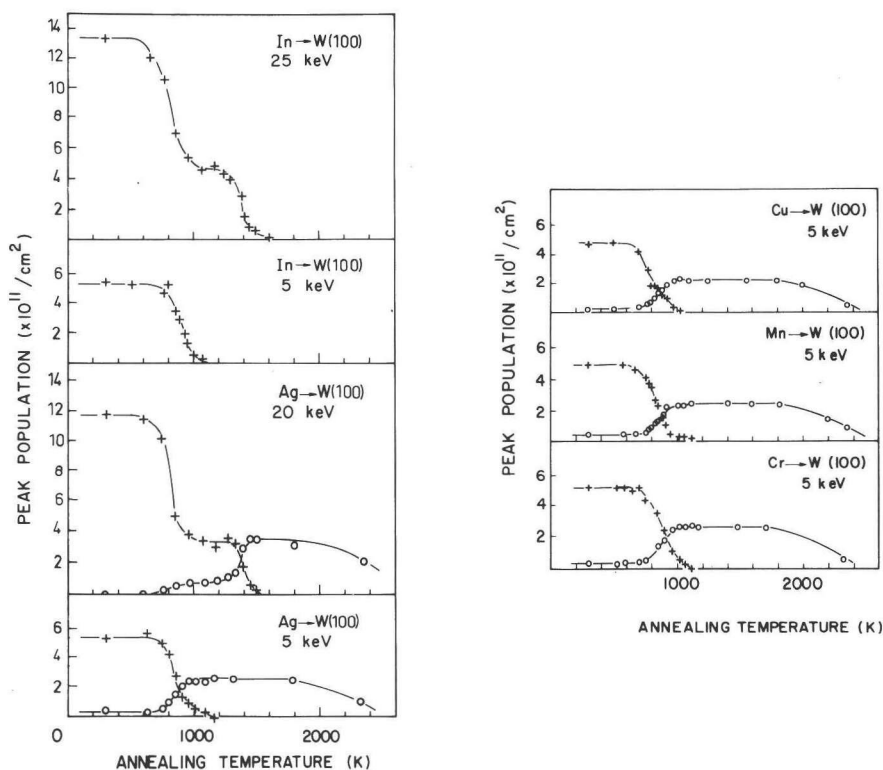


fig. 2: Peak populations as a function of annealing temperature for W(100) implanted with doses of  $2 \times 10^{12}$  cm<sup>-2</sup> of the indicated ions. The He dose and energy was as in fig. 1. (+) sum of G and H peaks, (o) sum of A, B and C peaks.

Peak fitting was applied to the measured spectra with a computer programme. In fig. 2 we have plotted the summed contents of the vacancy-type peaks (G and H) and the impurity-type peaks (A, B and C). For the implants Cu, Mn, In and Cr the spectra were analyzed in the same way (fig. 2b). The following observations were made:

- (i) Between 700 and 900 K the peaks representing vacancy-type traps decrease drastically. Apparently, vacancies become mobile in this temperature region and a large fraction recombines at the surface (stage III recovery). Due to our annealing scheme stage III appears at a higher temperature than normally observed in isochronal annealing experiments [10].
- (ii) The A, B and C peaks become visible at a temperature slightly beyond stage III, the step is more pronounced at the lower implantation energies.
- (iii) In the case of 20-25 keV implantation a vacancy-type defect is stable up to about 1350 K. Its disappearance is accompanied with a further increase of the visible substitutional fraction in the case of implanted Ag.
- (iv) At temperatures above 2000 K all substitutional-type traps disappear.

The H peak observed after heating to 1000 K or higher in the case of 20-25 keV Ag or In bombardment cannot be due to He originally trapped by monovacancies. To investigate the nature of the corresponding defect, a series of experiments was performed with increasing He filling degree of the defects. The W(100) crystal was implanted with 20 keV Ag, heated to 1200 K, cooled down to room temperature, and subsequently injected with increasing doses of 250 eV He, this time at an angle of 10 degrees with respect to the surface normal. The following observations were made (fig. 3):

- (v) The desorption temperature increases with increasing He dose, contrary to the case of multiple filling of monovacancies.
- (vi) For He doses of  $4.2 \times 10^{13} \text{ cm}^{-2}$  or more, desorption occurs at temperatures up to 1800 K, giving rise to I and J peaks.
- (vii) There is a clear separation between the I and J peaks.



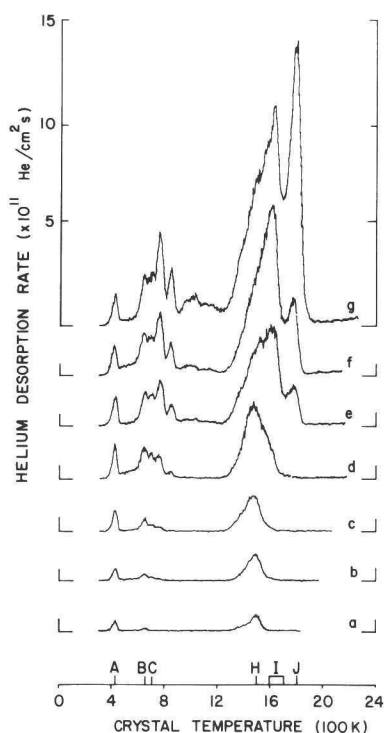


fig. 3: Desorption spectra of W(100) injected with  $2 \times 10^{12}$  20 keV  $\text{Ag}^+$   $\text{cm}^{-2}$ , annealed to 1200 K and injected with 250 eV  $\text{He}^+$ . Doses were a)  $3 \times 10^{12}$   $\text{cm}^{-2}$ ; b)  $6 \times 10^{12}$   $\text{cm}^{-2}$ ; c)  $1 \times 10^{13}$   $\text{cm}^{-2}$ ; d)  $2.2 \times 10^{14}$   $\text{cm}^{-2}$ ; e)  $4.2 \times 10^{13}$   $\text{cm}^{-2}$ ; f)  $6.3 \times 10^{13}$   $\text{cm}^{-2}$ ; g)  $8.8 \times 10^{13}$   $\text{cm}^{-2}$ .

### 3.3.2.3. Defect characterization.

The low-temperature desorption peaks labelled A, B and C were assigned in ref. [8] to detrapping of one, two and three He atoms from substitutional impurity atoms. The G and H peaks seen after 5 keV metal implantation have also been observed by Kornelsen [10] after implantation of 5 keV Kr into W, and have been assigned by him to release of one He atom from  $\text{He}_2\text{V}$  and  $\text{HeV}$ , respectively. The temperatures corresponding with the peak maxima and the assigned defect reactions are given in table 1.

table 1: Peaks visible with THDS, and assigned reactions. The peak temperatures are for a heating rate of 40 K/s.

peak	T (K)	n-He	proposed reaction
A	430	1	$\text{HeAgV} \rightarrow \text{He} + \text{AgV}$
B	645	2	$\text{He}_2\text{AgV} \rightarrow 2\text{He} + \text{AgV}$
C	705	3	$\text{He}_3\text{AgV} \rightarrow 3\text{He} + \text{AgV}$
G	1230	2	$\text{He}_2\text{V} \rightarrow \text{He} + \text{HeV}$
H	1490	1	$\text{HeV} \rightarrow \text{He} + \text{V}$
	~1490	2-3	$\text{He}_n\text{V}_m \rightarrow n\text{He} + m\text{V} \quad m=2,3$
I	~1600	4-7	$\text{He}_n\text{V}_m \rightarrow n\text{He} + m\text{V} \quad m=2,3$
J	1800	>7	$\text{He}_n\text{V}_m \rightarrow n\text{He} + m\text{V} \quad m=4$

The position and shape of the H peak observed after injection with a low He dose coincides with the temperature and peakshape that characterize He desorption from monovacancies. However, after bombardment with 20 keV Ag or In ions an H peak is observed after annealing of the sample at temperatures at which no free vacancies exist (fig. 2). We conclude, therefore, that at least in this case the H peak arises from He that was initially trapped by a defect complex which converts into a He filled monovacancy during desorption. The most obvious defect complex that can reduce to a monovacancy is a vacancy cluster. Other defects that bind He quite strongly, like dislocation loops, can be safely ruled out, since these would certainly give rise to a significantly different desorption temperature [11,12].

The I and J peaks become visible after 20 keV Ag or In implantation, annealing to above stage III, and He injection with doses larger than  $2 \times 10^{13} \text{ cm}^{-2}$ . The original defect is the same vacancy cluster that gave rise to the H peak, except that a larger number of He atoms has been trapped. These extra He atoms stabilize the cluster, which results in a higher desorption temperature as compared with the H peak. Recently it has been shown that monovacancies can be transformed into vacancy clusters by He atoms that push out self-interstitials [13,14,15]. In the next paragraph we will argue that the number of He atoms trapped per defect in our experiments was well below the value required for this so-called trap mutation.

The average He visiting frequency, which is proportional to the local He concentration and the He capture constant, during He injection is at maximum at a layer slightly deeper than the He implantation range [5]. From this layer till a quite large depth the average He

visiting frequency is virtually constant. Consequently, defects located in the latter region will trap more He atoms than defects located closer to the surface. In the experiments of refs. [13,15] the defects were located deeper than the He range, whereas in the present work after 20 keV Ag bombardment the ranges of Ag and He ions are about equal. In addition, the He dose required to grow the I and J peaks in refs. [13,15] was more than five times as large as the dose required in this study. We conclude, therefore, that in the present experiments no trap mutation takes place. This conclusion is corroborated by the observation that I and J peaks do not overlap as is the case in spectra arising from mutated defect complexes [13,15].

An estimate of the size of the above mentioned vacancy cluster is obtained as follows. It is likely that peaks at desorption temperatures higher than the H peak correspond to release of He atoms from traps larger than a monovacancy, and that every new peak corresponds with an extra vacancy. In our case we observed I and J peaks. In order to explain the width of the I peak at higher He doses we must assume that it is composed of two separate peaks. Therefore, beyond the H peak there are three new peaks, although not all of them can be resolved. This indicates that the original defect might be a  $V_4$ .

The different peaks in the desorption spectra were deconvoluted in order to determine the number of He atoms released in each peak. Firstly, the A, B and C peaks were fitted with peak populations calculated from eq. (1). Thus obtained peak populations were used, together with the information that one, two and three He atoms are released in these peaks [8], to match the peak evolutions as a function of He dose with calculated peak evolutions applying the model described in refs. [5,6]. The best fit was obtained with the following parameters: an average He range of 37 Å, a He penetration probability of 0.6, a Ag implantation profile with an average depth of 60 Å (see inset of fig. 4a), and a He trapping constant of 1.15 [16]. This set of parameters is not unique, but it corresponds well with the values expected for implantations at the given energies and angle with respect to the surface normal.

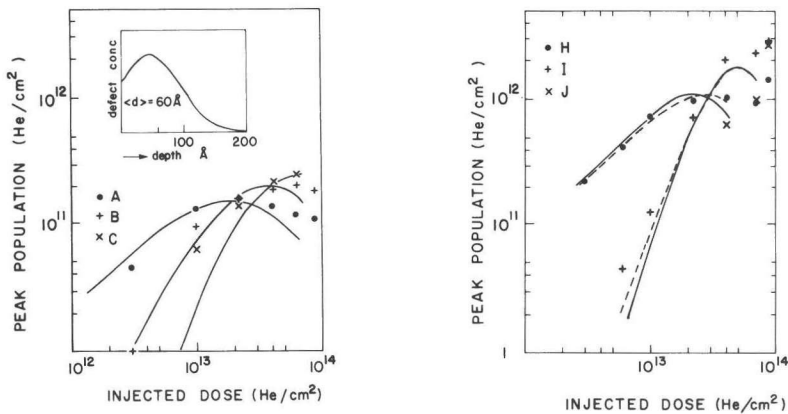


fig. 4: Peak populations as a function of He dose for Ag implanted W(100). Bombardment and annealing parameters as in fig. 3. Drawn curves result from model calculations. The inset shows the assumed Ag implantation profile.

Measured and calculated peak populations as a function of He dose are shown in fig. 4a. The number of AgV derived in this way amounts to  $5 \times 10^{11} \text{ cm}^{-2}$ .

Next, the vacancy-type desorption peaks were fitted using the He visiting frequency obtained from the previous analysis. All He desorbing at temperatures slightly below the H peak was added to the H peak population, and all He desorbing in the temperature range between H and J peak was lumped into the I peak. The J peak is clearly defined and was matched with a peak calculated from eq. (1), resulting in a pre-exponential factor of  $10^{18} \text{ s}^{-1}$ . Van Veen et al. [13] have shown that such a large pre-exponential factor arises when several He atoms are released subsequently with similar activation energies. We used the same set of parameters as before except for the He capture constant which was increased to the value 1.87 appropriate for the vacancy cluster  $V_4$  [16]. The best fit to the data is obtained when it is assumed that up to three He atoms are released in the temperature region at and just below the H peak. If filled with one He atom, the cluster reduces to HeV by detrapping of excess vacancies during desorption at a temperature between 1400 K and 1490 K. If filled with two or three He atoms, several dissociation mechanisms are possible. It is further obtained that all He released in the I peak after detrapping of one or two vacancies if the cluster contains four to seven He atoms, and that all He is released in the J peak if the clus-

ter contains more than seven He atoms (drawn curves in fig. 4b).

The decrease of the vacancy-type peaks (H, I, J) at an annealing temperature of 1400 K is nearly counterbalanced by the growth of the interstitial-type peaks (A, B, C), indicating that there is about one vacancy cluster per implanted impurity atom and that most of these clusters are located within a few lattice constants from the implant. Indeed the number of vacancy clusters derived from the model, together with the number of AgV, turns out to be  $1.8 \times 10^{12} \text{ cm}^{-2}$  which compares well with the implantation dose of  $2 \times 10^{12} \text{ cm}^{-2}$ .

We have also fitted the data assuming the same He capture constant 1.15 for the vacancy cluster used for AgV (dashed curves in fig. 4b). In this case the best fit is obtained when it is assumed that all He released in H, I and J peak if the vacancy cluster contains one or two, three or four, or more than four He atoms, respectively. However, the number of vacancy clusters from this analysis,  $3.4 \times 10^{12} \text{ cm}^{-2}$ , is much larger than the number of implanted impurity atoms.

### 3.3.3. PAC EXPERIMENTS.

#### 3.3.3.1. Method.

Lattice defects in cubic metals generally lower the local symmetry. The resulting electric field gradient (EFG) will interact with the nuclear electric quadrupole moment of a suitable probe atom introduced in the sample. This hyperfine interaction causes a time dependent perturbation of the angular distribution of  $\gamma$ -rays emitted by the probe atom. Each defect gives rise to a unique set of well-defined modulation frequencies which can be measured with high resolution, thus enabling discrimination between different kinds of lattice defects even in the case they occur simultaneously. It is this feature that renders PAC a powerful method in defect studies.

In the following we will briefly describe the essential aspects of PAC. For a more complete treatment we refer to the review by Frauenfelder and Steffen [17].

In a PAC experiment one measures the coincidence count rate of two  $\gamma$ -rays emitted in a cascade by the same nucleus:

$$C(\Omega_1 \Omega_2; t) = C_0 \exp(-t/\tau_n) W(\Omega_1 \Omega_2; t) \quad (2)$$

where  $C_0$  is the product of source strength and detector efficiencies,  $\tau_n$  is the lifetime of the intermediate nuclear state,  $\Omega_1$  and  $\Omega_2$  denote the angles of  $\gamma$ -ray emission, and  $W(\Omega_1, \Omega_2; t)$  describes the time dependent directional distribution of the  $\gamma$ -rays. In the case of polycrystalline samples the directional distribution takes the form (higher order terms are omitted for simplicity):

$$W(\Omega_1, \Omega_2; t) = 1 + A_2 P_2(\cos\theta) G_2(t) \quad (3a)$$

$$G_2(t) = \sum_i f_i G_{2,i}(t) \quad (3b)$$

$$G_{2,i}(t) = \sum_j a_{ij} \cos(b_{ij} \nu_{oi} t) \quad (3c)$$

where  $A_2$  is the anisotropy coefficient,  $P_2(\cos\theta)$  is the second order Legendre polynomial depending on the angle  $\theta$  between the directions denoted by  $\Omega_1$  and  $\Omega_2$ ,  $f_i$  is the relative number of probe atoms associated with the defect  $i$ , and  $G_{2,i}(t)$  is the corresponding perturbation factor that contains all relevant information about the hyperfine interaction. The quadrupole interaction frequency,  $\nu_o$ , is given by the expression:

$$\nu_o = \frac{eQV_{zz}}{h} \quad (4)$$

where  $Q$  is the nuclear quadrupole moment and  $V_{zz}$  is the  $z$ -component of the diagonalized EFG tensor. The relative modulation amplitudes and frequency factors,  $a_{ij}$  and  $b_{ij}$ , in eq. (3) depend on the spin of the intermediate nuclear state and on the value of the asymmetry parameter  $\eta$  of the EFG tensor:

$$\eta = \frac{V_{xx} - V_{yy}}{V_{zz}} \quad (5)$$

In the case of single-crystal samples,  $a_{ij}$  also depends in a complicated but well known manner on the orientations  $\Omega_1$  and  $\Omega_2$  of the  $\gamma$ -ray detectors with respect to the crystallographic axes.

Our samples were prepared by implantation of  $^{111}\text{Ag}$  or  $^{111}\text{In}$  ions. Both nuclei decay via an intermediate nuclear state in  $^{111}\text{Cd}$  with spin  $I=5/2$ , lifetime  $\tau_n=122$  ns and quadrupole moment  $Q=0.8$  b (see decay scheme in fig. 5).

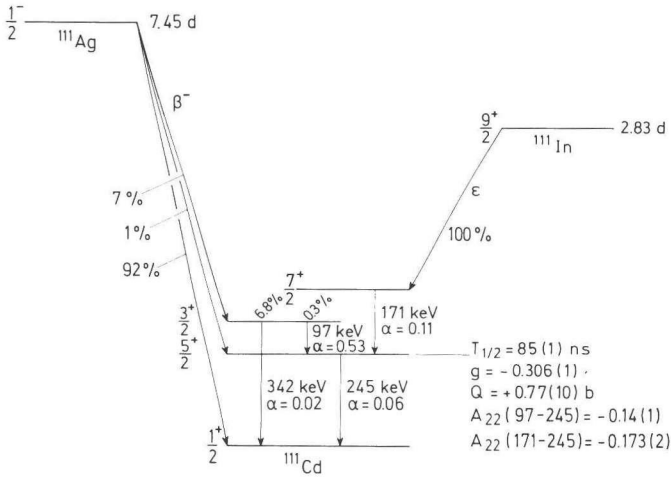


fig. 5: Partial decay scheme of  $^{111}\text{Ag}$  and  $^{111}\text{In}$  (from ref.[18]).

In this particular case each defect gives rise to three non-zero modulation frequencies:  $b_{i0}=0$ ,  $b_{i1}+b_{i2}=b_{i3}$  (cf. eq. (3)). The maximum modulation amplitude is about 13%. However,  $^{111}\text{Ag}$  decays via the appropriate  $\gamma$ - $\gamma$  cascade in only 0.15% of the desintegrations, which makes that statistics are usually much worse than in the case of the probe atom  $^{111}\text{In}$ .

The PAC measurements were carried out using a standard slow-fast coincidence system with a time resolution of about 2.5 ns FWHM. Details of the experimental set-up and the applied data-reduction methods can be found in ref. [19].

### 3.3.3.2. Experimental results.

Almost perfectly (100) oriented polycrystalline W foils were implanted at RT with 25 keV  $^{111}\text{Ag}$  or  $^{111}\text{In}$  ions at a dose of  $2 \times 10^{13} \text{ cm}^{-2}$ . The samples were annealed for 15 min in vacuum at specific temperatures, and studied by PAC after each annealing step. The annealing temperatures increased step-wise to about 1400 K. Some typical spectra are collected in fig. 6. The solid lines represent the function  $1-W(\Omega_1\Omega_2;t)$ , defined by eq. (3).

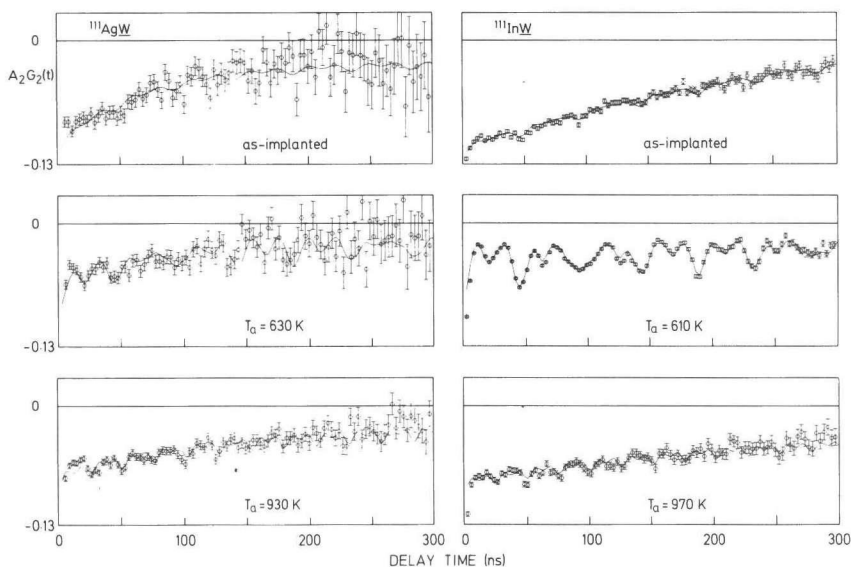


fig. 6: Perturbation factors for  $^{111}\text{Ag}$  and  $^{111}\text{In}$  implanted in W at RT with an energy of 25 keV after annealing at different temperatures  $T_a$ .

Best values of the parameters  $f_i$ ,  $\nu_{oi}$ ,  $\eta_i$ ,  $a_{ij}$  and  $b_{ij}$  were obtained from a least-squares fitting procedure.

Apart from substitutional impurity atoms, i.e. atoms on lattice positions with no defect within a distance of approximately one lattice unit, three different sets of hyperfine interaction parameters can clearly be distinguished. Consequently there are three different well-defined impurity-defect complexes that give sizable contributions to the perturbation factor.

table 2: Hyperfine parameters observed with PAC and assigned defects.

defect	$\nu_{oi}$ (MHz)	$\eta_i$	symmetry	proposed defect
1	141	0.0	$\langle 111 \rangle$	$\text{XV}_2$
2	181	1.0	$\langle 110 \rangle$	$\text{XV}_3$
3	260	0.0	$\langle 100 \rangle$	



In table 2 the hyperfine parameters are given. Note that the quadrupole frequencies do not depend on the impurity atom because both  $^{111}\text{Ag}$  and  $^{111}\text{In}$  decay to the same nuclear level in  $^{111}\text{Cd}$ .

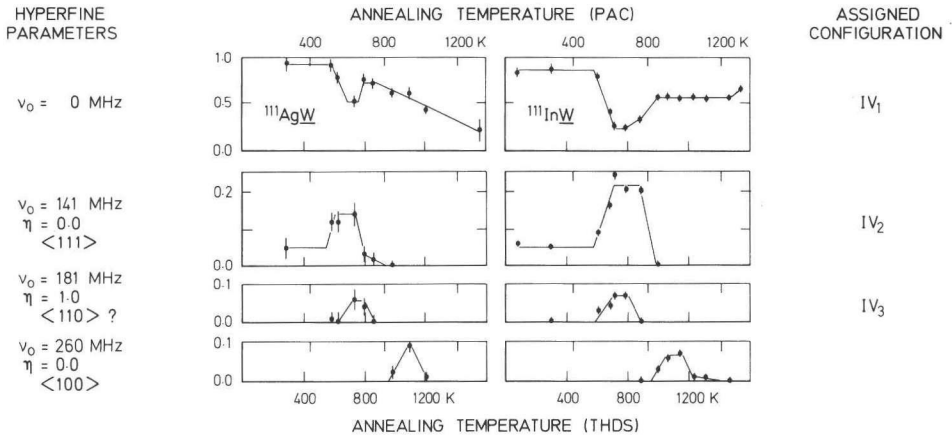


fig. 7: Annealing behaviour of defects in W, observed in PAC measurements on samples implanted with  $^{111}\text{Ag}$  and  $^{111}\text{In}$  at 25 keV. Corresponding hyperfine parameters are indicated at the left-hand side. Assigned impurity-vacancy clusters are given at the right-hand side.

In fig. 7 the fractions  $f_i$  of impurity atoms associated with the different defect configurations are plotted as a function of the annealing temperature. We did not observe a significant change in the annealing behaviour when the implantation energy was raised from 25 to 110 keV. For  $^{111}\text{In}$  in W our results agree with those obtained by Pütz et al. [20].

To facilitate the comparison between PAC and THDS results we give at the bottom of fig. 7 a temperature scale that is renormalized according to the annealing conditions of the THDS experiment. It was assumed that both defect trapping and detrapping are determined by a single-step process governed by a single activation energy, so that eq. (1) may be applied. Since in the THDS annealing scheme the temperature rises linearly with time to a maximum annealing temperature  $T_a$  and then drops with a cooling rate depending on the maximum temperature, eq. (1) had to be solved numerically. For various values of  $T_a$  we determined the dissociation energy  $E^d$  for which  $c_i(\infty)=c_i(0)/2$ , assuming a pre-exponential factor  $\nu_0=10^{13} \text{ s}^{-1}$ . The corresponding temperature in the PAC annealing scheme was defined as the temperature at which, for the same value of  $E^d$ , the initial defect concentration is

also reduced by a factor 2 after the annealing time of 15 min. In this case eq. (1) can be solved numerically. The reader should be reminded however, that the above model is an oversimplification, and that a comparison of THDS and PAC annealing temperatures should be made with due reserve.

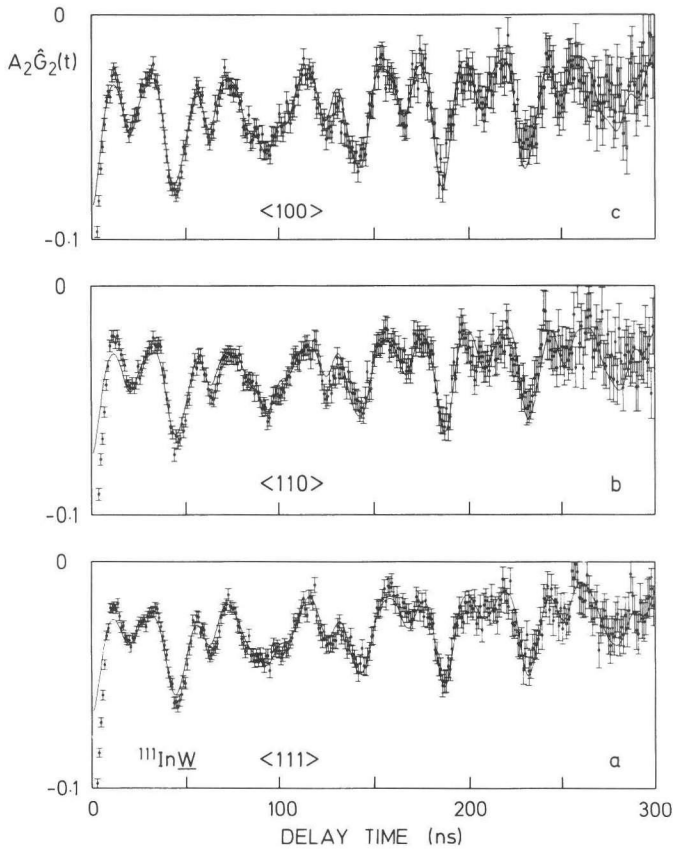


fig. 8: Perturbation factors for  $^{111}\text{In}$  implanted in W after annealing at about 700 K (THDS scale), with detectors oriented along (a)  $\langle 111 \rangle$ , (b)  $\langle 110 \rangle$  and (c)  $\langle 100 \rangle$  crystallographic directions.

In order to determine the symmetry of the observed impurity-defect complexes some spectra were taken with very high statistical accuracy. In those experiments the  $\gamma$ -ray detectors were oriented along the  $\langle 100 \rangle$ ,  $\langle 110 \rangle$  or  $\langle 111 \rangle$  crystallographic directions of the grains in the W foil. The symmetry of the defect was deduced from the dependency of the relative modulation amplitudes,  $a_{ij}$ , on the detector geometry.

From fig. 7 it is clear that after implantation and annealing defect 1 ( $\nu_{01}=141$  MHz) and defect 2 ( $\nu_{02}=181$  MHz) appear at the same annealing temperature, 700 K according to the THDS scale. Therefore the different modulation frequencies may interfere in the analysis. Fortunately, the contributions of defect 1 to the perturbation for the above mentioned detector geometries differed considerably, proving unambiguously that defect 1 possesses a 3-fold symmetry axis along the  $\langle 111 \rangle$  crystallographic direction. We used this fact, already reported by Pütz et al. [20], in the further analysis of the series of spectra shown in fig. 8.

We first analyzed the sum of the three spectra since from calculations it follows that the different modulation amplitudes in the sum-spectrum are close to the values appropriate to randomly oriented polycrystalline material. In this way the defect fractions  $f_1=0.20\pm 0.01$  and  $f_2=0.10\pm 0.01$  were found. Subsequently each spectrum of fig. 8 was fitted separately while the frequencies were the same as in the previous analysis, and the relative amplitudes of the modulation arising from defect 1 were fixed at the theoretical values for a  $\langle 111 \rangle$  orientation. The diagrams in fig. 9 show the resulting modulation amplitudes due to defect 2, which were treated as free parameters, together with theoretical predictions for a number of defect configurations with symmetry axes along low-index crystallographic directions.

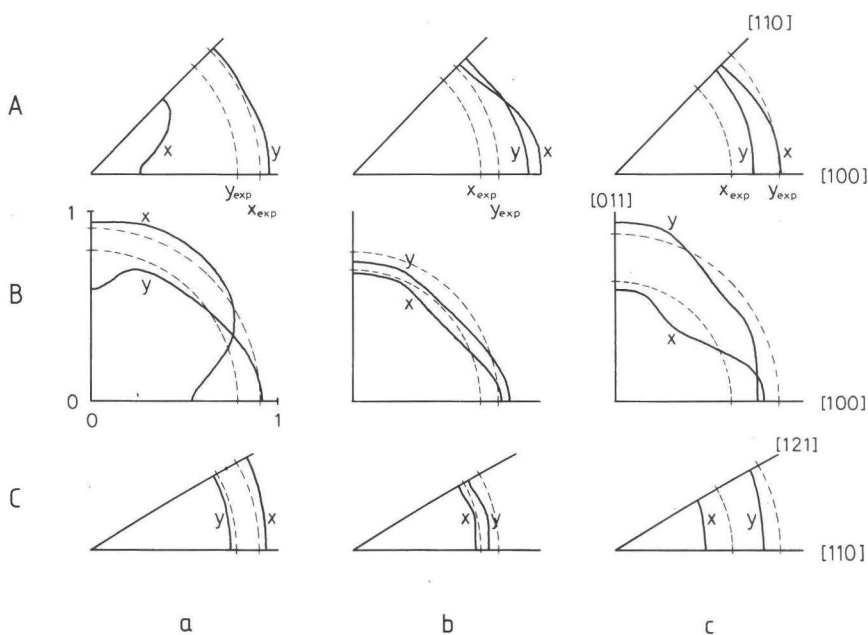


fig. 9: Dependency of the quantities  $x = a_1 + a_2 + a_3$  and  $y = (a_1 + a_2)/x$  on the orientation of the principal y-axis of the EFG tensor corresponding with defect 2, for different orientations of the principal z-axis and different detector geometries. The modulation amplitudes  $a_j$  are defined by eq. (3), (A)  $z//[001]$ , (B)  $z//[01\bar{1}]$ , (C)  $z//[1\bar{1}1]$  (a)  $\gamma//\langle 100 \rangle$ , (b)  $\gamma//\langle 110 \rangle$ , (c)  $\gamma//\langle 111 \rangle$

From this we conclude that the structure of defect 2 is such that the principal z-axis (or, equivalently, the principal y-axis) of the corresponding EFG tensor does not point into a  $\langle 100 \rangle$  direction.

The set of spectra shown in fig. 10 was taken to investigate the symmetry properties of defect 3 ( $\nu_{03}=260$  MHz). The dependency of the modulation amplitudes on the orientations of the detectors showed unambiguously that defect 3 possesses a 4-fold symmetry axis along the  $\langle 100 \rangle$  direction.

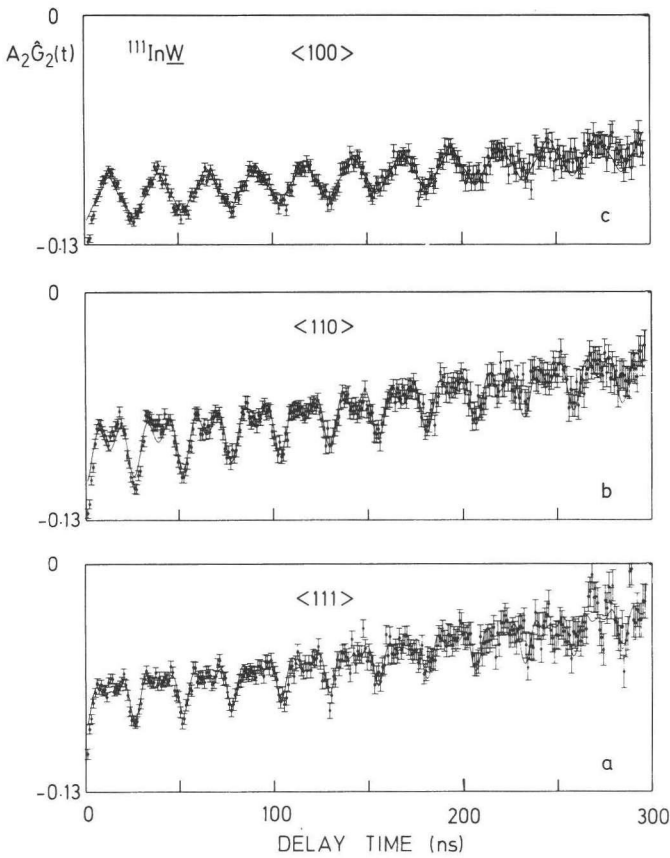


fig. 10: Perturbation factors for  $^{111}\text{In}$  implanted in W after annealing at about 1200 K (THDS scale) with detectors oriented along (a)  $\langle 111 \rangle$ , (b)  $\langle 110 \rangle$  and (c)  $\langle 100 \rangle$  crystallographic directions.

### 3.3.3.3. Defect characterization.

Defects 1 and 2 are formed in a rather narrow temperature region around 650 K (THDS scale), see fig. 7. This temperature coincides with stage III temperature found in resistivity measurements and is associated with vacancy mobility [10], see also section 2.2. Therefore it is likely that defects 1 and 2 are formed by trapping of one or more vacancies at the implants. Additional evidence for the vacancy character of these defects has been given by Pütz et al. [20]. They

observed that both defects can be converted into substitutional In atoms by the introduction of mobile selfinterstitials by bombarding the sample at room temperature with 60 keV protons to a dose of  $1 \times 10^{15} \text{ cm}^{-2}$ .

Defect 1 has been associated by Pütz et al. [20] with the configuration  $\text{InV}_2$ , a substitutional In atom with a vacancy at nearest neighbour distance (fig. 11a).

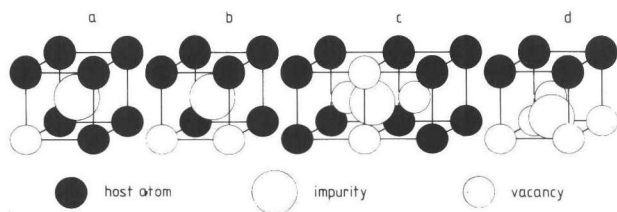


fig. 11: Some impurity-vacancy configurations: (a)  $\text{IV}_2$ , (b)  $\text{IV}_3$ , (c)  $\text{IV}_4$ , (d)  $\text{IV}_5$ .

They based their conclusion on the following observations: (i) defect 1 is formed with the largest fraction next to the substitutional fraction, (ii) the EFG tensor is axially symmetrical, and (iii) the proposed configuration possesses the observed  $\langle 111 \rangle$  symmetry axis.

Defect 2 has been associated with an  $\text{InV}_3$ , a substitutional In atom with two nearest neighbour vacancies. Of the three possible configurations, the one in which vacancies and impurity atom are collinear can be ruled out because this will lead to a zero asymmetry parameter. The other two configurations produce the same EFG and can therefore not be distinguished by PAC. The one that is supposed to have the lowest formation energy is shown in fig. 11b. For this configuration the point charge model predicts an EFG tensor with principal axes  $z//[01\bar{1}]$  and  $y//[011]$ , which is consistent with the results of our crystal orientation experiments (fig. 9).

The decrease of the substitutional fraction at 650 K is considerably larger than the simultaneous increase of the defect fractions  $f_1$  and  $f_2$  (fig. 7). Apparently, there is an invisible fraction that includes a variety of defect configurations, thus giving rise to a large number of quadrupole frequencies. This results in a strongly damped modulation pattern in the time domain. In the case of  $^{111}\text{Ag}$

implantation, the invisible fraction increased up to 70% at 1400 K, whereas in the case of  $^{111}\text{In}$  implantation the invisible fraction remained constant at a value of 40%. It was observed, however, that radioactivity was lost from the sample during annealing of the Ag implanted sample at temperatures above 950 K (THDS scale). At 1400 K the loss was even 40 %. Therefore the increase of the apparent hidden fraction with increasing annealing temperature may be due to mobility of Ag. After correction for this hypothetical out-diffusion the hidden fraction is constant and amounts to about 30%.

The decrease of the defect fractions  $f_1$  and  $f_2$  at about 800 K is counterbalanced by an increase of the substitutional fraction by an equal amount (fig. 7). It indicates that the disappearance of defects 1 and 2 is due to release of trapped vacancies.

Defect 3 has tentatively been attributed by Pütz et al. [20] to impurity atoms that have trapped three or more vacancies. For the configuration  $\text{XV}_4$  (fig. 11c) the point charge model predicts an EFG tensor with principal z-axis  $\parallel [100]$ , in agreement with the symmetry derived in this study. The same configuration has been assigned by Weidinger et al [21] to a defect that is formed in Mo implanted with  $^{111}\text{In}$ . However, there are two important differences: (i) the defect in Mo causes a quadrupole frequency which is smaller than the one that is due to a monovacancy, whereas in W the frequency is much larger, and (ii) in Mo the defect is formed in early stage III whereas in W it is formed far beyond stage III. Another possible small vacancy cluster that possesses the correct symmetry is the configuration  $\text{XV}_5$  (fig. 11d). In order to obtain the right magnitude of the quadrupole frequency it has to be assumed that the impurity atom is shifted over about 0.3 lattice units along the  $[001]$  direction.

Unfortunately, it is impossible to give formation pathways for the above small clusters  $\text{XV}_4$  and  $\text{XV}_5$  without running into conflicts. The chief cause of conflict is that there is no abrupt change of the substitutional fraction which is correlated with growth and disappearance of defect 3. Additional trapping of vacancies by defects 1 and 2 can also be excluded since these defect complexes break up already at about 800 K, as argued before. A hypothesis not in contradiction with the experimental results is that part of the invisible fraction is due to different configurations of vacancy clusters that collapse into vacancy loops at a well defined temperature (1000 K, THDS scheme). Apparently, these planar defects give rise to a unique hyperfine

interaction, which makes them visible in the PAC experiment. At still higher temperature another transformation of the structure takes place, and the resulting defects again merge in the invisible fraction.

Final recovery of lattice damage does not occur below 1400 K (THDS scale) which is consistent with the THDS results (figs. 2a and 7).

### 3.3.4. MODEL CALCULATIONS.

#### 3.3.4.1. Implantation simulations with Marlowe.

Simulations of the collision cascade during implantation were performed using the binary collision code Marlowe [22]. The number of implantations per ion type was limited to 50. The individual cascades were analysed with respect to the radial vacancy distributions around the implanted atoms. The fraction of formed Frenkel Pairs that recombine spontaneously depends on the average Frenkel Pair separation. To simulate this, an effective cut-off radius  $r_c$  was introduced in Marlowe such that every vacancy-interstitial pair with a separation less than  $r_c$  recombines. Hou et al. [23] measured vacancy concentrations in He bombarded Mo applying THDS. In the analysis they varied the minimum displacement energy  $E^d$  and the cut-off radius  $r_c$  until they obtained the best agreement between calculated and measured vacancy concentrations. The optimum parameters turned out to be  $E^d=33$  eV and  $r_c=3.7a_0$  ( $a_0$  is the lattice constant). In our calculations for W we took the same value of the cut-off radius as for Mo, but a displacement energy of 40 eV [24]. In fig. 12 we show the results obtained for different energies, implants and implantation angles. Note that the number of vacancies in the immediate surrounding of the implant is virtually the same for all implantation energies considered.



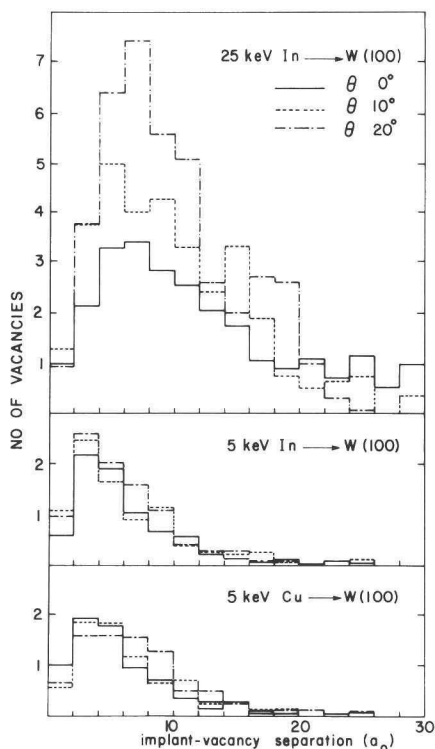


fig. 12: Radial vacancy distributions for In and Cu implanted into W(100) at various implantation energies and angles with respect to the surface normal.

### 3.3.4.2. Annealing results.

To estimate the number of nearby vacancies migrating towards the implant during early stage III, random walk theory was applied. The vacancy started its random walk 2000 times at each non-equivalent lattice point within  $2.5a_0$  from the defect. The jump direction was determined by a random number generator, a vacancy jump probability of  $1/8$  was assumed for each  $\langle 111 \rangle$  direction. Once the vacancy had arrived at a first or second neighbour lattice position with respect to the defect, trapping was assumed. The vacancy was supposed to be lost for short range capture once outside a sphere with radius  $8a_0$  around the impurity. Taking this radius to be  $10a_0$  changed the trapping probabilities only slightly. Thus obtained radial vacancy trapping probabilities were applied to the individual cascades calculated with Marlowe (previous section).

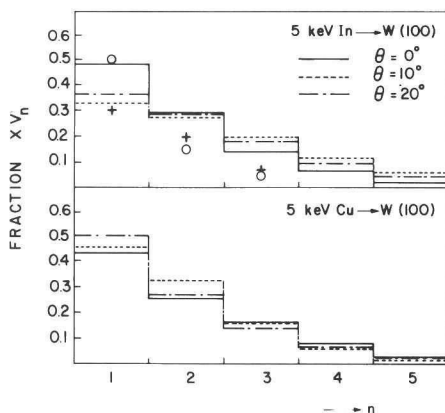


fig. 13: The fraction  $\times V_n$  after annealing up to stage III for In and Cu implanted into W(100) at 5 keV. For comparison, also the PAC results for 25 keV In (+) and Ag (o) are plotted.

The fractions found of  $\times V_n$  with  $n=1,2,3,4$  are shown in fig. 13 for the indicated implantation parameters. For comparison we have also plotted the fractions for  $\text{Ag}V_n$  and  $\text{In}V_n$ , with  $n=1,2,3$ , obtained from the PAC measurements. They agree fairly well with the calculated values. It should be realized that especially for oversized impurities, like heavy noble-gas atoms, vacancy jumps towards the implant will be enhanced at small separations. This problem is dealt with in more detail in [25]. We performed the random walk calculations only for the 5 keV implantation, because after 20 keV implantation vacancy clusters are present near the implant. This leads to a reduced probability for trapping of vacancies at the impurity atom, which is not taken into account by the present model.

The number of vacancy jumps till trapping occurred was counted for the various starting positions. We found that 56% of the vacancies starting from less than  $2a_0$  were trapped after about 5 jumps, and that 18% of the vacancies starting from  $2a_0$  to  $4a_0$  were trapped after about 21 jumps. These values are larger than those earlier reported [4], since the radius determining short range vacancy loss was taken  $8a_0$  instead of  $4a_0$ .

In order to estimate the fraction of substitutional implants visible in the THDS experiments we performed the following calculations. First we determined the radial probability distribution of finding a vacancy at a distance  $r$  from the implant after  $n$  jumps by

following the fate of 500 vacancies starting from the impurity position. In [16] the shielding of the implant against He trapping as well as the retrapping of He released from the implant by a nearby vacancy were calculated as a function of implant-vacancy separation, yielding the THDS detection efficiency for implants near vacancies for low He doses. Combination of this separation dependent efficiency and the radial vacancy probability distributions mentioned before gave the fraction of substitutional implants that is detected by THDS after  $n$  jumps of the released vacancy (fig. 14).

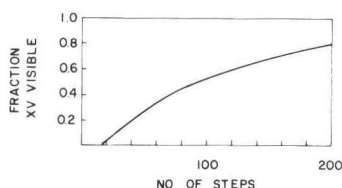


fig. 14: The fraction of XV detectable with THDS for low He doses, after dissociation of  $XV_2$ , as a function of the number of steps of the released vacancy.

We conclude that after 200 steps about 80% of the implants are visible in THDS. Using the information contained in fig. 14 and the measured temperature profiles we calculated the visible fraction of substitutional implants after annealing to a temperature  $T_a$ .

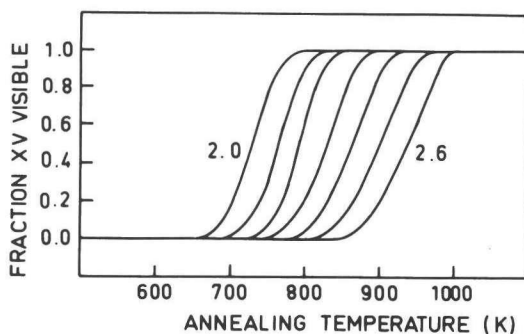


fig. 15: The fraction of XV detectable with THDS, starting with  $XV_2$ , as a function of annealing temperature for dissociation energies ranging from 2.0 to 2.6 eV with increment 0.1 eV.

In fig. 15 we show the visible fraction as a function of the annealing temperature for various values of the dissociation energy  $E^d$  of the original  $XV_2$  defect, assuming a vacancy migration energy of 1.70 eV and a pre-exponential factor  $\nu_0 = 4.4 \times 10^{13} \text{ s}^{-1}$ .

### 3.3.5. INTERPRETATION OF THE RESULTS.

#### 3.3.5.1. Discrepancy between THDS and PAC results from as-implanted samples.

The most striking difference between the results obtained by the two applied methods is that PAC showed a large substitutional fraction in as-implanted samples, whereas virtually no substitutional atoms were seen with THDS. Mössbauer experiments on W and Mo implanted with 50-100 keV radioactive Xe atoms also revealed a substitutional fraction of about 60% in as-implanted samples [26,27]. Apparently THDS is not suitable for detection of substitutional impurities in as-implanted samples for higher implantation energies. We believe that this finding strongly supports the conclusion, drawn in ref. [16], that nearby vacancies reduce the visibility of substitutional implants in THDS. Vacancies near substitutional implants shield the implant for He capture, retrap desorbed He, and cause drainage of He to the nearby vacancies at lower temperatures than needed for bulk dissociation. Especially the latter effect is quite strong since He is able to push a neighbouring lattice atom in a more distant vacancy, thereby self being trapped by the newly formed vacancy, as shown in [16,28].

#### 3.3.5.2. Vacancy migration energy.

The monovacancy migration energy  $E_V^m$  can be calculated from the annealing temperature  $T_a = 550 \pm 10 \text{ K}$  (PAC scale) at which vacancy trapping was observed by PAC, the time  $\Delta t = 15 \text{ min.}$  during which the sample was annealed, the number of jumps  $n = 5-21$ , required for trapping, as derived in section 4.2, and the jumping frequency  $\nu_0 = 4.4 \times 10^{13}$ . The latter was derived from the diffusivity of

tungsten in the temperature range 1700-3400 K, reported by Mundy et al. [29]:

$$D = 0.04 \exp[-5.4 \pm 0.5 \text{ eV}/kT] + 46 \exp[-6.9 \pm 0.6 \text{ eV}/kT] \text{ cm}^2/\text{s} \quad (6)$$

The first of the two exponential terms is the monovacancy contribution which can also be written as:

$$D = \nu_0 \frac{\lambda^2}{6} f \exp[(S_V^f T - E_V^m - E_V^f)/kT] \quad (7)$$

where  $\nu_0$  is the jumping frequency,  $\lambda$  is the average jumping distance, the factor  $f$  accounts for the correlation between consecutive jumps of the tracer atom,  $S_V^f$ ,  $E_V^m$  and  $E_V^f$  are the monovacancy formation entropy, migration enthalpy and formation enthalpy. Substitution of  $f=0.727$  (ref. [30]) and  $S_V^f=2.3/k$  (ref. [9]) in eqs. (6) and (7) gives  $\nu_0=4.4 \times 10^{13} \text{ s}^{-1}$ . The monovacancy migration enthalpy turns out to be  $E_V^m = kT_a \ln(\nu_0 \Delta t/n) = 1.70 \pm 0.07 \text{ eV}$ . The error reflects the uncertainty in the temperature at which vacancy trapping was observed and the uncertainty in the number of jumps required for short-range trapping. Our value of  $E_V^m$  compares well with the value  $1.78 \pm 0.10 \text{ eV}$  derived by Rasch et al. [9]. The small difference may be due to an overestimate of the number of jumps necessary for the vacancy to reach the PAC probe atom or to strain enhanced vacancy migration caused by the mismatch of probe and host atomic volumes [31].

In the THDS experiments (Fig. 2) vacancy mobility became visible at a temperature that is appreciably higher than in the corresponding PAC experiment (fig. 7), even if we use the renormalized temperature scale. This is due to the fact that vacancies have to migrate to the surface, to disappear in the THDS spectra. This requires many more steps than the 5-21 needed for short range trapping observed in PAC.

### 3.3.5.3. Vacancy binding energies.

Defect dissociation energies were derived from the annealing temperatures at which defects 1 ( $XV_2$ ) and 2 ( $XV_3$ ) disappear in the PAC spectra (fig. 7).

table 3: Vacancy dissociation and binding energies  
obtained from PAC and THDS.

method	defect	$E^d$ (eV)	$E^b$ (eV)
PAC	AgV <sub>2</sub>	2.2	0.5
	AgV <sub>3</sub>	2.3	0.6
	InV <sub>2</sub>	2.7	1.0
	InV <sub>3</sub>	2.4	0.7
THDS	AgV <sub>2</sub>	<2.5	<0.8
	CuV <sub>2</sub>	<2.5	<0.8
	CrV <sub>2</sub>	<2.5	<0.8
	MnV <sub>2</sub>	<2.4	<0.7

The results given in table 3 were calculated for a jumping frequency of  $4.4 \times 10^{13} \text{ s}^{-1}$ . The dissociation energies are considered to have a relative accuracy of 0.05 eV. The binding energies also shown in table 3 are equal to the corresponding dissociation energies minus the vacancy migration energy  $E_V^m = 1.70 \text{ eV}$ .

Defect dissociation energies could not be calculated in the same direct way from the THDS spectra since the absence of A, B and C peaks in the spectra does not necessarily mean that  $XV_n$  defects have formed, as argued in section 5.1. On the other hand, visibility of the A, B and C peaks is a clear indication for the presence of substitutional implants. Therefore upper limits for the vacancy dissociation energy follow from the annealing temperature at which the A, B and C peaks become visible provided that the implants had the opportunity to trap a vacancy. The calculations presented in section 4.2 show that after 5 keV implantation and annealing to stage III about 50% of the implants had the opportunity to trap a vacancy. This is corroborated by our PAC experiments on 25 keV Ag and In in W and by THDS experiments on 5 keV Kr in W [8] and 2 keV Ar in Mo [32], which showed that 50% to 80% of the implants were associated with one or more vacancies. By comparing the fraction of  $XV$  visible after annealing to  $T_a$  (see fig. 15) with the measured population of the A, B and C peaks (see fig. 2) we found the upper limits for the dissociation energies as presented in table 3.

It should be mentioned that the dissociation and binding energies were calculated using the jumping frequency for free vacancy migration. Recently, Koike et al. [33] have demonstrated, that binding of vacancies to various impurity atoms in Al also involves a substantial

binding entropy. The latter leads to an effective lowering of the pre-exponential factor  $\nu_0$  by one or two orders of magnitude, depending on the impurity.

#### 3.3.5.4. Larger defect clusters.

The breaking up of the vacancy cluster, probably a  $V_4$ , observed after annealing beyond stage III temperature was observed as a discrete step at about 1350 K. A binding energy of 1.9 eV was calculated, taking the jump frequency and migration energy of the monovacancy. Masuda [34] calculated the stability of small vacancy clusters in W, applying a tight-binding type of electronic theory. Binding energies he found were 0.54 eV and 1.36 eV for respectively the most stable tri- and tetra-vacancies. Since we neglected binding entropies in the derivation of our binding energy our value will be too high. So we may conclude that the calculations predict the right order of magnitude.

From the peak evolution as a function of the He dose, it was concluded that only about 8 He atoms are needed to stabilize the  $V_4$  defect at a temperature up to 1800 K.

According to PAC, a defect with well defined structure appears at 850 K and disappears at 1050 K (PAC scale). The fraction, however, is much lower than the high temperature defect seen with THDS.

#### 3.3.6. CONCLUSIONS.

- Metallic impurities implanted into W with an energy ranging from 5 to 100 keV occupy substitutional positions with one or more nearby vacancies.

- Those nearby vacancies make it impossible for THDS to detect the substitutional implants, due to shielding during the He injection and to retrapping during He desorption.

- At early stage III vacancies become mobile. About half the amount of implants traps one or more vacancies, giving rise to at least two well defined defects;  $XV_2$  and  $XV_3$ . The vacancy migration energy derived is  $E_V^m = 1.70 \pm 0.07$  eV.

- At a temperature slightly beyond stage III the vacancy-impurity complexes dissociate. This step is clearly seen with PAC. However, all vacancies must have migrated till outside a sphere with a radius of  $2.5a_0$  surrounding the implant before the substitutional implants are

visible in THDS. From PAC results binding energies of impurity-vacancy complexes were obtained which range from 0.5 to 1.0 eV depending on the implant. THDS provides only upper limits for the binding energy, since by this technique nearby vacancies or vacancy clusters cannot be distinguished from bound vacancies.

- In THDS a defect is observed which persists up to 1400 K. It probably consists of four vacancies with a dissociation energy of 3.6 eV.
- After annealing to 1200 K (THDS scale) PAC measurements reveal the existence of a well-defined defect which we can not uniquely ascribe to a specific configuration.

This work was partly financed by the Stichting voor Fundamenteel Onderzoek der Materie (Foundation for Fundamental Research on Matter) subsidized through the Nederlandse Organisatie voor Zuiver Wetenschappelijk Onderzoek (Netherlands Organization for the Advancement of Pure Research).

## REFERENCES

- [1] G.J. van der Kolk, A. van Veen, L.M. Caspers and J.Th.M. de Hosson, Rad. Eff. 71,109(1983).
- [2] L.M. Caspers, A. van Veen, Phys. Stat. Sol. (a) 68,339(1981).
- [3] F. Pleiter and C. Hohenemser, Phys. Rev. B 25,106(1982).
- [4] K. Post, F. Pleiter, G.J. van der Kolk, A. van Veen, L.M. Caspers and J.Th.M. de Hosson, Hyperfine Interactions 15/16,421(1983).
- [5] A.A. van Gorkum and E.V. Kornelsen, Rad. Eff. 42,93(1979).
- [6] E.V. Kornelsen and A.A. van Gorkum, Rad. Eff. 42,113(1979).
- [7] A. van Veen, A. Warnaar and L.M. Caspers, Vacuum 30,109(1980).
- [8] G.J. van der Kolk, A. van Veen, L.M. Caspers and J.Th.M. de Hosson, to be published in J. of Nucl. Mat, chapter 4.1.
- [9] K.D. Rasch, R.W. Siegel, H. Schultz, Phil. Mag. A 41,91(1980).
- [10] E.V. Kornelsen, Rad. Eff. 13,227(1972).
- [11] J.Th.M. de Hosson, A.W. Sleeswyk, L.M. Caspers, W. van Heugten and A. van Veen, Sol. State Comm. 18,479(1976).
- [12] A. van Veen, J.H. Evans, W.Th.M. Buters and L.M. Caspers, Rad. Eff. 78,53[1983].
- [13] A. van Veen and L.M. Caspers, Proc. 7<sup>th</sup> Int. Vac. Congr. & 3<sup>d</sup> Int. Conf. Solid Surfaces (Vienna 1977) pp. 2637-2640.



- [14] A. van Veen, L.M. Caspers and B. Nielsen, to be published.
- [15] E.V. Kornelsen, A.A. van Gorkum, J. of Nucl. Mat. 92,79(1980).
- [16] G.J. van der Kolk, A. van Veen, J.Th.M. de Hosson and R.H.J. Fastenau, to be published in Nucl. Instr. and Meth, chapter 3.2.
- [17] H. Frauenfelder and R.M. Steffen, in: Alpha- Beta- and Gamma-Ray Spectroscopy, ed. K. Siegbahn (North Holland, Amsterdam 1966), ch. XIX (A).
- [18] B. Hammatz, Nucl. Data Sheets 27,453(1975).
- [19] A.R. Arends, C. Hohenemser, F. Pleiter, H. de Waard, L. Chow and R.M. Suter, Hyperf. Interact. 8,191(1980).
- [20] U. Pütz, A. Hoffman, H.J. Rudolf and R. Vianden, Z. Physik B46,107(1982).
- [21] A. Weidinger, R. Wessner, E. Recknagel and Th. Wichert, Nucl. Instr. and Meth. 182/183,509(1981).
- [22] M.T. Robinson and H. Torrens, Phys. Rev. B9,5008(1974).
- [23] M. Hou, A. van Veen, L.M. Caspers M.R. Ypma, Nucl. Instr. and Meth. 209/210,19(1983).
- [24] H.H. Neely, D.W. Keefer and A. Sosin, Phys. Stat. Sol. 28,675(1968).
- [25] G.J. van der Kolk, A. van Veen, L.M. Caspers and J.Th.M. de Hosson, to be published in Nucl. Instr. and Meth, chapter 3.1.
- [26] S.R. Reintsema, E. Verbiest, J. Odeurs and H. Pattyn, J. Phys. F. 9,1511(1979).
- [27] E. Verbiest, Ph. D. Thesis, Leuven, Belgium (1983).
- [28] W.D. Wilson and C.L. Bisson, Rad. Eff. 19,53(1973).
- [29] J.N. Mundy, S.J. Rothman, N.Q. Lam, H.A. Hoff and L.J. Nowicki, Phys. Rev. B 18,6566(1978).
- [30] J.R. Manning in: Diffusion Kinetics for Atoms in Crystals (Van Nostrand, New York, 1968), Ch III.
- [31] C.C. Matthai and D.J. Bacon, J. of Nucl. Mat. 114,22(1983).
- [32] A. van Veen, W.Th.M. Buters, G.J. van der Kolk, L.M. Caspers and T.R. Armstrong, Nucl. Instr. and Meth. 194,485(1982).
- [33] M. Koike, K. Furukawa, J. Takamura, H. Hira, N. Yamamoto and F. Nakamura, in Point Defects and Defect Interactions in Metals, eds. J. Takamura, M. Doyama and M. Kiritani, North Holland 1982, pp. 457-460.
- [34] K. Masuda, J. Physique 43,921(1982).



#### 4. INTERACTION OF INTERSTITIALS WITH SUBSTITUTIONAL IMPURITIES IN TUNGSTEN.

##### INTRODUCTORY REMARKS.

In this chapter the interaction of He-interstitials and self-interstitials with metallic impurities in tungsten is studied. The impurities are brought into the sample by ion implantation. Subsequent heating ensures substitutionality of the impurities. Desorption spectra made after low energy He injection yield He dissociation energies from the various metallic impurities. By low energy Xe bombardment self-interstitials are introduced in a controlled way. He injection followed by desorption is used to monitor the conversion of the substitutional impurities to configurations which do not trap He.



#### 4.1. BINDING OF HELIUM TO METALLIC IMPURITIES IN TUNGSTEN; EXPERIMENTS AND COMPUTER SIMULATIONS.

G.J. van der Kolk<sup>1</sup>, A. van Veen<sup>1</sup>, L.M. Caspers<sup>1</sup> and J.Th.M. de Hosson<sup>2</sup>.

<sup>1</sup> Delft University of Technology/Interuniversity Reactor Institute, Mekelweg 15, 2629 JB Delft, the Netherlands.

<sup>2</sup> University of Groningen, Materials Science Centre, Nijenborgh 18, 9747 AG Groningen, the Netherlands.

#### ABSTRACT

A W(100) single crystal was implanted with low doses Ag, Cu, Mn, Cr, Al or In. Subsequent heating to 1600 K removed all vacancies and left the implants in substitutional positions. Low energy He was injected, and binding of He to the substitutional impurities was observed. Binding energies were found as high as 1.25 eV for one He atom. Pair potential calculations were performed; the calculated binding energies corresponded reasonably with the measured ones.

#### 4.1.1. INTRODUCTION.

In future fusion reactors the first wall limiting the plasma will be subjected to high fluences of fast particles escaping from the plasma e.g. hydrogen isotopes and  $^4\text{He}$ . At the same time the build up of an appreciable concentration of H and He via the transmutation reactions (n,p) and (n, $\alpha$ ) is envisaged. It has been shown that clustering of He plays an important or even decisive role in the process that leads to intolerable modification of the first wall (e.g. blistering, swelling). Recently Helium Desorption Experiments (HDS) combined with electron microscopy have improved the insight into the early phase of the He clustering process [1,2]. Various experiments have been performed on low-energy and low-dose He implantation in a.o. single crystals of W, Mo and Ni [3,4,5,6]. In these experiments it was demonstrated that He binds to lattice vacancies with high binding energies. The binding of He to heavier substitutional noble gases was also observed [7]. It was found that the larger the substitutional noble gas atom the smaller the He-binding energy. A very important

result of THDS experiments was that once the first He is bound to a substitutional heavy noble gas atom, the second He atom will be bound more tightly.

It was observed that in Mo this general trend holds for up to at least 1000 He atoms per trap. So any trapping centre for He will act as a nucleation centre for bubbles.

Although tungsten is no candidate material for the first wall of the early generation of fusion reactors, tungsten was studied here, because W or Mo will probably be used in plasma limiters, divertors etc. [8].

Small amounts of the metallic impurities Ag, Cu, Mn, Cr, Al and In are introduced in a W(100) single crystal by 5 keV ion implantation. In all cases annealing at 1600 K is sufficient to evaporate the excess vacancies around the implants so that substitutionality of the implants is ensured. In section 3 it is found that He is bound by the metallic impurities Al, Cr, Ag, Mn and Cu with binding energies ranging from 0.75 eV to 1.25 eV. In section 4 the a model is applied which calculates He binding energies from differences in local electron densities. In section 5 the experimental results and the results of the model calculations are compared and discussed.

#### 4.1.2. EXPERIMENTALLY.

The equipment used in this study has already been described in refs. [9,10]. Basically the equipment consists of a large UHV target chamber being held at a pressure of  $2 \times 10^{-8}$  Pa. In the centre of the chamber a W(100) high purity single crystal is mounted. The sample can be heated by 1.5 keV electron bombardment on the rear. A WRe3%-WRe25% thermocouple is used to measure the temperature of the crystal during computer controlled linear heating with time (the heating rate normally used is 40 K/s). Auxiliary devices are a gas ion source with which low energy He implantation is performed (standard energy 250 eV), a quadrupole mass analyser equipped with an electron multiplier to detect desorbing He, and a metal ion source (5-30 keV acceleration voltage). In the beam line of the metal ion source magnetic deflection over 90 degrees ensures adequate mass separation for our purpose. Both in the gas ion beam and the metal ion beam electrode pairs are mounted which enable sweeping of the beams to provide a uniform distribution of the ions on the crystal surface. The W(100) single crystal is the

same as has been used in ref. [10].

The standard experimental procedure adopted for this study was to bombard the crystal with  $2 \times 10^{12}$  5 keV metal ions  $\text{cm}^{-2}$ . The angle of incidence with respect to the surface normal was about 15 degrees. Following the metal implantation the target was annealed to a certain temperature with a heating rate of 40 K/s. Subsequently  $3 \times 10^{12}$  250 eV  $\text{He}^+$   $\text{cm}^{-2}$  was injected perpendicularly to the surface. He desorption was monitored by the quadrupole mass analyser mentioned above during linear heating with time. The thus obtained spectra were corrected for the residence time  $\tau$  of He in the desorption volume.

#### 4.1.3. EXPERIMENTAL RESULTS.

##### 4.1.3.1. Annealing temperature variation after metal implantation.

In fig. 1 helium desorption spectra are shown for W(100) implanted with  $2 \times 10^{12}$  5 keV  $\text{Ag}^+$   $\text{cm}^{-2}$ , annealed to the indicated temperatures and subsequently injected with  $3 \times 10^{12}$  250 eV  $\text{He}^+$   $\text{cm}^{-2}$ .

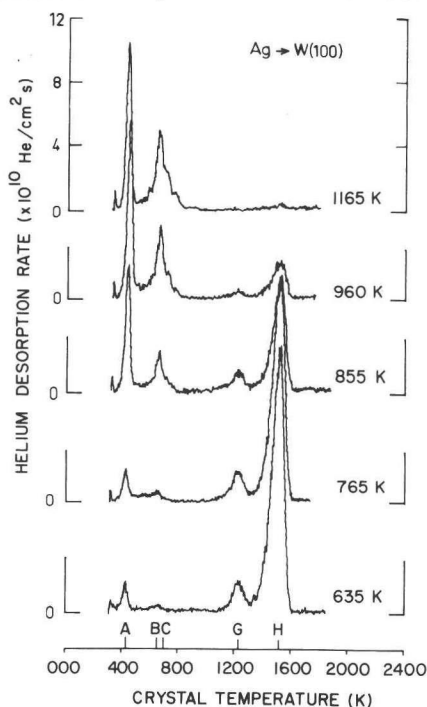


fig. 1: Helium desorption spectra for W(100) implanted with  $2 \times 10^{12}$  5 keV  $\text{Ag}^+$   $\text{cm}^{-2}$ , annealed to the indicated temperatures and subsequently injected with  $3 \times 10^{12}$  250 eV  $\text{He}^+$   $\text{cm}^{-2}$ .

The peaks labelled H and G which are attributed to He release from monovacancies, see ref. [3]. We attribute the peaks labelled A, B and C to He desorbing from substitutional Ag atoms. In section 3.2 this will be elucidated. In fig. 2 the peak populations versus annealing temperature are shown for the G and H peak and the A, B and C peaks.

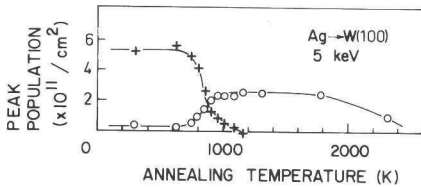


fig. 2: Peak populations as a function of annealing temperature. Bombardment parameters as in fig. 1. (+) sum of G and H, (o) sum of A, B and C.

At around 800 K a steep decrease of the G and H peak population is seen which we attribute to stage III recovery. The empty vacancies become mobile and recombine at the near surface thereby being lost as traps for He. It can be seen that in the same temperature region the A, B and C peaks grow. In ref. [11] it is shown that the suppression of the A, B and C peaks at annealing temperatures below 800 K can be attributed to effects caused by vacancies situated within a distance not larger than 3 lattice constants. Both shielding of substitutional Ag (AgV) by vacancies (V) for migrating He as well as He drainage to and retrapping in nearby vacancies during desorption from AgV occur. Once the nearby vacancies have become mobile a large fraction of them will be trapped by the metal atoms. However the binding energy is so low that at temperatures slightly beyond stage III they will be detrapped and released. For all metallic implants a similar annealing behaviour was found; after 5 keV implantation vacancy type traps disappear at stage III at the same annealing temperature as where the A, B and C peaks appear. It is seen that between 1000 and 1800 K the population of the peaks does not change. This is found to be true for all implants, therefore annealing up to 1600 K ensures that the impurity is in a single state (substitutional) and still does not move out of the crystal by diffusion.

#### 4.1.3.2. Peak assignment.

In fig. 3 helium desorption spectra are shown for W(100) implanted with different metallic impurities, annealed up to 1600 K and injected



with the indicated doses of 250 eV He<sup>+</sup>.

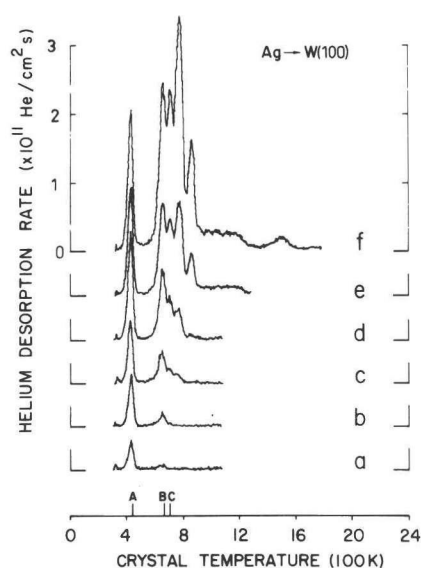


fig. 3a: Desorption spectra of W(100) bombarded with  $2 \times 10^{12}$  5 keV Ag<sup>+</sup> cm<sup>-2</sup>, annealed to 1600 K and injected with 250 eV He<sup>+</sup>, doses are a)  $6.5 \times 10^{11}$  cm<sup>-2</sup>; b)  $1.5 \times 10^{12}$  cm<sup>-2</sup>; c)  $3 \times 10^{12}$  cm<sup>-2</sup>; d)  $6 \times 10^{12}$  cm<sup>-2</sup>; e)  $1.2 \times 10^{13}$  cm<sup>-2</sup>; f)  $2.4 \times 10^{13}$  cm<sup>-2</sup>.

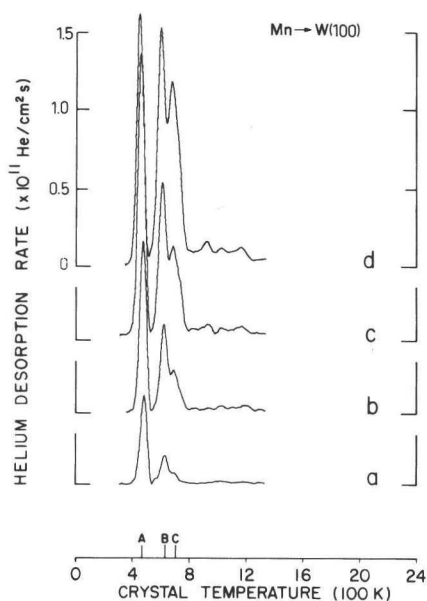


fig. 3b: As in fig. 3a, but for Mn<sup>+</sup>, He doses are a)  $1.7 \times 10^{12}$  cm<sup>-2</sup>; b)  $3.4 \times 10^{12}$  cm<sup>-2</sup>; c)  $5.2 \times 10^{12}$  cm<sup>-2</sup>; d)  $8.6 \times 10^{12}$  cm<sup>-2</sup>.

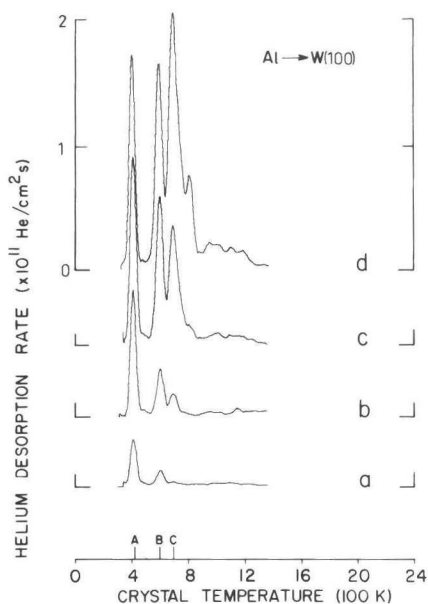


fig. 3c: As in fig. 3a, but for  $\text{Al}^+$ , He doses are a)  $1.3 \times 10^{12} \text{ cm}^{-2}$ ; b)  $3 \times 10^{12} \text{ cm}^{-2}$ ; c)  $6 \times 10^{12} \text{ cm}^{-2}$ ; d)  $1.2 \times 10^{13} \text{ cm}^{-2}$ .

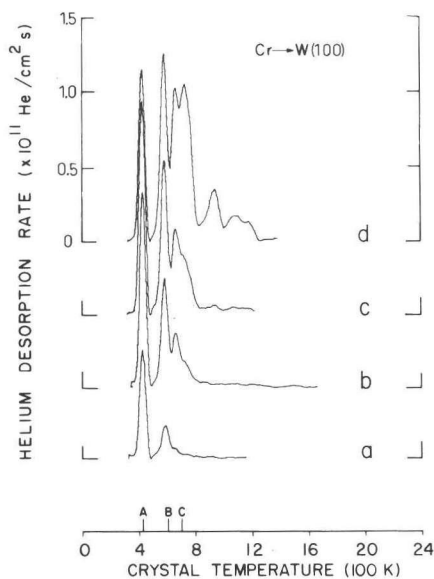


fig. 3e: As in fig. 3a, but for  $\text{Cr}^+$ , He doses are a)  $1.7 \times 10^{12} \text{ cm}^{-2}$ ; b)  $4 \times 10^{12} \text{ cm}^{-2}$ ; c)  $6 \times 10^{12} \text{ cm}^{-2}$ ; d)  $1.2 \times 10^{13} \text{ cm}^{-2}$ .

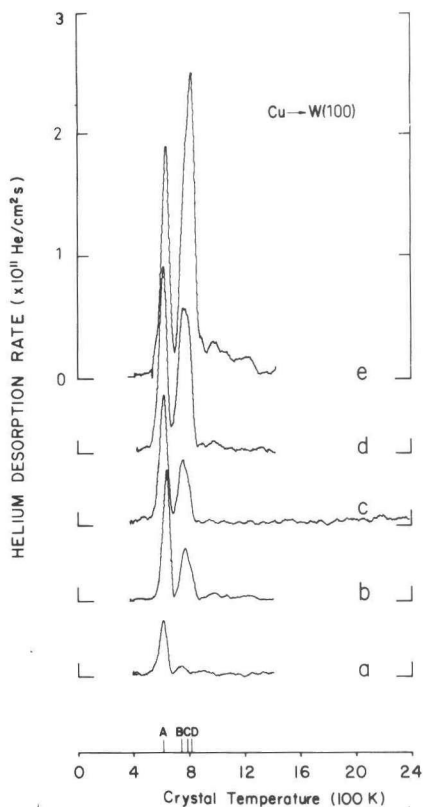


fig. 3d: As in fig. 3a, but for  $\text{Cu}^+$ , He doses are a)  $1 \times 10^{12} \text{ cm}^{-2}$ ; b)  $2 \times 10^{12} \text{ cm}^{-2}$ ; c)  $3.2 \times 10^{12} \text{ cm}^{-2}$ ; d)  $5.8 \times 10^{12} \text{ cm}^{-2}$ ; e)  $7.5 \times 10^{12} \text{ cm}^{-2}$ .

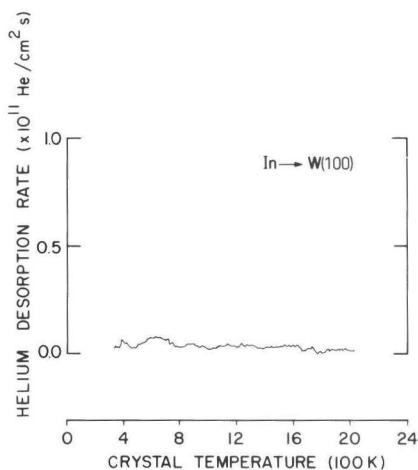


fig. 3f: As in fig. 3a, but for  $\text{In}^+$ , He dose is  $3 \times 10^{12} \text{ cm}^{-2}$ .

It is seen that for most implants the peak profile is similar, the peak temperatures depend a little on the implanted species. It should be noted that in the case of In implantation no peaks are visible, indicating that the binding energy of He to substitutional In is too low to permit permanent binding at room temperature. Beside the A, B and C peaks already observed in the previous section extra peaks are seen to develop at temperatures above the C peak. The peak populations of the Ag implanted series are shown in fig. 4.

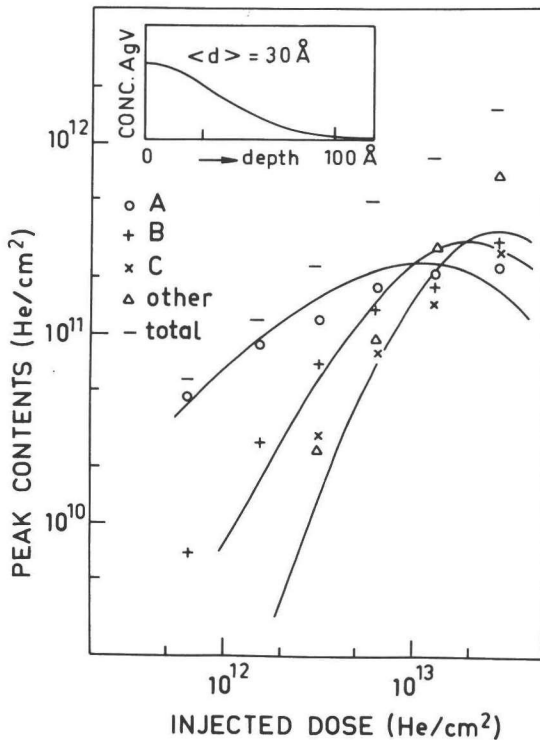


fig. 4: Individual peak populations as a function of He dose for Ag implanted W, bombardment and annealing parameters as in fig. 3a. (o) peak A, (+) peak B, (x) peak C, ( $\Delta$ ) other peaks, (-) total. Drawn curves are calculated for a He range of 60 Å, and the Ag distribution shown in the inset. For details see text.

It should be noted that due to the low desorption temperature the first peak shown here was not detected in earlier experiments [10]. The peak evolution as a function of He dose corresponds with the behaviour expected for traps which bind He with increasing binding ener-

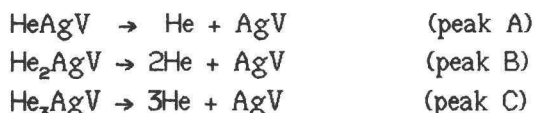
gies. Trapping of one He atom by a trap should increase linearly with dose, a peak representing trapping of 2 He atoms should increase approximately quadratic. Furthermore since the second He atom is bound more strongly than the first one two He atoms will be released once the dissociation temperature for the second He atom is attained. Thus for higher He doses the B peak will be higher than the A peak. The peak evolution can be calculated with a model described in [12]. The trap distribution, the capture constant for He trapping and the He range are model parameters. With the model the depth dependent stationary He concentration is calculated applying diffusion theory to the initial He range. From the thus obtained stationary He distribution and given trap distribution He trapping probabilities and thus peak populations as a function of He dose are obtained. The best fit is shown in fig. 4 (drawn curves). For this fit it had to be assumed that one He desorbs in the A peak, two in the B peak and three in the C peak. The drawn curves were calculated for an average He penetration depth of 60 Å, an entrance probability of 0.85 [13] and a capture constant of 1.15 [14]. The average depth of Ag was taken as 30 Å, the Ag distribution is shown in the inset of fig. 4. Binary collision simulations with the programme Marlowe predict a rather broad Gaussian distribution with an average depth of 18 Å or 63 Å for 5 keV Ag implanted into W(100) at angles of respectively 20 and 10 degrees off the surface normal. The number of traps which had to be substituted in the model calculations to obtain a reasonable fit with the experimental data was  $8.3 \times 10^{14} \text{ cm}^{-2}$ .

Sticking probabilities for 5 keV Kr and Xe on W were reported to be about 0.6 to 0.7 [15]. We expect the same sticking probability for Ag. The heating to 1600 K applied in this study will have removed a fraction of the Ag atoms of 0.3 as well. So the number of traps deduced from the peak populations is in fair agreement with what is expected for the implanted dose of  $2 \times 10^{12} \text{ 5keV Ag}^+ \text{ cm}^{-2}$ .

In the next lines we will argue that the implanted impurity atoms are located in substitutional positions. (i) According to an empirical rule formulated by Sood [16] an implanted species will be in a substitutional position if: a) the atomic radius is within -15% and +40% of that of the host, and b) the electronegativity according to the Gordy scale (ref.[17]) is within 0.7 of the electronegativity of the host. For all implants except In this is the case. (ii) Further experimental evidence follows from the desorption spectra. All vacancy type traps

are removed after annealing to above stage III, see the previous section. For all implants except In the behaviour was totally analogous to He binding to substitutional Ar, Kr and Xe. Substitutionality of the noble gas implants after annealing was proven experimentally [18,19]. The binding energy observed here for the first He atom is of the same magnitude as that of He to KrV (1.7 eV) or to XeV (1.2 eV) in tungsten. Furthermore the feature that the second and third He atom are stronger bound than the first in the case of substitutional Ar, Kr and Xe holds for the metallic impurities as well.

Having established that the trap is a substitutional Ag atom, we make the following peak assignments:



The peaks emerging at higher He doses will correspond with desorption of more than 3 He atoms from a Ag atom.

For all other implants except In similar peak patterns were found with a similar peak evolution as a function of He dose for the A, B and C peaks. So peak assignments as above can be made, but for Ag is X, with X=Al, Cr, Cu and Mn.

#### 4.1.3.3. Peak fitting.

Helium desorption peaks from low concentration simple defects and low helium filling can be described by a single step dissociation process followed by diffusion to the surface. In W at room temperature the first process is dominant due to the low interstitial migration energy for He of 0.3 eV [20,21]. Therefore the He release rate  $R(t)$  can be described by the formula:

$$R(t) = \nu_0 c(t) \exp(-E^d/kT(t)) \quad (1)$$

with  $c(t)$  the concentration of He filled defects at time  $t$ ,  $E^d$  the dissociation energy,  $\nu_0$  the zero temperature jumping frequency,  $k$  the Boltzmann factor and  $T(t)$  the temperature at time  $t$ . In principle  $E^d$  and  $\nu_0$  can be derived from a single experiment by matching the observed peak with a numerically obtained solution of equation (1). In

fig. 5 several fitting curves are shown for an A peak of Ag in W. For a fixed value of  $\nu_0$  values of  $E^d$  were chosen so that the left side of the peak was fitted well. It can be seen that the calculated peak for  $\nu_0 = 5 \times 10^{11} \text{ s}^{-1}$  is too broad whereas the others are too narrow. The accuracy of this method is limited;  $\nu_0$  is estimated to be between  $5 \times 10^{11}$  and  $5 \times 10^{13} \text{ s}^{-1}$ . In this particular case the peak suffered only a minimal shape distortion; the average residence time  $\tau$  of He in the mass spectrometre volume was quite short ( $< 0.05 \text{ s}$ ) and the width of the peak in the time domain rather large relative to  $\tau$  due to the low heating rate ( $\beta = 20 \text{ K/s}$ ). Despite of this we were unable to match the peak perfectly, the residue of the measured peak after subtraction of the calculated peak always showed a small deviation at the high temperature side of the peak. This can be understood in the following way. There is a small fraction of He entering small volumes where the average pumping speed will be much lower, thus leading to a larger average residence time for a fraction of the He atoms. This will enlarge the tail of the peak.

An alternative method for obtaining  $\nu_0$  is to extract the maximum peak temperature  $T_m$  for different linear heating rates  $\beta$ . The following equation should be fulfilled under the assumption that  $\nu_0$  is independent of temperature:

$$\frac{E^d}{kT_m} = -\ln \frac{\beta E^d}{\nu_0 kT_m^2} \quad (2)$$

A plot of  $\ln \beta / T_m^2$  versus  $1/T_m$  should be a straight line from which both  $E^d$  and  $\nu_0$  can be determined. Fig. 6 shows such a plot for the A peak in the desorption spectrum of Ag implanted W.

The errors in the dissociation energy and the jumping frequency are mainly determined by three effects. The largest error is introduced by the uncertainty of the temperature of the cold joint of the thermocouple which is inside the UHV chamber. Especially at the low peak-temperatures in this study this can introduce an error of 1.5% in the absolute value of  $T_m$ . Another error may be introduced by the data acquisition system. This error was kept within 0.5%. The error in the thermocouple is according to the manufacturer less than 1%. A small error is introduced by fluctuations of the heating rate  $\beta$ . For spectra with  $\beta$  below 80 K/s this error was estimated to be less than 3%. Differentiation of relation (2) with respect to the different physical parameters shows that for the uncertainties quoted above the errors in

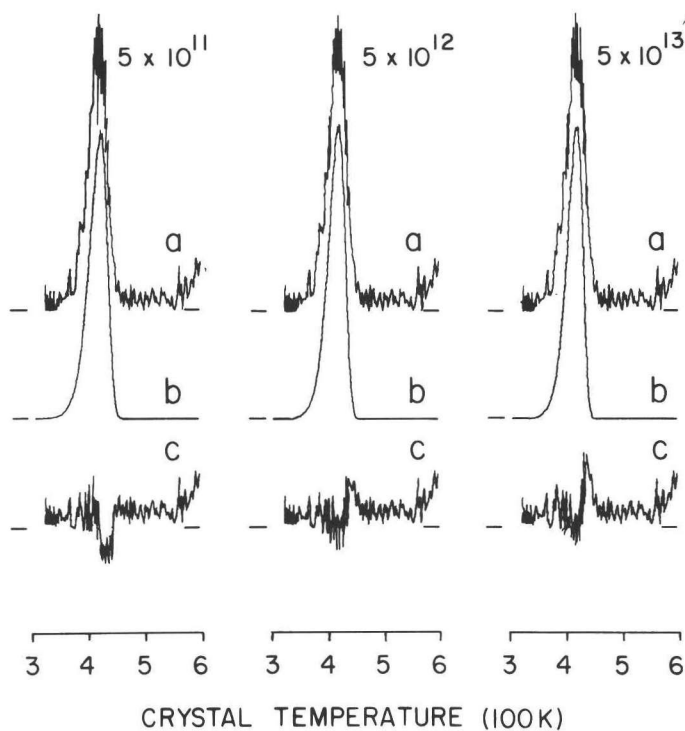


fig. 5: Comparison between the A peak of W(100), implanted with  $2 \times 10^{12}$  5 keV  $\text{Ag}^+$   $\text{cm}^{-2}$ , annealed to 1600 K and injected with  $3 \times 10^{12}$  250 eV  $\text{He}^+$   $\text{cm}^{-2}$  (heating rate is 20 K/s), and calculated peaks. a) spectrum; b) calculated peak; c) difference of a) and b).

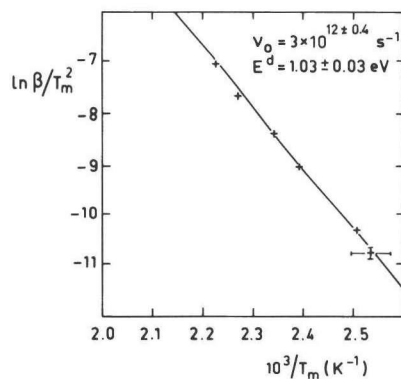


fig. 6: Plot of  $\ln \beta / T_m^2$  versus  $1/T_m$  for the A peak observed for Ag implanted W.

$E^d$  and  $\ln \nu_0$  are largely determined by the uncertainty of  $T_m$  and are 3%. The best fit (least square analysis) is shown in the figure. The result is that  $E^d = 1.03 \pm 0.03$  eV and  $\nu_0 = 3 \times 10^{12 \pm 0.4}$  s<sup>-1</sup>. These data agree with the peak fitting results in fig. 5. Furthermore the result is in line with the expected frequency which should be approximately the same as the Debye frequency (for W  $\sim 8 \times 10^{12}$  s<sup>-1</sup>) since He dissociation from substitutional atoms is likely to be governed by vibrations in the surrounding lattice. Peak fitting of results for other implants showed no deviations from the jumping frequency found above, therefore all dissociation energies given in table 1 are based on a value of  $\nu_0$  of  $3 \times 10^{12}$  s<sup>-1</sup>.

table 1: Experimentally derived dissociation energies (eV) for He from implanted impurities in W,  $\nu_0$  was taken  $3 \times 10^{12}$  s<sup>-1</sup>.

implant	peak A	peak B	peak C
Ag	$1.03 \pm 0.03$	1.57	1.71
Cu	1.48	1.79	1.88
Al	0.99	1.46	1.69
Mn	1.13	1.51	1.70
Cr	1.02	1.41	1.61
In	<0.90		

#### 4.1.3.4 He precipitation at high dose He injection.

It was shown recently with HDS that substitutional noble gas atoms in tungsten act as non-saturable traps for helium. The non-saturable traps could be grown with non-damaging low energy He into helium-precipitates containing up to 150 He atoms [18,1]. Injection of 250 eV He up to very high doses in W(100) bombarded with 5 keV Ag and annealed up to 1600 K showed that the He binding energy continues to increase with increasing filling degree. The spectra are similar to those obtained by Kornelsen and van Gorkum [17] on substitutional Ne, Ar, Kr and Xe in W for similar filling degrees. Two spectra are shown in fig. 7; the A, B and C peaks are still visible, but most of the He is trapped with high binding energies. The three large peaks at higher temperature are identical with the peaks found by ref.[18] for a He occupancy per trap ranging from 20 to 90 He atoms.



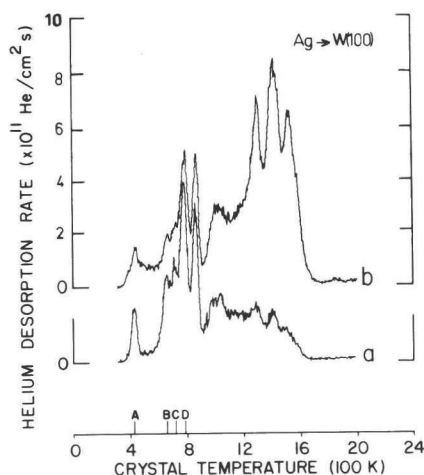


fig. 7: Spectra of W bombarded with  $2 \times 10^{12}$  5 keV  $\text{Ag}^+$   $\text{cm}^{-2}$ , heated to 1600 K and injected with 250 eV  $\text{He}^+$ , doses are a)  $6 \times 10^{13} \text{ cm}^{-2}$ ; b)  $1.2 \times 10^{14} \text{ cm}^{-2}$ .

For the other metallic implants except In similar He precipitation at higher He doses takes place (the first He atom does not bind to In in W at room temperature).

#### 4.1.4. STATIC LATTICE CALCULATIONS.

##### 4.1.4.1. PAIR POTENTIALS.

Static lattice calculations were performed using a model in which a small crystallite of  $13 \times 13 \times 13 \text{ a}_0^3$ , containing a defect in the centre, is allowed to relax to the lowest energy. The method is described in ref. [22]. The interaction between two atoms is described with a two-body interaction function, the pair-potential. The results rely on a proper choice of pair potentials. For the W-W potential the potential derived by Johnson and Wilson [23] was used. This potential is based on elastic constants and gives a suitable estimation of the displacement of lattice atoms on which a force is exerted. The He-metal potentials were calculated using a program of M. Baskes [24], in which the modified Wedepohl method [25,26] is used to derive the pair potential from the radial electron density obtained with

Hartree-Fock-Slater calculations (see ref. [27]). The He-metal pair potentials calculated this way predict He-vacancy binding energies for Mo and W which are in close agreement with recent Helium Desorption measurements; the predicted dissociation energies are respectively 4.19 and 4.75 eV, the experimental values are  $3.8 \pm 0.2$  and  $4.64 \pm 0.04$  eV respectively.

The W-X potential with X the impurity was not available in literature, therefore an approximation had to be found which described the correct relaxation of the impurity atom in the vacancy with a He atom bound to it. In view of the noble gas results it is clear that the size of the impurity plays a role. The size of the impurity is largely determined by its atomic volume in pure form. For most alloys a volume contraction is observed relative to the volumes of the alloying components. Therefore in this section a correction will be applied to the atomic volume of X.

In short the method applied was scaling of the W-W potential to a potential representing a bcc X-X interaction. The average between pure W-W and the thus calculated X-X potential was taken to obtain the X-W potential. This approach seems to be quite crude; however results obtained by Machlin, Maeda and Vitek [28,29,30,31] suggest that it might work satisfactory for some problems. The different steps will be discussed below. Both the potential range and the potential minimum must be scaled.

To adapt the potential range of the W-W potential, so that a X-X potential is obtained, the radii of X and W should be compared. Often half the first neighbour distance is taken as the radius of an atom, in our case however atoms of unlike structure were placed in a bcc structure. Therefore first of all a correction should be made for forcing the atoms in a bcc structure. E. Machlin [28] has estimated these size corrections, his values were applied in this study. According to several authors the volume contraction upon alloying depends on the difference in electronegativity of the two constituents [28,30,31]. A formula describing this contraction given in ref. [29] and which will be used in this study is as follows:

$$D^{\alpha*} = \frac{D^{\alpha}}{[1 - 0.75 S_{\alpha} t_{\beta \rightarrow \alpha} / (X_{\alpha} - 0.5)]} \quad (3)$$

with  $D^{\alpha}$  the nearest neighbour distance of  $\alpha$  (in a bcc structure in our case),  $D^{\alpha*}$  is the corrected nearest neighbour distance,  $S_{\alpha}$  is the

screening constant tabulated in ref.[28], and  $t_{\beta \rightarrow \alpha}$  the charge transfer from element  $\beta$  to element  $\alpha$ ,  $X_\alpha$  is the electronegativity of  $\alpha$  according to Gordy [17]. Since in our case a very diluted alloy is concerned of  $X$  in  $W$  the charge transfer of neighbouring  $W$  atoms should be minus  $1/8$  of the charge transfer of  $X$  to preserve electroneutrality. From relation (3)  $D^{X*}$  and  $D^{W*}$  follow. To rescale  $W-W$  into  $W-X$  the potential range was scaled with the following factor:  $f=(D^{X*}+D^{W*})/2D^W$ .

To scale the potential minimum a variety of physical parameters as cohesive energy, vacancy formation energy and bulk modulus can be taken. In this context however it should be realized that the Johnson-Wilson  $W-W$  potential belongs to a class of potentials which do not aim to describe correct cohesive energies but is constructed to give proper displacements of atoms on which a force is exerted. The vacancy formation energy obtained with this potential is not correct (1.8 eV too low). Since in this study the interest is focussed on the displacement of an atom  $X$  in a  $W$  matrix on which a repulsive force is exerted by a He atom the bulk modulus  $B$  might be the suitable parameter to look at. Under the assumption that the energy-variation of metals under volumetric changes can be described by a pair potential  $\phi$  of the same functional form, so that the potentials can be transformed into any other by scaling the  $r$  and the potential minimum, it can be shown that:

$$\frac{B_X}{B_W} = \frac{\eta^3}{\gamma} \quad (4)$$

with  $\eta = r_W/r_X$  and  $\gamma = \phi_W^{\min}/\phi_X^{\min}$ . With the value of  $\eta$  as derived from the range scaling  $\gamma$  can be calculated. Reynolds and Couchman [32] have used this relation with the assumption that the minimum of a pair potential is directly related to the vacancy formation energy  $E_V^f$  to demonstrate that there are three classes of metals for which the product of  $B.V/E_V^f$  is a constant within a class, with  $V$  the atomic volume. Taking more recent data for the vacancy formation energy only one class can be distinguished with a few exceptions (Zn, Au, Pt). The same relation can be applied to show that  $B.V/E_{coh}$  should be constant, with  $E_{coh}$  the cohesive energy. Within a row of the periodic system this holds fairly well, but for totally different metals  $B.V/E_{coh}$  can deviate a factor two. So the accuracy of the scaling of the potential minimum will not be too good, especially for totally unlike metals.

## 4.1.4.2. Calculated results.

In table 2 the results are shown calculated for different X-W and X-He potentials. For the X-W respectively is taken: the pure W-W potential, the W-W potential with scaled range, and the W-W potential with both range and minimum scaled. For the He-X potential two different potentials were taken, one calculated for a singly ionized X atom and one calculated for a neutral X atom.

**table 2:** Calculated binding energies  $E^b$  (eV) for He to substitutional impurities in tungsten. In set I for X-W is taken pure W-W. In set II for X-W is taken pure W-W with scaled range. In set III for X-W is taken pure W-W with scaled range and minimum. For the He-X interaction both He-X and He-X<sup>+</sup> were taken. In the last column binding energies obtained with (5) from experimental dissociation energies are shown.

impurity X	set I	set II	set III	experiment
Ag	0.44	0.38	0.55	0.78
Ag <sup>+</sup>	0.80	0.75	0.92	
Cu	0.84	1.14	1.30	
Cu <sup>+</sup>	1.20	1.51	1.67	1.23
Al	0.78	0.96	1.13	
Al <sup>+</sup>	1.08	1.26	1.42	
Mn	0.59	0.92	1.07	0.74
Mn <sup>+</sup>	0.90	1.23	1.37	
Cr	0.70	1.00	1.12	
Cr <sup>+</sup>	1.06	1.36	1.49	0.77
In	0.24	0.21	0.25	
In <sup>+</sup>	0.52	0.50	0.54	

From the table it can be learned that for most implants range scaling supplies the dominant correction to the He binding energy compared with the case that the unscaled W-W potential is taken for the W-X interaction. In the last column of the table the experimentally measured dissociation energies are shown. The relation between dissociation energy  $E^d$  and binding energy  $E^b$  is mostly assumed to be:

$$E^d = E^b + E^m \quad (5)$$

with  $E^m$  the migration energy. In tungsten the migration energy of He was calculated to be  $E_{He}^m = 1.25$  eV by ref. [20]. To test the validity of eq. (5) for our case calculations were performed applying the He-Ag<sup>+</sup> potential of He, migrating away from a substitutional Ag atom. In fig.

8 the migration path and corresponding energy variations of the crystallite are shown. The W atoms and the Ag atom were allowed to relax fully, with the He atom held fixed at various positions. The results point out that the first energy barrier is 0.15 eV higher than the binding energy. For  $\text{Cu}^+$  this figure was 0.24 eV, therefore it seems to be justified to compare the measured dissociation energies minus 0.25 eV directly with the calculated He binding energies.

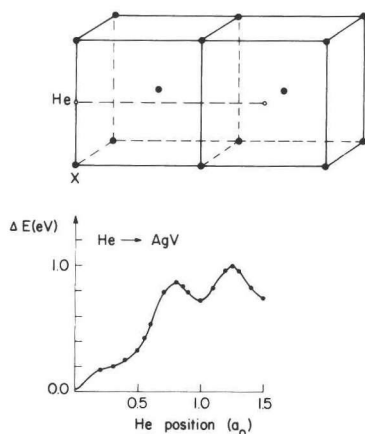


fig. 8: Calculated energy variation of a microcrystallite ( $13 \times 13 \times 13 \text{ a}_0^3$ ) upon dissociation of a He-AgV complex, the microcrystallite was allowed to relax fully with the He atom fixed at various positions along the indicated line.

In doing so (table 2) it seems that the calculated energies agree fairly well with the measured ones presumed that  $\text{He-X}^+$  is taken for  $\text{X=Ag, Cu}$ , and that the W-X potential is obtained by scaling the range of the W-W potential. It should be noted that in the original work in which the method of calculating the He-X potential is described for  $\text{X=Ag, Cu}$  or Au also the singly ionized X atom was taken, see ref. [21]. Bearing in mind the large uncertainty in the accuracy of the scaling of the potential minimum it is not surprising that this scaling tends to overestimate the relaxation of the impurity atoms, the more so since some relaxation effects are already incorporated due to the volume correction for charge transfer.

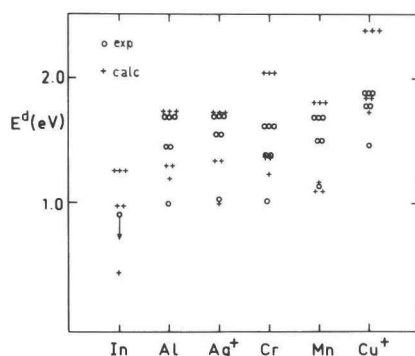


fig. 9: Dissociation energies for He from substitutional impurities in tungsten, open circles are experimentally obtained, plusses are calculated. The number of circles c.q. plusses indicates the number of He atoms concerned.

In fig. 9 calculated dissociation energies are compared with measured ones for up to three He per trap. The trends are reproduced.

#### 4.1.5. DISCUSSION.

Binding of He to substitutional metallic impurities in tungsten is observed. The binding energies for the first He atom are as high as 1.25 eV depending on the implant. The rather interesting point is that chromium in tungsten binds He with 0.77 eV. Cr and W have a mutual though limited solubility in each other at room temperature, above 1800 K a complete series of solid solutions exists, as reported by Greenaway [33]. Thus this result strongly suggests that in alloys relatively strong binding of He to one of the species may occur at room temperature.

It should be realized however that tungsten is one of the most favourable metals for observing He binding to impurities since the interstitial He formation energy is rather high (>5 eV) due to the high interatomic electron density [34]. Implants with lower electron densities than tungsten will bind He. Although hidden in the pair-potential approach the model described is based on the local electron density. The latter depends on the impurity and the possibility for the impurity to relax in the vacancy under influence of a He atom. Calculations on He-metal interactions were recently performed by Manninen et al. [34,35] for the 3d metals, using a different calculation scheme. It is interesting to note that they found a He-Mn repulsion weaker than the He-Cr repulsion. They ascribed this to magnetic effects of Mn. The He-Mn calculated with the modified Wedepohl is more

repulsive than the He-Cr interaction calculated with this method. In the experiments the findings of ref. [34] are reproduced; the He-Mn interaction is weaker, resulting in a stronger binding of He to substitutional Mn than to Cr.

#### 4.1.6. APPLICATION.

A possible application of the finding in this study that the He interaction with metallic impurities in metals can be understood in terms of local electron densities can be the calculation of the behaviour of He in alloys. The most obvious problem is the behaviour of He in the first wall of a fusion reactor. The first wall limiting the plasma will probably be a stainless steel alloy, containing precipitates and transmutation products, see ref. [35]. For stainless steel (SS 316) the He-X interaction functions were calculated for the different alloying elements Fe, Ni, Cr, Mn and Ti, see fig. 10.

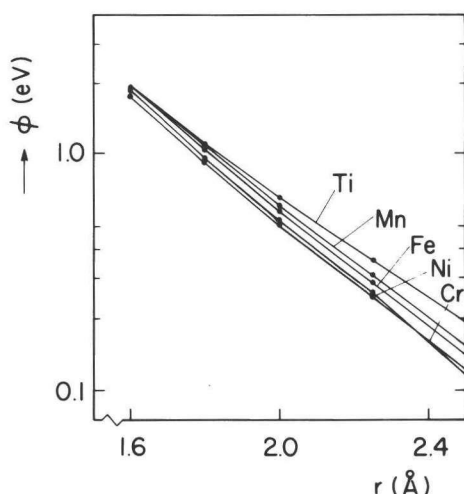


fig. 10: He-metal pair potentials in the intermediate region.

Relaxation effects will play a smaller role since atomic volume and compressibility of the constituents are similar except for Ti. The He-metal separation will be approximately  $0.54a_0$ , (see ref. [21]) which corresponds with  $1.9 \text{ \AA}$ . At this separation the He-X interaction potentials only differ 0.1 eV, thus it will only result in a slightly higher effective He migration energy than in pure Ni.

For precipitates a totally different picture holds. We may expect that the minimum binding energy of He to a precipitate in SS 316

equals the difference in interstitial formation energy of He in Ni or Fe and the corresponding energy in the precipitate. Manninen et al. [34,35] calculated the heat of solution for He in 3d transition metals. From their results we expect that the binding energy of one He atom to a Ti precipitate in Fe is about 1 eV. Due to the large size mismatch the electron density at the interface will locally be considerably lower, resulting in an enhanced binding. Experimentally strong He binding has been observed for TiC precipitates in SS 316, see ref. [37].

This work was part of the research programme of the Stichting voor Fundamenteel Onderzoek der Materie (Foundation for Fundamental Research on Matter) and was supported financially by the Nederlandse Organisatie voor Zuiver Wetenschappelijk Onderzoek (Netherlands Organization for the Advancement of Pure Research).

#### REFERENCES.

- [1] A. van Veen, A.J.H. Evans, W.T.M. Buters and L.M. Caspers, to be published in Rad. Eff.
- [2] J.H. Evans, A. van Veen and L.M. Caspers, Scripta Met. 17,549(1983).
- [3] E.V. Kornelsen, Rad. Eff. 13,227(1972).
- [4] A. van Veen, L.M. Caspers, E.V. Kornelsen, R. Fastenau and A. van Gorkum, Phys. Stat. Sol. A40,235(1977).
- [5] D. Edwards Jr and E.V. Kornelsen, Surf.Sc. 44,1(1974).
- [6] S.E. Donnelly, Vac. 28,163(1978).
- [7] E.V. Kornelsen, A.A. van Gorkum, J. of Nucl. Mat. 92,79(1980).
- [8] M. Ulrickson, J. of Nucl. Mat. 85/86,231(1979).
- [9] A. van Veen, A. Warnaar and L.M. Caspers, Vac. 30,109(1980).
- [10] G.J. van der Kolk, A. van Veen, L.M. Caspers and J.Th.M. de Hosson, Rad. Eff. 71,109(1983).
- [11] G.J. van der Kolk, K. Post, A. van Veen, F. Pleiter and J.Th.M. de Hosson, to be published in Rad. Eff, chapter 3.3.
- [12] A.A.van Gorkum, E.V. Kornelsen, Rad. Eff. 42,93(1979).
- [13] E.V. Kornelsen, A.A. van Gorkum, Rad. Eff. 42,113(1979).
- [14] G.J. van der Kolk, A. van Veen, J.Th.M. de Hosson and R.H.J. Fastenau, to be published in Nucl. Instr. and Meth.



chapter 3.2.

- [15] E.V. Kornelsen and M.K. Sinha, J. of Appl. Phys. 39,4546(1968).
- [16] D.K. Sood, Phys. Lett. 68A,469(1978).
- [17] W. Gordy, Phys. Rev. 69,604(1946).
- [18] A. van Veen, W.Th.M. Buters, G.J. van der Kolk, L.M. Caspers and T.R. Armstrong, Nucl. Instr. and Meth. 194,485(1982).
- [19] A. van Veen, W.Th.M. Buters, T.R. Armstrong, B. Nielsen, K.T. Westerduin, L.M. Caspers and J.Th.M. de Hosson, Nucl. Instr. and Meth. 209/210,1055(1983).
- [20] A. Wagner and D.N. Seidman, Phys. Rev. Lett. 42,515(1979).
- [21] W.D. Wilson and R.A. Johnson in Interatomic Potentials and Simulation of Lattice Defects, eds. P.C. Gehlen, J.R. Beeler Jr. and R.I. Jaffee (Plenum Press, New York 1972) p. 375.
- [22] J.Th.M. de Hosson in Interatomic Potentials and Crystalline Defects, ed. J.K. Lee (Michigan 1981) p.3.
- [23] R.A. Johnson and W.D. Wilson, *ibid* [13] p.301.
- [24] M. Baskes, private communication.
- [25] P.T. Wedepohl, Proc. Phys. Soc. 92,79(1967).
- [26] W.D. Wilson and C.L. Bisson, Phys. Rev. B 3,3984(1971).
- [27] F. Herman and S. Skillman, Atomic Structure Calculations (Prentice Hall Inc, New Jersey, 1963).
- [28] E.M. Machlin, Acta. Met. 22,109(1974), 22,367(1974), 22,367,(1974), 22,1433(1974).
- [29] E.M. Machlin in Theory of Alloy Phase Formation Ed. by L.H. Bennett, (New Orleans 1979) p. 127.
- [30] K. Maeda, V. Vitek and P. Sutton, Acta. Met. 30,2001(1982).
- [31] V. Vitek and Y. Minonishi, to be published in Surf. Sc.
- [32] C.L. Reynolds and J.R. Couchman, Phys. Lett. 50A,157(1974).
- [33] H.T. Greenaway, J. Inst. Met. 80,589(1951,1952).
- [34] M. Manninen, J.K. Norskov and C. Umrigar, J. Phys. F. 12,L7(1982).
- [35] M.J. Puska, R.M. Nieminen and M. Manninen, Phys. Rev. B. 24,3037(1981).
- [36] R.W. Conn, J. of Nucl. Mat. 103,7(1981).
- [37] W. Kesternich and J. Rothaut, J. of Nucl. Mat. 103,845(1981).



## 4.2. INTERACTION OF SELF-INTERSTITIALS WITH METALLIC IMPURITIES IN TUNGSTEN OBSERVED WITH THDS

G.J. van der Kolk<sup>1</sup>, A. van Veen<sup>1</sup>, L.M. Caspers<sup>1</sup> and J.Th.M. de Hosson<sup>2</sup>.

<sup>1</sup> Delft University of Technology/Interuniversity Reactor Institute Delft, Mekelweg 15, 2629 JB Delft, The Netherlands

<sup>2</sup> University of Groningen, Materials Science Centre, Nijenborgh 18, 9747 AG Groningen, the Netherlands.

### 4.2.1. INTRODUCTION.

The interaction of a self-interstitial atom (SIA) with an impurity atom leads in many cases to the trapping of the SIA [1,2,3]. The understanding of the properties of trapping and release of SIAs turns out to be of crucial importance for the correct description of defect production and impurity segregation in metals under particle irradiation [4]. Most work on trapping of SIAs has concentrated on fcc metals; however, a few studies were published recently devoted to trapping of SIAs in bcc metals by among others Mansel et al. [5] using Mössbauer spectroscopy and Ecker [6] using proton induced X-ray emission in a channeling set-up. These results indicate that in Mo a Mo-Co  $\langle 110 \rangle$  mixed dumbbell is formed which is stable at least up to stage III temperature. At this temperature they are "eaten" by the then mobile vacancies. Thermal Helium Desorption Spectrometry (THDS) has proven to be a useful tool to monitor the reaction of SIAs with substitutional noble gas atoms (He, Ne, Ar, Kr) in Mo and Ni, see the earlier work of the authors [7,8]. In most cases it appeared that the noble gas atom was converted from a substitutional to an interstitial position, thereby becoming mobile (at room temperature).

In this study we report THDS results obtained for interaction of SIAs with the substitutional metallic impurities Ag, Cu and Al in tungsten. Similarly as in [7,8] SIAs were generated by low energy Xe bombardment ( $E=100-250$  eV). From experiments and simulations, see e.g. [9] and [10], it is known that via the process of replacement collision sequences the SIAs, produced by the Xe atoms, are thermalized at a larger depth than where the vacancies are produced. The latter are

produced in the first layers at the low implantation energies employed. The length of the replacement collision sequences is unknown, but model calculations predict an average number of replacements of 4 to 7 [11]. That the SIAs are able to encounter traps at depths of at least up to 900 Å in W(100), as shown by the authors [12], must therefore be caused by interstitial migration.

#### 4.2.2. EXPERIMENTAL RESULTS.

A high purity W(100) single crystal was used in the desorption spectrometer HDS3. For details of the equipment and the cleaning procedure of the crystal see [13]. In fig. 1 spectra are shown of He dissociating from monovacancies in W.

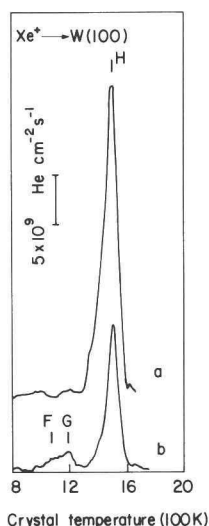


fig. 1: Helium desorption spectrum for HeV defects created by (a) 4 keV He ions in W(100) followed by annealing to 1200 K and (b) as (a), but now post irradiated with  $10^{15}$  100 eV Xe<sup>+</sup> cm<sup>-2</sup>.

The HeVs were obtained by bombardment of W(100) with 4 keV He followed by annealing to 1200 K to dissociate multiple filled Vs. After bombardment with  $10^{15}$  100 eV Xe<sup>+</sup> cm<sup>-2</sup> the number of HeVs has decreased. The reaction:



has taken place, a fraction of the released He atoms are trapped by HeVs already present thus forming He<sub>2</sub>Vs (G peak). The coefficient for

self-interstitial capture  $\mu_i$ , defined by:

$$\mu_i = - \frac{1}{N} \frac{dN}{dP} \quad (2)$$

where  $N$  is the number of defects and  $P$  is the Xe dose, is approximately constant for different Xe doses, as shown in ref. [12].

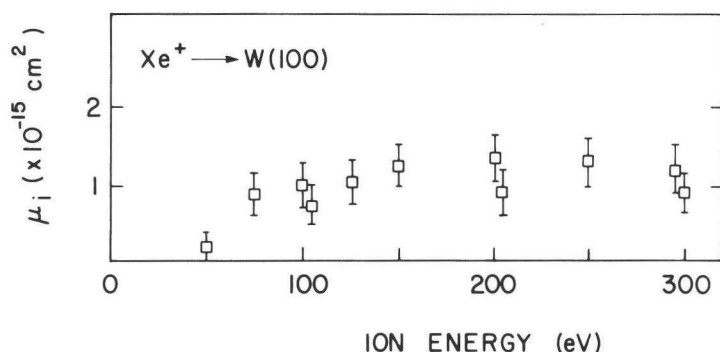


fig. 2: The measured SIA capture coefficient  $\mu_i$  versus the ion energy for Xe on W(100).

In fig. 2  $\mu_i$  is shown as a function of the Xe energy for reaction (1).

Substitutional X atoms with X= Ar, Ag, Cu and Al in W were subjected to reactions with SIAs. The impurity atoms were brought into the sample by 5 keV implantation at an angle of about 15 degrees with respect to the surface normal. Doses were typically about  $2 \times 10^{12} \text{ cm}^{-2}$ . Substitutionality of the implants was ensured by heating to 1800 K, see ref. [14]. A few illustrative spectra are shown in fig. 3 of He desorbing from substitutional Ag and Cu, prior to (a), and after low energy Xe bombardment (b). Since binding energies of He to the impurities are in the same range as those to substitutional Xe an annealing step to 1200 K was introduced after the Xe bombardment to remove sub-surface Xe. The A, B and C peaks are substantially smaller after the Xe bombardment.

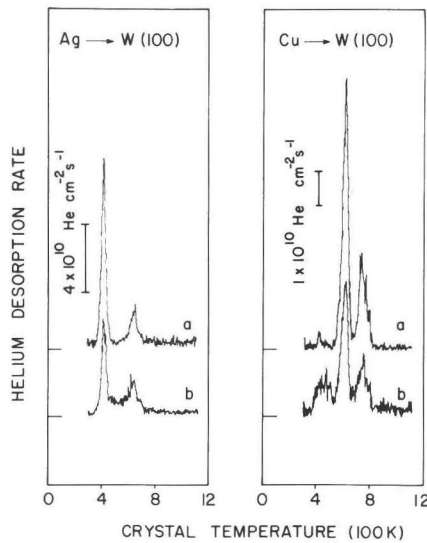


fig. 3: Helium desorption spectra of W(100): (a) bombarded with  $2 \times 10^{12}$  5 keV  $\text{Ag}^+$  or  $\text{Cu}^+$   $\text{cm}^{-2}$ , heated to 1780 K and injected with  $3 \times 10^{12}$  250 eV  $\text{He}^+$   $\text{cm}^{-2}$ , (b) as (a) but now prior to the He injection bombarded with  $2.2 \times 10^{15}$  250 eV  $\text{Xe}^+$   $\text{cm}^{-2}$  (Ag) or  $2.6 \times 10^{15}$  250 eV  $\text{Xe}^+$   $\text{cm}^{-2}$  (Cu) followed by heating to 1200 K.

Heating to 1700 K caused no further reduction of the A, B and C peaks. In fig. 4 the logarithmic decrease of the A peak as a function of the Xe dose is shown for Ag and Cu in W. With a least squares fit  $\mu_i$  was derived to be  $3 \times 10^{-16} \text{ cm}^2$ . For Ar and Al the same  $\mu_i$  was found.

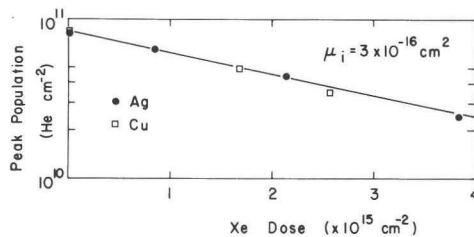


fig. 4: The A peak population as a function of the He dose for Ag (●) and Cu (□) in W(100). Bombardment parameters as in fig. 3. The line is a least squares fit to the Ag data.

The value is lower than found for reaction 1. Loss of substitutional impurities by sputtering cannot explain the large observed decrease. The Xe dose, at which the population of the A,B and C peaks is reduced with a factor 2, corresponds with sputtering of a layer with a thickness of at maximum 2 Å. The average penetration depth, as calculated with Marlowe, for 5 keV Ag implanted into W(100) at angles of 10 and 20 degrees with respect to the surface normal is 65 Å respectively 20 Å. The annealing up to 1800 K after the Ag bombardment leads to limited Ag diffusion, so that the average Ag depth is even larger than the calculated minimum value of 20 Å. The other implants are located deeper than Ag. Therefore it is clearly demonstrated that the decrease of the A, B and C peaks observed for all implants cannot be caused by sputtering, and must therefore be caused by interaction of the SIAs with the implants.

#### 4.2.3. DISCUSSION.

Different defect configurations may have formed by the observed reaction of the SIAs with the impurity atoms. The formation of a SIA bound to the impurity atom can be excluded since heating to 1700 K would lead to the release of the SIA and the subsequent visibility of the impurity atoms, contrary to the observed behaviour. Van Veen et al. [7,8] observed that substitutional Ar and Kr were converted by the SIAs into interstitials, thereby becoming mobile already at or slightly beyond room temperature.

This conversion may also have taken place with the metallic implants studied here. However, we cannot exclude the formation of mixed dumbbells in this study. The stability of mixed dumbbells is calculated by Dederichs et al. [1] using Morse potentials. For relatively small impurities a high stability is observed. Cage motion, i.e. motion of the dumbbell so that it is confined within a unit cell [16], requires an energy about equal to the SIA migration energy. Rotation of a dumbbell requires some 4 to 7 times the pure SIA migration energy [1]. The latter motion allows the impurity to diffuse. Dissociation of the dumbbell requires a higher energy. Experimental evidence on the stability of mixed dumbbells follows from ref. [5]; Co-Mo <110> dumbbells in Mo are stable up to stage III temperature, at this temperature they disappear probably by annihilation with migrating vacancies. Since Co is much smaller than Mo this high stability is

expected. Other information on the energy required for rotation of the dumbbells follows from recent calculations of Johnson [17]. He predicts that the energy required for rotation of a  $\langle 110 \rangle$  dumbbell to the  $\langle 111 \rangle$  orientation is between 0.4 and 1.2 eV depending on the chosen pair-potential. Therefore we expect that after annealing to 1200 K, as done in our experiment after the SIA production, mixed dumbbells will have been able to rotate and thus diffuse. Since the surface is nearby the impurities will have been trapped there.

The pushing out of an impurity atom by a SIA can attribute to radiation enhanced diffusion observed during ion beam mixing. For certain combinations of atoms it is seen that the impurity atoms are trapped in layers deeper than the initial range [17]. Apparently the impurity atom has become mobile. The relative stability of the impurity-SIA complex will be an important parameter for the efficiency of the mixing process.

The coefficient for SIA capture  $\mu_i$ , found in this study for both HeV and ArV defects in W(100), is lower than found in [8] for those defects in Mo(110). This may be due partly to a lower efficiency for SIA production at the (100) surface, than for (110). However, we cannot exclude that in this study considerable divergence of the Xe beam has occurred between the last diaphragm and the target under influence of space charge, yielding a systematic overestimate of the Xe dose  $\text{cm}^{-2}$ .

The conclusions of this study are:

- SIAs react with the impurities Ar, Ag, Cu and Al in W.
- The capture cross section is of the same order of magnitude as that for SIA capture by HeVs.
- The then formed defect is either a mixed dumbbell or an impurity at a purely interstitial position.
- Heating to 1700 K does not lead to substitutionality of the implants again, indicating that the impurity atoms have diffused interstitially to the surface.

This work was part of the research programme of the Stichting voor Fundamenteel Onderzoek der Materie (Foundation for Fundamental Research on Matter) and was made possible by financial support of the Nederlandse Organisatie voor Zuiver Wetenschappelijk Onderzoek (Netherlands Organization for the Advancement of Pure Research).



## REFERENCES

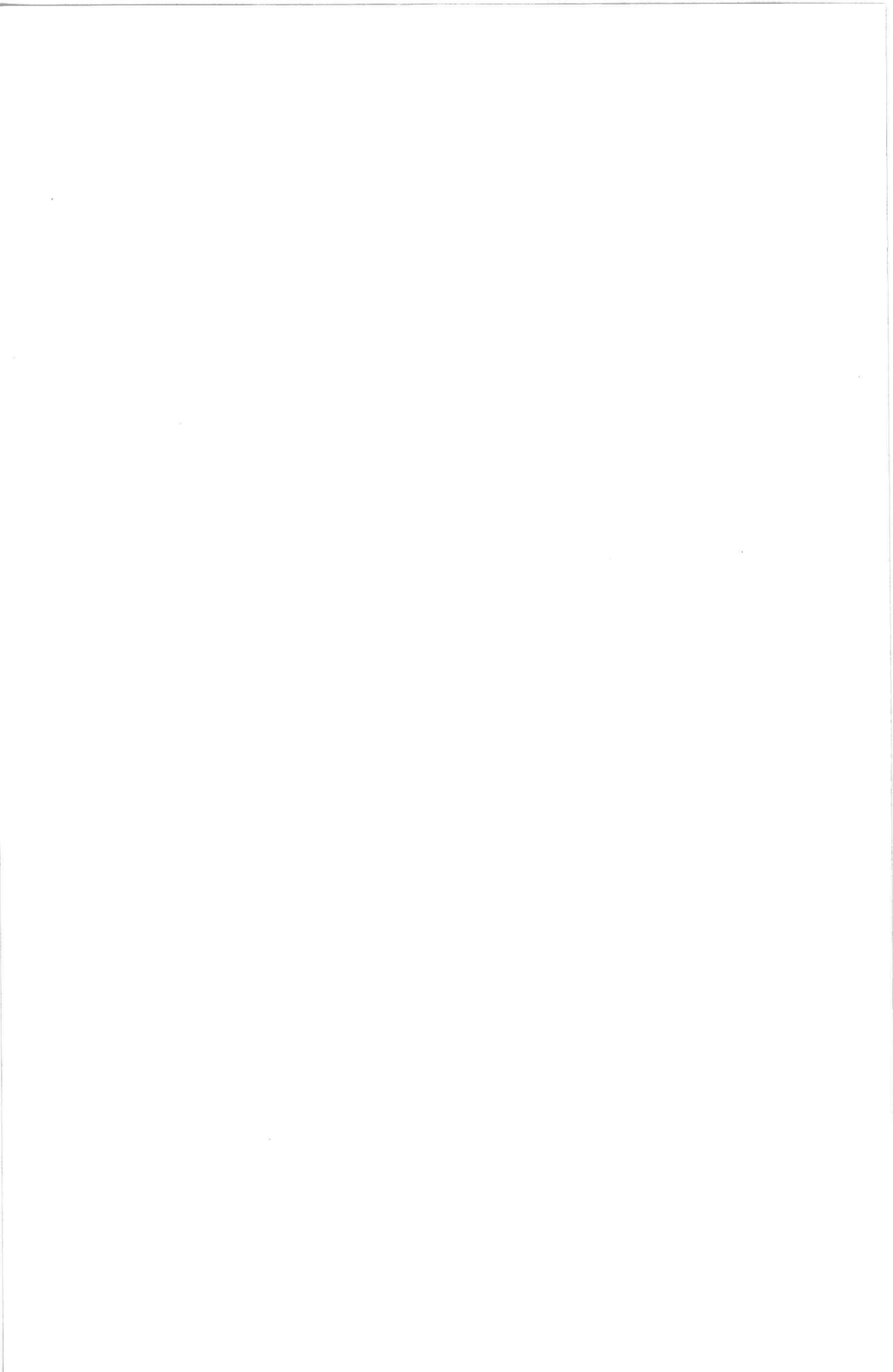
- [ 1 ] P.H. Dederichs, C. Lehmann, H.R. Schober, A. Scholz and R. Zeller, J. of Nucl. Mat. 69/70,176(1978).
- [ 2 ] M.L. Swanson, L.M. Howe and A.F. Quenneville, J. of Nucl. Mat. 69/70, 372(1978).
- [ 3 ] H. Wollenberger, J. of Nucl. Mat. 69/70,362(1978).
- [ 4 ] A. Marwick, to be published in Nucl. Instr. and Meth. 1984.
- [ 5 ] W. Mansel, J. Marangos and D. Wahl, J. of Nucl. Mat. 108/109,137(1982).
- [ 6 ] K.H. Ecker, J. of Nucl. Mat. 119,301(1983).
- [ 7 ] A. van Veen, W.Th.M. Buters, G.J. van der Kolk, L.M. Caspers and T.R. Armstrong, Nucl. Instr. and Meth. 194,485(1982).
- [ 8 ] A. van Veen, W.Th.M. Buters, T.R. Armstrong, B. Nielsen K.T. Westerduin, L.M. Caspers and J.Th.M. de Hosson, Nucl. Instr. and Meth. 209/210,1055(1983).
- [ 9 ] J.A. Venables and R.W. Baluffi, Phil. Mag. 11,1021(1965).
- [ 10 ] C. Erginsoy, G.H. Vineyard, A. Englert, Phys. Rev. A 133,595(1964).
- [ 11 ] V.G. Kapinos, YU.R. Kevorkyan, Rad. Eff. 79,9(1983).
- [ 12 ] A. van Veen, G.J. van der Kolk, H.A. Filius, K.T. Westerduin and L.M. Caspers, to be published in Nucl. Instr. and Meth. 1984.
- [ 13 ] G.J. van der Kolk, A. van Veen, L.M. Caspers and J.Th.M. de Hosson, Rad. Eff. 71,109(1983).
- [ 14 ] G.J. van der Kolk, K. Post, A. van Veen, F. Pleiter and J.Th.M. de Hosson, to be publ. in Rad. Eff, chapter 3.3.
- [ 15 ] G. Carter and J.S. Colligon, Ion Bombardment of Solids, Heinemann London 1968.
- [ 16 ] G.Vogl, W. Mansel and P.H. Dederichs, Phys. Rev. Lett. 36,1497(1976).
- [ 17 ] R.A. Johnson, Phys. Rev. B 27,2014(1983).
- [ 18 ] Z.L. Wang, J.F.M. Westendorp and F.W. Saris, Nucl. Instr. and Meth. 209/210,115(1983).



## 5. INTERACTION BETWEEN IMPLANTED IMPURITIES.

### INTRODUCTORY REMARKS.

In this chapter experiments are described, in which the implantation doses of the metallic impurities exceeded  $10^{13}$  per  $\text{cm}^2$ . From previous work it is known that for heavy noble gas implants substantial clustering effects are seen at such doses. For the metallic impurities only for Ag substantial clustering effects were seen. It is argued that this indeed indicates that the other metallic impurities implanted by us, Al, Cr, Cu and Mn, do not cluster at the implantation doses mentioned above.



## CLUSTERING PHENOMENA OF IMPLANTS IN TUNGSTEN OBSERVED WITH THDS.

G.J. van der Kolk<sup>1</sup>, A. van Veen<sup>1</sup>, J.Th.M. de Hosson<sup>2</sup> and L.M. Caspers<sup>1</sup>.

<sup>1</sup> Delft University of Technology/Interuniversity Reactor Institute Delft, Mekelweg 15, 2629 JB Delft, the Netherlands.

<sup>2</sup> University of Groningen, Materials Science Centre, Nijenborgh 18, 9747 AG Groningen, the Netherlands.

### ABSTRACT

A W(100) single crystal was irradiated with 5-10 keV of different metallic species (Ag, Cu, Cr, Mn, Al and In). Subsequently the crystal was annealed at temperatures ranging from room temperature to 2400 K. Thermal Helium Desorption Spectrometry (THDS) was applied to monitor the dissociation and clustering reactions of defect complexes either formed at room temperature during implantation or during partial annealing at a higher temperature. Strong evidence is found for clustering of Ag if implantation doses of Ag exceed  $6 \times 10^{12} \text{ Ag}^+ \text{ cm}^{-2}$ . For the implants Al, Cr, Cu and Mn substantial clustering was not detected. Atomistic calculations are presented which indicate that clustering of the implants other than Ag certainly would be detected if the impurity atoms in the cluster all occupy lattice positions. Therefore we do believe that radiation enhanced diffusion is much more efficient for Ag than for Cu and Mn in W. For Cr and Al we cannot exclude enhanced diffusion, since the binding energies of Cr and Al to Cr-respectively Al-clusters in W will be rather small. Of the implants Cu, Mn and Ag, the latter is the only one being oversized. A rather strong binding of vacancies to Ag is envisaged, which enables transport of the Ag atom, being part of a moving vacancy cluster.

### 5.1. INTRODUCTION.

In studies, in which ion implantation is used to obtain mixed surface layers, radiation enhanced diffusion plays an important role in determining the efficiency of the mixing process. Ion irradiation induced defect fluxes not only affect the efficiency of the process but also

may lead to radiation induced segregation [1,2,3]. The latter phenomenon is made possible by the first. It may lead to undesirable effects like demixing of alloys or surface enrichment by one of the alloying components as a consequence of irradiation [4]. The temperature range where enhanced diffusion is favoured is an intermediate region in which vacancies are mobile and where the equilibrium concentration of vacancies is not very high. The excess vacancies present during the implantation may provide a transport mechanism for larger solutes. For smaller solutes in general an interstitial migration mechanism is assumed [1]. A phenomenon, closely related to radiation enhanced diffusion is clustering. After 5 keV implantation of Kr into W and annealing to 1500 K clustering was observed with thermal helium desorption spectrometry (THDS) [5]. It was shown that the Kr atoms were transported along with the radiation produced vacancies.

In this study THDS is applied to study the initial phase of segregation of metallic implants on an atomic level. Essentially THDS is the decoration of defects with low energy implanted helium. The rapid interstitial diffusion of He through the crystal provides trapping of a fraction of the implanted He atoms at different defects. Due to different binding energies the various defects can be distinguished by monitoring the He release rate as a function of the temperature. Binding of He to substitutional impurities gives rise to unique desorption peaks, for a review see refs. [6,7,8]. The desorption temperature is shifted upwards if more impurity atoms are located close to each other on lattice positions. This provides a unique tool to study radiation induced segregation in the very early stage when only two or three solute atoms have clustered. The results presented in this paper are an extension of earlier published results on Kr clustering [5] and Ag-clustering in W [9].

In section 2 the experimental results are presented, in section 3 static lattice calculations are presented which facilitate assignment of the different desorption peaks. In section 4 the defect assignments will be made and discussed.

## 5.2. EXPERIMENTAL RESULTS.

### 5.2.1. Experimentally.

The experimental equipment has already been described in refs. [5] and [10]. The sample is the same W(100) single crystal used in earlier experiments. The sample is mounted in a large vacuum chamber on a rotatable platform such that the sample can face: a metal ion source (5-30 keV); a gas ion source (0.1-6 keV); and a quadrupole mass spectrometer. The gas ion beam (He beam) traverses a Wien filter. The high purity of the He gas used ensures that the fraction of impurity ions in the He beam is less than  $10^{-4}$ . The impurity ion beam is mass analysed by a magnetic separator ( $M/\Delta M \sim 200$ ). Both beams are swept periodically (700 and 2500 Hz) by horizontal and vertical pairs of deflection plates to ensure a uniform distribution on the target. Computer controlled heating by electron bombardment on the rear of the target ensures linear heating with time during desorption or partial annealing. The temperature is obtained from a WRe3%-WRe25% thermocouple. The annealing scheme used in this study consisted of linear heating with time (heating rate  $\beta=40$  K/s) to a certain temperature followed by cooling. In general this leads to recovery steps at higher temperatures than seen with isochronal annealing procedures.

### 5.2.2. Results.

Ag dose variation In fig. 1 a series of desorption spectra is shown of W(100), implanted with an increasing dose of 10 keV  $\text{Ag}^+$ , heated to 1600 K and subsequently injected at room temperature with  $1.3 \times 10^{12}$  250 eV  $\text{He}^+$   $\text{cm}^{-2}$ . The spectra are similar to those earlier shown [9], except for the appearance of a peak at low desorption temperature. A lower He dose is chosen than in [9] to facilitate a better peak separation. The average degree of filling amounts to about 0.3 He per trap. In ref. [11] it was shown that the peaks labelled A and B represent dissociation of one respectively two He atoms from a substitutional Ag atom (notation  $\text{AgV}$ ). Extra peaks, labelled P, Q and R, are seen to evolve with increasing Ag dose. The P and Q peaks resemble the peaks seen earlier for high dose Kr bombardment on W [5], therefore the same notation was used. The different peaks, peak temperatures and dissociation energies for the indicated pre-exponential factors  $\nu_0$  are

shown in table 1.

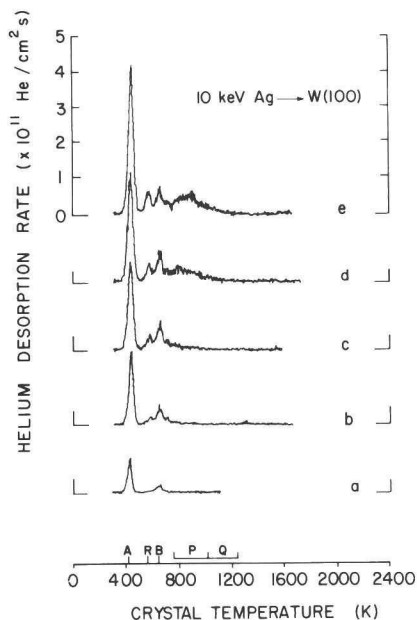


fig. 1: Spectra of W(100), bombarded with 10 keV  $\text{Ag}^+$ , heated to 1600 K and injected with  $1.2 \times 10^{12}$  250 eV  $\text{He}^+$   $\text{cm}^{-2}$ , Ag doses were: a)  $2 \times 10^{12}$   $\text{cm}^{-2}$ ; b)  $4 \times 10^{12}$   $\text{cm}^{-2}$ ; c)  $7 \times 10^{12}$   $\text{cm}^{-2}$ ; d)  $2.1 \times 10^{13}$   $\text{cm}^{-2}$ ; e)  $4 \times 10^{13}$   $\text{cm}^{-2}$ .

table 1: Peak assignments and dissociation parameters for Ag implanted W (heating rate 40 K/s).

peak	temp. (K)	$E_d$ (eV)	$\nu_0$ $\text{s}^{-1}$	reaction
A	430	1.03	$3 \times 10^{12}$	$\text{HeAgV} \rightarrow \text{He} + \text{AgV}$
B	650	1.57	$3 \times 10^{12}$	$\text{He}_2\text{AgV} \rightarrow 2\text{He} + \text{AgV}$
R	580	1.40	$3 \times 10^{12}$	
P	760-1000	1.9-2.5	$3 \times 10^{12}$	$\text{HeAg}_n\text{V}_n \rightarrow \text{He} + \text{Ag}_n\text{V}_n$ $n=2,3$
Q	1000-1260	2.5-3.1	$3 \times 10^{12}$	
H <sub>b</sub>	1390	3.6	$1 \times 10^{13}$	$\text{HeAg}_n\text{V}_{n+1} \rightarrow \text{He} + \text{Ag}_n\text{V}_{n+1}$
H	1490	4.5	$2 \times 10^{15}$	$\text{HeV} \rightarrow \text{He} + \text{V}$



It should be noted that the P and Q peaks are too broad to represent only one binding state; no proper fit could be made. Therefore all He desorbing between 760 K and 1000 K was taken as P peak population, and He desorbing above 1000 K but below 1200 K was taken as Q peak population. The peak assignments shown in the table will be discussed in the next section. The peak populations as a function of the Ag dose are shown in fig. 2.

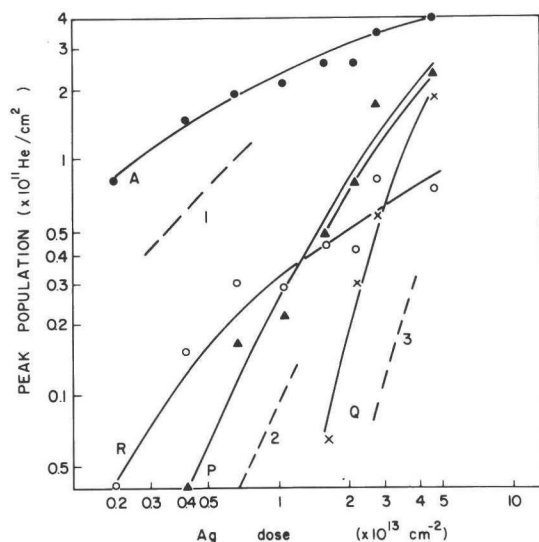


fig. 2: Peak populations as a function of Ag dose, bombardment parameters as in fig. 1.

Influence of other defects Implantation with  $1.6 \times 10^{13}$  10 keV  $\text{In}^+$   $\text{cm}^{-2}$ , heating to 1600 K, and injection with 250 eV  $\text{He}^+$  revealed no desorption peaks at all. From this we conclude that the P, Q and R peaks seen in the case of Ag implantation are associated with Ag. Location of Ag near implantation-produced defects may be responsible for the enhanced He binding. A Ag atom next to a dislocation loop will bind He stronger than a Ag atom in a perfect lattice. To investigate this the target was bombarded with a very high dose of 20 keV  $\text{W}^+$  ions to create dislocation loops and vacancy clusters. Subsequently a low dose  $\text{Ag}^+$  was injected. Finally again a bombardment with a high dose of  $\text{W}^+$  was performed. Finally the crystal was heated to 1600 K. This "sandwich" bombardment ensures, whether the Ag atoms or the other defects are the mobile species, that the fraction of Ag located near other defects will be of the same order of magnitude as in the case of

high dose Ag bombardment only. The spectrum is shown in fig. 3. For comparison a spectrum with a high dose Ag only is also shown.

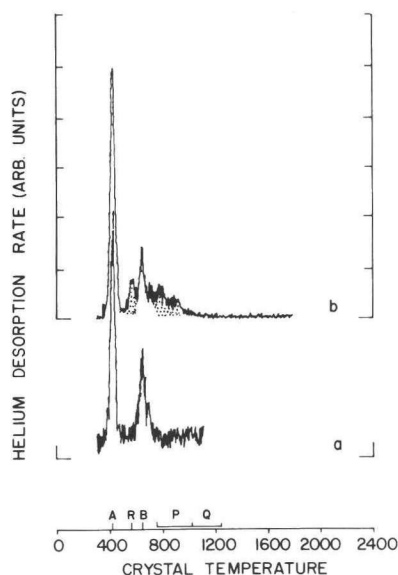


fig. 3: W(100), after bombardment heated to 1600 K and injected with  $1.3 \times 10^{12}$  250 eV  $\text{He}^+$   $\text{cm}^{-2}$ , shaded area's indicate high dose effects. Initial bombardments: a)  $1.7 \times 10^{13}$  20 keV  $\text{W}^+$   $\text{cm}^{-2}$ , followed by  $1 \times 10^{12}$  10 keV  $\text{Ag}^+$   $\text{cm}^{-2}$  followed by  $1.6 \times 10^{13}$  10 keV  $\text{W}^+$   $\text{cm}^{-2}$ ; b)  $1.6 \times 10^{13}$  10 keV  $\text{Ag}^+$   $\text{cm}^{-2}$ .

It is quite clear that P, Q and R peaks are not visible in the case of pre- and post-irradiation with W ions.

Annealing behaviour of high dose  $\text{Ag}^+$  implanted W In fig. 4 a series of spectra is shown of W(100), bombarded with  $1.6 \times 10^{13}$  10 keV  $\text{Ag}^+$   $\text{cm}^{-2}$ , annealed to the indicated temperatures and subsequently injected at room temperature with  $3 \times 10^{12}$  250 eV  $\text{He}^+$   $\text{cm}^{-2}$ . The peak labelled H represents He desorption from vacancy type defects. Apparently the peak shown here after annealing to temperatures beyond stage III temperature (in our annealing scheme 900 K) originates from He trapped in bound vacancies, since free vacancies do not survive this annealing temperature. The peak is labelled  $\text{H}_b$ . The vacancies can be bound to vacancy clusters or to Ag clusters.

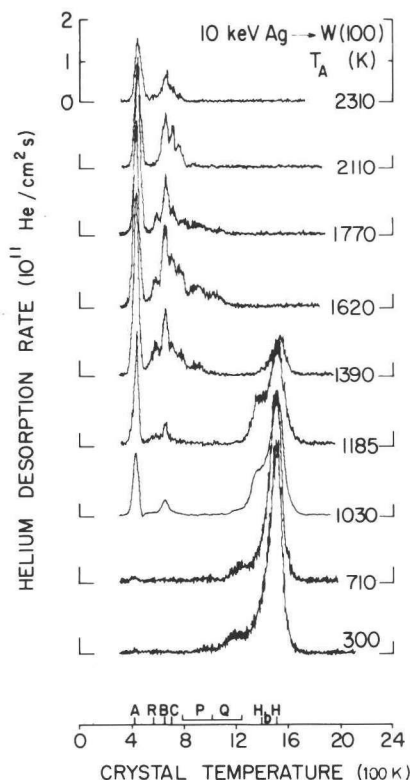


fig. 4: W(100) bombarded with  $1.6 \times 10^{13} \text{ 10 keV Ag}^+ \text{ cm}^{-2}$ , heated to the indicated temperatures and injected with  $3 \times 10^{12} \text{ 250 eV He}^+ \text{ cm}^{-2}$ .

In fig. 5 peak populations as a function of the annealing temperature are shown. The following observations can be made:

- i After annealing to stage III (900 K) the H peak has decreased, monovacancies have become mobile and have disappeared at the near surface.
- ii The A, B and C peaks become visible at about 900 K.
- iii Above 700 K a peak denoted  $H_b$  becomes visible.

The disappearance of peak  $H_b$  at 1350 K is accompanied with the appearance of the P and Q peaks.

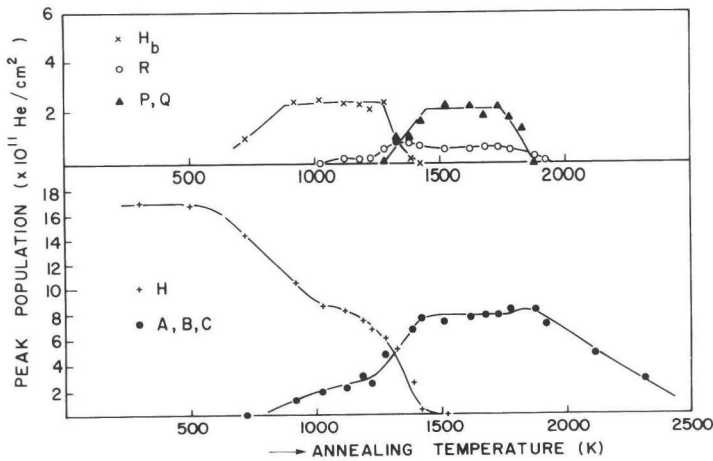


fig. 5: Peak populations as a function of the annealing temperature, bombardment parameters as in fig. 4.

- iv Above 1800 K the P, Q and R peaks disappear in a narrow temperature interval.
- v Above 1800 K the A, B and C peaks gradually disappear apparently due to thermal vacancy assisted diffusion of the Ag atoms to the surface followed by desorption [11,12].

He dose variation after high dose Ag<sup>+</sup> implantation The He dose was varied for the W target implanted with  $5.3 \times 10^{13}$  10 keV Ag<sup>+</sup> cm<sup>-2</sup> and annealed to 1800 K. The spectra are shown in fig. 6. It is quite clear that the average desorption temperature of the peaks, evolving after high dose Ag implantation, increases with increasing He dose.

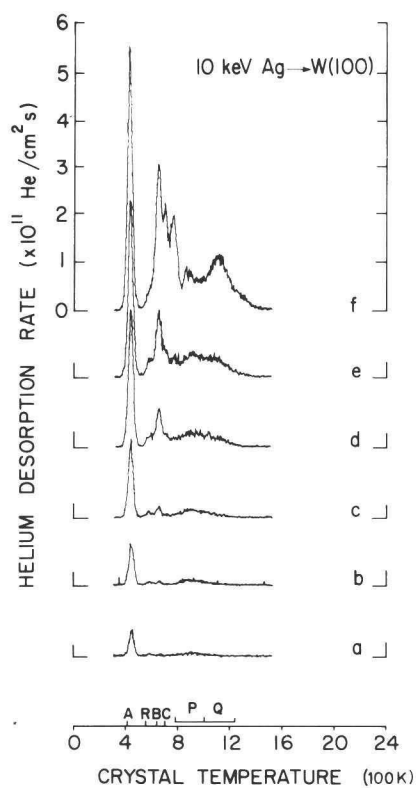


fig. 6: W(100) bombarded with  $5.3 \times 10^{13}$  10 keV  $\text{Ag}^+ \text{ cm}^{-2}$ , heated to 1800 K and injected with various He doses, He doses were: a)  $2 \times 10^{11} \text{ cm}^{-2}$ ; b)  $4.3 \times 10^{11} \text{ cm}^{-2}$ ; c)  $8.6 \times 10^{11} \text{ cm}^{-2}$ ; d)  $2 \times 10^{12} \text{ cm}^{-2}$ ; e)  $3 \times 10^{12} \text{ cm}^{-2}$ ; f)  $6 \times 10^{12} \text{ cm}^{-2}$ .

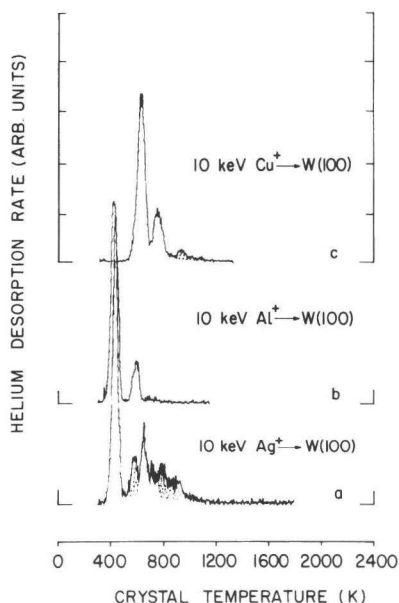


fig. 7a: W(100) bombarded, heated to 1600 K and injected with  $1.3 \times 10^{12}$  250 eV He<sup>+</sup> cm<sup>-2</sup>, shaded area's indicate high dose effects. Initial bombardments:  
 a)  $1.6 \times 10^{13}$  10 keV Ag<sup>+</sup> cm<sup>-2</sup>;  
 b)  $4 \times 10^{13}$  10 keV Al<sup>+</sup> cm<sup>-2</sup>;  
 c)  $4 \times 10^{13}$  10 keV Cu<sup>+</sup> cm<sup>-2</sup>.

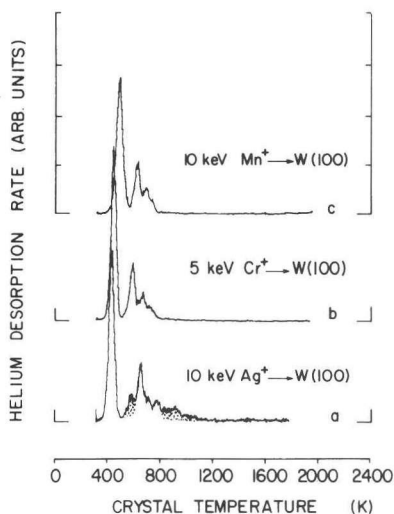


fig. 7b: As fig. 7a but now with initial bombardments:  
 a)  $1.3 \times 10^{13}$  10 keV Ag<sup>+</sup> cm<sup>-2</sup>;  
 b)  $2 \times 10^{13}$  5 keV Cr<sup>+</sup> cm<sup>-2</sup>;  
 c)  $2.6 \times 10^{13}$  10 keV Mn<sup>+</sup> cm<sup>-2</sup>.

High doses of Cu<sup>+</sup>, Al<sup>+</sup>, Mn<sup>+</sup> and Cr<sup>+</sup> In fig. 7 spectra, taken after high dose impurity bombardment and annealing to 1600 K, are shown for the various other implants. Spectra for In implantation are not shown, since In in W does not bind He at all. Quite evidently the characteristic P, Q and R peaks are not visible for the implants other than Ag. However in the case of Cu<sup>+</sup> implantation a very small peak is visible at 950 K which should not be there at the low He filling degree of the defects.

### 5.3. STATIC LATTICE CALCULATIONS.

Static lattice calculations were performed for various impurity clusters to obtain an estimate of the binding energies of He. The

pair-potential set was the same as used in [11]. The W-W potential was derived from elastic constants [13], the He-metal pair potentials were derived with a Hartree-Fock-Slater scheme [14,15]. The W-impurity and impurity-impurity potentials were obtained by application of a scaling procedure to the W-W potentials [11]. The size of the crystallite in the calculations is  $17 \times 17 \times 17$  lattice units.

From the calculations binding energies were obtained. The dissociation energy equals the binding plus migration energy, therefore 0.25 eV was added to all calculated binding energies to obtain the dissociation energies.

table 2: Calculated dissociation energies  $E^d$  for He from various defects.  
Figures between brackets indicate  $n^{\text{th}}$  neighbour positions.

defect	$E^d$ (eV) calc.	$E^d$ (eV) exp.
AgV	1.00	1.03
Ag <sub>2</sub> V <sub>2</sub> (1)	1.58	
Ag <sub>2</sub> V <sub>2</sub> (2)	1.72	1.48
Ag <sub>3</sub> V <sub>3</sub> (112)	2.29	
CuV	1.76	
Cu <sub>2</sub> V <sub>2</sub> (1)	2.26	
Cu <sub>2</sub> V <sub>2</sub> (2)	2.97	1.13
MnV	1.17	
Mn <sub>2</sub> V <sub>2</sub> (1)	1.31	
Mn <sub>2</sub> V <sub>2</sub> (2)	2.11	
CrV	1.25	1.02
Cr <sub>2</sub> V <sub>2</sub> (1)	1.33	
Cr <sub>2</sub> V <sub>2</sub> (2)	2.09	0.99
AlV	1.21	
Al <sub>2</sub> V <sub>2</sub> (1)	1.48	
Al <sub>2</sub> V <sub>2</sub> (2)	1.99	

In table 2 results are shown for the substitutional implants as well as for the small clusters. The number between brackets indicates a substitutional impurity at  $n^{\text{th}}$  neighbour separation. The configuration of a di-atomic impurity cluster which yielded the largest He dissociation energy was the second nearest neighbour cluster. Impurity atoms at  $n^{\text{th}}$  neighbour distance with  $n > 2$  affect the binding energies only slightly. For the tri-atomic clusters surrounding of the He atom leads to the highest binding energy. To illustrate the accuracy of the calculations, we show in table 2 the experimental dissociation energies for He from substitutional implants taken from [11].

## 5.4. DISCUSSION.

### 5.4.1. Ag results.

The P, Q and R peaks were seen to evolve at higher Ag doses only. For the other implants no P and Q peaks were seen. Since for high dose In implantation He binding was not observed at all, whereas the cascades produced by In and Ag are similar, we believe that the P and Q peaks have to do with He associated with Ag (similarly as for Kr). Other evidence is that after Kr bombardment a P peak was observed at a higher desorption temperature than for Ag for a similar He dose [5]. There are various arguments which support the assignment of these peaks to Ag clusters as well as undermining this assignment. The following arguments undermine the clustering hypothesis:

- After implantation of a W foil with 25 keV  $^{111}\text{Ag}^+$  to a dose of  $2 \times 10^{13} \text{ cm}^{-2}$  and isochronal annealing at 1200 K, observations with perturbed angular correlation measurements (PAC) did not reveal sizable contributions to the PAC spectra with hyperfine parameters as would be expected for di-atomic Ag clusters [16].

- Only the R peak is a clear first order desorption peak, the P and Q peaks are in fact conglomerates of (probably first order) desorption peaks with slightly different desorption temperatures.

Arguments which support the clustering hypothesis are:

- No P, Q and R peaks could be grown in the W target by bombardment with a high dose 20 keV  $\text{W}^+$ , followed by a low dose 10 keV  $\text{Ag}^+$  and again bombarded with a high dose 10 keV  $\text{W}^+$ .

- In the case of 10 keV  $\text{Ag}^+$  bombardment, conversion of vacancy type peaks into P and Q peaks takes place at a considerably lower annealing temperature than in the case of 5 keV  $\text{Kr}^+$  bombardment. The higher implantation energy of Ag will lead to larger defect clusters, so the weaker vacancy binding is caused by a weaker interaction of the vacancies with the implanted atoms, i.e. Ag-atoms. The strong vacancy binding observed in both cases is not expected for single substitutional impurities.

- The P, Q and R peaks are seen already at an implantation energy of 5 keV, this implantation energy is too low to expect large defect clusters to have formed. Small defect clusters may have formed, but we do not expect that these are stable up to 1800 K.

- The peak evolution of the P, Q and R peaks is for the P and R peaks



approximately quadratic with the Ag dose, whereas for the Q complex a higher order increase is seen as a function of the Ag dose, see fig. 2. Especially the latter observation supports the clustering hypothesis since it is hard to see why a third order term would persist for Ag interaction with other defects as a function of the bombardment dose.

A unique assignment of the P, Q and R peaks is not possible. Based on the above arguments, however, we believe that the P and Q peaks represent binding of He to small Ag clusters. The R peak will not necessarily indicate clustering; it only grows quadratically with Ag dose for low doses, at higher doses a saturation occurs, see fig. 2. Maybe Ag clusters in near surface regions give rise to this peak. It should be noted that for Kr the R peak was not observed [5]. Since the He filling degree in these experiments was rather high, it cannot be excluded that the R peak was hidden underneath the B and C peaks.

The calculated binding energies also do not permit a definite assignment of the P, Q and R peaks. The computed dissociation energy of He to, what is expected to be the most stable di-atomic Ag-cluster, a  $\text{Ag}_2\text{V}_2$ , is well in between the two experimental values of the R and P peak. All experimental values however are well in the range of what is computed for small Ag-clusters.

Assuming that the P and Q peaks represent clustering the annealing results are explained as follows: vacancy type defects are visible up to 1400 K, however the largest fraction has disappeared after annealing to 1100 K. The fraction still visible will be due to bound vacancies and to more stable vacancy clusters. At 1300 K the peak labelled  $\text{H}_b$  disappears accompanied with a growth of the P and Q peaks. Since the maximum peak temperature of  $\text{H}_b$  is lower than that of the pure H peak after low dose implantation, we believe that dissociation of He from vacancy type defects slightly "smaller" than monovacancies is concerned here. Ag is oversized in W, so a vacancy bound by a Ag-cluster will indeed be "smaller". Note that in ref. [16] a binding energy of a vacancy to a substitutional Ag-atom in W was found of 0.5 eV. For two atoms a binding energy approximately two times larger is expected. This would result in a dissociation energy of 2.7 eV. The recovery step at 1300 K corresponds with about 3.5 eV. In the earlier Kr clustering experiments vacancy type defects persisted up to much higher annealing temperatures. This is quite understandable regarding

the much larger binding energy of a vacancy to a KrV than to a AgV in tungsten. A  $Kr_2V_3$  will similarly be more stable than a  $Ag_2V_3$ .

The P, Q and R peaks disappear at about 1800 K. This corresponds with the onset of self-diffusion via a thermal vacancy mechanism. So the Ag clusters break up, essentially this requires only one step versus many for migration to the surface. Indeed it is observed that the decrease of the P, Q and R peaks is rather sudden.

#### 5.4.2. Other metallic implants.

The small peak visible after high dose Cu injection at 950 K in fig. 6 (corresponding for  $\nu_0 = 3 \times 10^{12} \text{ s}^{-1}$  with  $E^d = 2.3 \text{ eV}$ ) agrees with the dissociation energy of 2.26 eV, calculated for He dissociation from a  $Cu_2V_2$ . Therefore we assume that this peak indicates Cu clustering. For the other implants, Cr, Al and Mn, no clustering peaks were observed. We cannot exclude, however, that a peak of the same magnitude of the cluster peak in the case of Cu is hidden underneath the B and C peak. The calculations predict an enhancement of the binding energy of only 0.1 to 0.3 eV for the smallest clusters. Quite evidently for all these implants the degree of clustering is far below that of Ag in W.

#### 5.4.3. Mobility and clustering mechanism.

According to Miedema et al. [17] Ag, Cu and Mn have a positive heat of solution in liquid W. The binding energy between two solute atoms is proportional to the reduction of the contact area implant-host. Neglecting contributions due to size-mismatch and taking the reduction 1/8 for a di-atomic cluster with respect to two isolated atoms, the following data were obtained for the binding energy: for Ag 0.21 eV, for Cu 0.11 eV and for Mn 0.03 eV.

Transport of the solute atoms can occur through two mechanisms: (i) The substitutional implants are converted to interstitial positions by interaction with irradiation produced self-interstitials [18]. Once in interstitial position diffusion may occur quite easily. A large fraction of these interstitials however, will be trapped by nearby vacancies of its own cascade. Those interstitials escaping their cascade, will still have a rather small probability of encountering another implant, since these are effectively shielded by vacancies as well; (ii) the substitutional implants bind one or more

vacancies, the whole complex migrates thermally activated.

Since the appearance of the P and Q peaks coincides with the disappearance of the vacancy-type peak  $H_b$ , we assume that indeed the latter mechanism is responsible for the observed clustering. The first mechanism may play an additional role in the transportation of impurity atoms to the cascade regions of other implanted atoms.

The binding energy of a vacancy to Ag in W was recently measured; and is 0.5 eV [16]. Adopting "Miedema type" arguments we expect that the vacancy binding energy is related to the positive heat of solution and the relative oversize of the impurity atom [19]. After correction for volume contraction due to charge transfer, similarly as in [11], Ag is the only oversized implant of the impurities studied here. Furthermore it has the highest heat of solution. Therefore we expect that the vacancy binding energy to the other impurities is well below the experimental value found for Ag. Consequently, the mobility of the other implants will be smaller than that of Ag.

Observing fig. 7 we notice that already at Ag doses of  $6 \times 10^{12} \text{ Ag}^+ \text{ cm}^{-2}$  clustering is visible. From the model given by van Gorkum et al. [20] it is deduced that the probability  $p_c$ , that an implanted atom encounters another implanted atom, is approximately:

$$p_c = 4\pi r_i \bar{d}_i c_i f_m \quad (1)$$

$r_i$  is the trapping radius for implants, for noble gas atoms  $r_i$  is typically 3 Å,  $\bar{d}_i$  is the average penetration depth of the implant,  $c_i$  the concentration per surface area and  $f_m$  a factor which indicates the fraction of the implants which is sufficiently long associated with a vacancy to facilitate long range transport. A rough guess of the latter follows from the desorption data of Kornelsen et al. [21] of 5 keV Kr implanted into W(100). Only some 10% of the Kr atoms has desorbed from the crystal after heating to 1600 K (heating rate 40 K/s). A large fraction is due to desorption of near-surface Kr. An upper limit of  $f_m$  for implantation energies of about 5 keV will therefore be 0.05.

Average penetration depths calculated with Marlowe of 10 keV Ag implanted into W(100) at implantation angles of 10 respectively 20 degrees off the surface normal are respectively 125 Å and 30 Å. Therefore we expect from eq. (1) that for a Ag dose of  $1 \times 10^{13} \text{ cm}^{-2}$  a frac-

tion of between 6% and 24% has clustered. Indeed for a Ag dose of  $1 \times 10^{13} \text{ cm}^{-2}$  10% of the trapped He atoms desorbs in the P and Q peaks.

## 5.5. CONCLUSIONS.

- After bombardment with doses above  $6 \times 10^{12} \text{ 10 keV Ag}^+ \text{ cm}^{-2}$  and annealing to 1200 K extra peaks were seen in the desorption spectra, which were attributed to He desorbing from small  $\text{Ag}_n\text{V}_n$  clusters, with  $n=2,3,\dots$ . The peaks disappeared after annealing to 1800 K, the decrease is rather abrupt, indicating that only one step is needed for the cluster to break up. The appearance of the cluster peaks is accompanied with the disappearance of a vacancy type peak  $\text{H}_p$ . He desorbing from a vacancy, bound by a small Ag cluster, causes this peak. It indicates that the Ag clusters form through excess vacancies.

- The P and Q peaks are too broad for first order desorption peaks. This could be caused by a variety of defects with slightly different binding energies for He, such as location of the clusters near other defects, near the surface, or various cluster configurations.

- For the other implants Cu, Mn Al and Cr no substantial clustering was observed. Both the binding energy between these implants and a vacancy and the mutual binding energy are lower than for Ag. The first will hamper the impurity transport, the second will lead to a lower clustered fraction for similar mobilities as for Ag.

Although thermal activation was needed in this study to obtain clustering, we believe, that the findings in this study strongly support the model that radiation enhanced diffusion and radiation induced segregation for oversized solutes takes place through a bound vacancy-solute complex.

This work was partly financed by the Stichting voor Fundamenteel Onderzoek der Materie (Foundation for Fundamental Research on Matter) subsidized through the Nederlandse Organisatie voor Zuiver Wetenschappelijk Onderzoek (Netherlands Organization for the Advancement of Pure Research).

## REFERENCES

- [1] A.D. Marwick, Nucl. Instr. and Meth. 182/183,827(1981).

- [ 2 ] A.D. Marwick, R.C. Piller, Nucl. Instr. and Meth. 182/183,121(1981).
- [ 3 ] G. Martin, R. Cauvin, J.-L. Bocquet and A. Barbu in: Point Defects and Defect Interactions in Metals, eds. J. Takamura, M. Doyama and M. Kiritani, North Holland 1982, pp.923-930.
- [ 4 ] L.E. Rehn in: Metastable Materials Formation by Ion Implantation, eds. S.T. Picreux and W.J. Choyke, North Holland 1982, pp. 17-34.
- [ 5 ] A. van Veen, A. Warnaar and L.M. Caspers, Vacuum 30,109(1980).
- [ 6 ] E.V. Kornelsen, Rad. Eff.13,227(1972).
- [ 7 ] L.M. Caspers, A. van Veen, Phys. Stat. Sol. (a) 68,339(1981).
- [ 8 ] E.V. Kornelsen and A.A. van Gorkum, Vacuum 31,99(1981).
- [ 9 ] G.J. van der Kolk, A.S. Hydra, A. van Veen and L.M. Caspers, Nucl. Instr. and Meth. 209/210,1047(1983).
- [ 10 ] G.J. van der Kolk, A. van Veen, L.M. Caspers and J.Th.M. de Hosson, Rad. Eff. 71,109(1983).
- [ 11 ] G.J. van der Kolk, A. van Veen, L.M. Caspers and J.Th.M. de Hosson, to be published in J. of Nucl. Mat, chapter 4.1.
- [ 12 ] M. Paunov and E. Michailov, Surf. Sc. 81,479(1979).
- [ 13 ] R.A. Johnson and W.D. Wilson in Interatomic Potentials and Simulation of Lattice Defects, eds. P.C. Gehlen, J.R. Beeler Jr. and R.I. Jaffee (Plenum Press, New York 1972) p. 301.
- [ 14 ] P.T. Wedepohl, Proc. Phys. Soc. 92,79(1967).
- [ 15 ] W.D. Wilson and C.L. Bisson, Phys. Rev. B 3,3984(1971).
- [ 16 ] G.J. van der Kolk, K. Post, A. van Veen, F. Pleiter and J.Th.M. de Hosson, to be published in Rad. Eff, chapter 3.3.
- [ 17 ] A.R. Miedema, F.R. de Boer and R. Boom, Calphad 1,341(1977).
- [ 18 ] G.J. van der Kolk, A. van Veen, L.M. Caspers and J.Th.M. de Hosson, to be published in Rad. Eff. Lett, chapter 4.2.
- [ 19 ] A.R. Miedema, Z. Metallkunde 70,345(1979).
- [ 20 ] A.A. van Gorkum, E.V. Kornelsen, Rad. Eff. 42,93(1979).
- [ 21 ] E.V. Kornelsen, M.K. Sinha, J. of Appl. Phys. 39,4546(1968).



## SUMMARY

Thermal Helium Desorption Spectrometry (THDS) has been applied to study the interaction of various defects with metallic impurities in tungsten. The metallic impurities were brought into a W(100) single-crystal by implantation with energies between 5 and 25 keV.

In chapter 2 the ion implantation and He desorption equipment is described.

In chapter 3 the interaction is described of implanted impurities with vacancies, formed during the implantation. The first two sections are devoted to computer simulations, on the one hand it appears that after implantation usually one or more vacancies are located within a distance of four lattice units of the implanted atom, on the other hand it appears that these nearby vacancies prevent detection of the implanted atom with THDS. The third section deals with THDS and Perturbed Angular Correlation (PAC) experiments of Ag or In implanted W-samples. The results confirm the image that near-vacancies hinder detection of the implanted atoms with THDS. The binding energy of an extra vacancy to substitutional Ag respectively In is 0.5 and 1.0 eV.

In chapter 4 the interaction of interstitials with substitutional metallic impurities is described. He-interstitials bind to substitutional Ag, Al, Cr, Cu and Mn with energies above 0.7 eV. A pair-potential model reproduces the experimental values of the binding energy fairly well. Self-interstitial atoms react with the impurities in such a way, that He binding at room temperature is not observed for the then formed defect-complex. One may suppose that the impurities become mobile, either thermally activated or not, and migrate to the surface.

In chapter 5 the interaction between the impurities is studied. In the case of Ag, and to a lesser extent Cu, clustering of the Ag atoms respectively Cu atoms was observed. Transport of the Ag atoms respectively Cu atoms has probably taken place during annealing at 800 to 1000 K through the implantation produced vacancies.

## SAMENVATTING

Thermische Helium Desorptie Spectrometrie (THDS) is toegepast om de interacties van diverse defecten met metallische onzuiverheden in wolfraam waar te nemen. Hiertoe werd allereerst de metallische onzuiverheid geschoten met energieën tussen 5 en 25 keV in een wolfraam één-kristal.

In hoofdstuk 2 worden de hiervoor gebruikte ionenbeschietings- en He-desorptie-apparatuur beschreven.

In hoofdstuk 3 wordt de interactie beschreven van ingeschoten onzuiverheden met vakatures, gevormd tijdens de beschieting. De eerste twee secties zijn gewijd aan computersimulaties, enerzijds blijkt hieruit dat er na beschieting gewoonlijk één of meer vakatures zich binnen een afstand van vier roostereenheden van het ingeschoten atoom bevinden, anderzijds blijkt hieruit dat deze nabije vakatures detectie van het ingeschoten atoom met THDS verhinderen. De derde sectie beschrijft experimenten verricht met THDS en met verstoorde hoek correlatie metingen aan wolfraam beschoten met Ag en In. De resultaten bevestigen het beeld dat nabije vakatures detectie van het ingeschoten atoom met THDS onmogelijk maken. De bindingsenergie van een extra vakature aan een substitutioneel Ag respectievelijk In atoom is 0,5 eV en 1,0 eV.

In hoofdstuk 4 wordt de interactie van interstitiële met substitutionele metallische onzuiverheden beschreven. Interstitiële He atomen binden aan de onzuiverheden Ag, Al, Cr, Cu en Mn met energieën groter dan 0,7 eV. Een paar-potentiaal model blijkt de gevonden bindingsenergieën redelijk te kunnen reproduceren. Zelf-interstitiële reageren met de metallische onzuiverheden op dusdanige wijze dat He binding aan de gevormde defect-complexen niet meer optreedt bij kamertemperatuur. Men mag veronderstellen dat de onzuiverheden, al dan niet thermisch geactiveerd, mobiel worden, en bij het oppervlak terecht komen.

In hoofdstuk 5 tenslotte wordt de interactie tussen de onzuiverheden onderling beschouwd. In het geval van Ag en in veel mindere mate Cu in W werd "clustering" van de Ag respectievelijk Cu atomen waargenomen. Transport van de Ag respectievelijk Cu atomen heeft waarschijnlijk plaatsgevonden tijdens verhitting tot 800 à 1000 K middels de in ruime mate aanwezige vakatures.



Stellingen behorende bij het proefschrift: Thermal Helium Desorption Spectrometry applied to Metallic Implants in Tungsten.

## 1

De resultaten van berekeningen verricht door Baskes en Melius [1], waarbij de bindingsenergie van He aan een vakature in een aantal k.v.g. metalen groter is dan de interstitiële formatieenergie, zijn fysisch uiterst onwaarschijnlijk.

[1] M. Baskes, C.F. Melius, Phys. Rev. B. 20,3197(1979).

## 2

De desorptie van He uit nikkel, na implantatie met 700 eV, zoals gerapporteerd door Philipps en Sonnenberg [1], is niet korrekt weergegeven.

[1] V. Philipps, K. Sonnenberg, J. of Nucl. Mat. 114,95(1983).

## 3

Maeda, Vitek en Sutton [1] stellen dat er voor de juiste opsplitsing van de energie van een metaalrooster in een paar-potentiaal term en een dichtheidsafhankelijke term geen aanwijzingen beschikbaar zijn. Hiermee gaan zij ten onrechte voorbij aan de vakatureformatie energie.

[1] K. Maeda, V. Vitek and A.P. Sutton, Acta Metall. 30,2001(1982).

## 4

Deicher, Grübel en Wichert [1] hebben binding van He aan In in roestvrij staal waargenomen. Gezien de waargenomen stabiliteit van de He-In complexen en de resultaten gepresenteerd in [2] moeten wij aannemen dat het hier He-In-vakature complexen betreft.

[1] M. Deicher, G. Grübel and Th. Wichert, Nucl. Instr. and Meth. 209/210,817(1983).

[2] Dit proefschrift, hoofdstuk 4.1.

## 5

De industriële toepassing van ionenimplantatie, met als oogmerk de verbetering van de corrosiebestendigheid van metaaloppervlakken, zal, in tegenspraak met de positieve berichtgeving van sommige onderzoeksgroepen, nog lang op zich laten wachten.

## 6

De behandeling van ernstig lichamelijk gehandicapten, door een horizontaal georganiseerd multidisciplinair behandelteam leidt in vele gevallen tot een betere behandeling in vergelijking met de behandeling door een hiërarchisch georganiseerd behandelteam.

## 7

In een tijd, dat de personeelsformatie aan de wetenschappelijke instellingen dusdanig van opbouw is, dat op bepaalde werkzaamheden onevenredig lang gewacht moet worden, mag men het argument, dat men een te duur betaalde kracht is om die werkzaamheden zelf uit te voeren, niet meer hanteren.

## 8

Afslanking van instellingen door het zogenaamde natuurlijk verloop leidt, zonder gepaste tegenmaatregelen, tot een volslagen willekeur wat betreft de keuze van af te slanken afdelingen, secties of groepen binnen die instellingen.

## 9

Het risico op overlijden dat een amateur vechter loopt tengevolge van deelname aan wedstrijden wordt grotendeels bepaald door de aanwezigheid van rokers in de wedstrijdruimte.

Zie o.a. Stralingsbescherming, dr. J. Weber en dr. C.E. Rasmussen, Delft 1974.

## 10

Indien de zure regen, en de daardoor veroorzaakte bossterfte, het gevolg zou zijn van het bedrijven van kerncentrales, dan zou een groot deel van de bevolking zich uitspreken voor onmiddellijke stopzetting van die centrales.



## CURRICULUM VITAE

Op 4 juni 1955 werd de schrijver van dit proefschrift geboren te Ede. Na enige omzwervingen in den lande verliet hij in 1972 de HBS te Heemstede, en werd de studie aan de afdeling Technische Natuurkunde der Technische Hogeschool te Delft aangevangen. Het afstudeerwerk werd verricht bij de vakgroep Reactorfysica o.l.v. prof. dr. ir. H. van Dam in de subgroep stralingsschade van dr. ir. L.M. Caspers en dr. A. van Veen. Tijdens de afstudeerperiode werkte hij als student-assistent bij de stralingsbeschermingsdienst van het Interuniversitair Reactor Instituut te Delft. In augustus 1978 werd de studie afgesloten. Vervolgens ving hij aan, als erkend gewetensbezwaarde ter vervanging van de militaire dienst, met werkzaamheden bij de vakgroep Meet- en Regeltechniek en Cybernetische Ergonomie o.l.v. prof. dr. ir. H.G. Stassen aan de afdeling Werktuigbouwkunde aan de Technische Hogeschool Delft. De werkzaamheden hadden betrekking op de informatieverwerking in de gezondheidszorg. In december 1979 trad hij in dienst van de Stichting voor Fundamenteel Onderzoek der Materie (FOM). Vanaf die tijd verrichtte hij het in dit proefschrift beschreven onderzoek bij de bovengenoemde vakgroep Reactorfysica.





